

國立交通大學  
材料科學與工程學系  
博士論文

超低介電孔洞材料 MSQ 薄膜中起孔洞劑  
聚集行為及孔洞形貌控制之研究

The porogen aggregation behavior, pore size,  
and size control of ultra-low- $k$  porous  
organosilicate films based on MSQ/porogen  
hybrid system

研 究 生：譚昱涵

指導教授：呂志鵬 博 士

中 華 民 國 一 百 零 一 年 六 月

超低介電孔洞材料 MSQ 薄膜中起孔洞劑聚集行為

及孔洞形貌控制之研究

**The porogen aggregation behavior, pore size, and size control of  
ultra-low- $k$  porous organosilicate films based on MSQ/porogen hybrid  
system**

研 究 生： 譚昱涵

Student： Yu-Han Chen

指導教授： 呂志鵬 教授

Advisor： Dr. Jihperng Leu



June 2012

Hsinchu, Taiwan, Republic of China

中 華 民 國 一 百 零 一 年 六 月

# 超低介電孔洞材料 MSQ 薄膜中起孔洞劑聚集行為 及孔洞形貌控制之研究

研究生：譚昱涵

指導教授：呂志鵬 博士

國立交通大學

材料科學與工程學系

摘要

本研究使用延後移除高溫起孔洞劑製程 (post-integration porogen removal scheme) 的混合型低介電材料，主要分為三個部份：(1) 探討起孔洞劑 (porogen) 於低介電母材中團聚的行為；(2) 分散 porogen 於低介電母材中，並有效控制 porogen 以及最後孔洞的尺寸；(3) 提高母材中 porogen 的含量，致使更有效降低介電常數維持更小孔洞，並探討其結構與性質間之關係。首先，選用 methylsilsesquioxane (MSQ) 為母材，polystyrene-b-polybutadiene-b-polystyrene (SBS) 作為高溫起孔洞劑，使之形成混合型低介電材料薄膜。在不同升溫速率條件下利用即時動態的 grazing incidence small angle X-ray scattering (GISAXS) 量測 porogen 尺寸變化；並以黏度變化和紅外線光譜儀 (FT-IR) 分析母材結構對 porogen 尺寸的影響。藉由其交互行為可

得知 SBS 的團聚主要受三個關鍵的溫度影響; (1)母材的玻璃轉換溫度，此時開始有團聚現象，(2)母材開始大量產生交鏈的溫度(或結構由 cage 轉換成 network 時)，此時團聚現象更甚，(3) 母材完成交鏈的溫度，此時結構固化，團聚不易產生。確定團聚機制後，第二部分使用 polystyrene(PS)作為 porogen，並使用陰離子型的 dodecylbenzenesulfonate (NaDBS)以及陽離子型的 domiphen bromide (DB)界面活性劑將 porogen 進行表面改質，然後檢測慢速升溫(2°C/min)過程中的 porogen 尺寸及黏度的變化。研究結果指出，改質過的 porogen 表面帶有電荷，並存在庫倫力將其排斥並穩定分散於母材中，而且在改質過後的 porogen 造成的電滯效應使母材整體黏度上昇，使之更不容易擴散或聚集於母材內。另一方面帶有正電的 PS 會與 MSQ 母材中的 Si-OH 有吸引作用，位置會被母材固定住致使更不易團聚，故可達到更佳控制孔洞大小的效果。最後研究將 DB 改質的 PS 增量於低介電母材中，用以增加孔隙率並降低介電常數，結果指出孔隙率達到 45vol.%以上，介電常數可有效降低，且孔洞呈現獨立圓形，其機械性質因無內連結大型孔洞可維持強度。以往文獻指出 porogen 的含量大於 25wt%或孔隙率達到 30vol.%以上時，因為 porogen 大量聚集而造成熱移除後的大型孔洞，本研究發展一個表面改質方法使 porogen 可以有效分散 porogen 於母材中並能提高最後之孔隙率。

# **The porogen aggregation behavior, pore size, and size control of ultra-low- $k$ porous organosilicate films based on MSQ/porogen hybrid system**

Student: Yu-Han (Hans) Chen

Advisor: Dr. Jihperng (Jim) Leu



This work focuses on the hybrid low- $k$  film in a late-porogen removal scheme. There are three parts are discussed including: (1) the aggregation behavior of porogen in the hybrid film; (2) disperses the porogen in the low- $k$  precursor and control the porogene size (later pore size); (3) increases the loading of porogen in the low- $k$  materials to reduce  $k$  value and try to remain the small pore size. Firstly, the interaction between polystyrene-*b*-polybutadiene-*b*-polystyrene (SBS) porogen and low- $k$  methylsilsesquioxane (MSQ) matrix under different curing profiles and their impact on porogen size were studied by grazing incidence small angle X-ray scattering (GISAXS), viscosity measurement, and Fourier transform infrared analysis. The aggregation of SBS

porogen was greatly influenced by the microstructure of MSQ matrix at three controlling temperatures; namely (1) glass transition temperature,  $T_g$  ( $\sim 100^\circ\text{C}$ ), (2) onset temperature ( $160^\circ\text{C}$ ) for transforming cage to network structure, and (3) immobilization temperature ( $170^\circ\text{C}$ ). Secondly, an anionic surfactant, sodium dodecylbenzenesulfonate (NaDBS) and a cationic surfactant, domiphen bromide (DB) were used to modify the surface potential of PS porogen in the low- $k$  film. The NaDBS- and DB-modified porogens with higher surface potential impede their aggregation within the cross-linking MSQ matrix, resulting in a smaller porogen size, by electrostatic repulsion and increased viscosity due to the electroviscous effect. In addition, the columbic attraction between Si-OH groups of MSQ matrix and the positively charged, DB-modified PS, restrains the PS porogen, thus reduces its aggregation during the curing step, leading to small porogen size and tight distribution at  $200^\circ\text{C}$  and later a similar pore size after removal of porogen at  $400^\circ\text{C}$ . Finally, the different loading of polystyrene (PS) porogen with/without cationic surfactant, domiphen bromide (DB) modification in MSQ appeared for porous low- $k$  films. The pore size, morphology, mechanical strength and  $k$  of porous low- $k$  films with different porosity were investigated. The porosity could be increased above 45 vol.% by porogen surface modification, and reduced  $k$  from 2.6 to 1.9. The porous film appear the no interconnect pore and maintain the sphere shape. The past paper indicates that porogen occur obvious aggregation at porogen loading  $>25$  wt% (or porosity  $>30$  vol.%). In this work, we develop a method of porogen surface-modification to disperse the porogen in the low- $k$  materials and increase the porogen loading (porosity) effectively.

# Acknowledgements

如果能夠重來一次，我不知道會不會再選擇攻讀博士學位。人生最可惜的地方就是沒有如果，這是一趟單程的旅行，誰都沒有重頭啟程的機會跟權利，但是換句話說，這也是生命最可貴的地方，沿路美麗的風景只有一次，旅途上的過客或朋友甚至是敵人，都是無可替代的，所以才更應該珍惜與感激。

首先感謝我的指導教授呂志鵬老師，感謝老師這些年來在課業上的教導及協助，除了訓練學生邏輯以及專業之外，老師也提供了很多待人處事的道理及應對的方法，我覺得我不是一個好的學生，但老師非常的有耐心，雖然我跟老師的互動相對而言比較少，但是我心裡是很敬重老師的。然後感謝協助完成論文的同步輻射中心的 23A 光束線成員，包括鄭有舜、蘇秋琿、蘇群仁、廖桂芬等，這些年來在實驗數據上的解析及幫助。還有工研院化材所楊偉達、謝青城在流變黏度儀上的協助。

接著謝謝實驗室的博士班成員。感謝同梯的好友徐國原在實驗及人生上的提點，就像燈塔一樣指引了方向，也在我很低落的時候，告訴我建立價值跟重拾熱情。謝謝車牧龍，感謝總會在我犯了過錯的時候提醒我，是我無話不談的好朋友，也是實驗及生活上幫助我最多的人。謝謝徐幸鈴，在基礎理論上的教學及討論，常常有聽君一席話，勝讀十年書那種茅塞頓開的體會。謝謝王智這個好兄弟一起度過很多大風大雨的日子，常常在籃球以及課外活動上提攜我，是我最喜歡的一

個有情有義的好朋友。謝謝徐明義好鄰居，我們一起坐的位子不知道幾年了，感謝總是不厭其煩地幫我解決一些雞毛蒜皮的小問題，例如修電腦。感謝涂弘恩帥哥，雖然沉默寡言存在感很低，但是有需要他的時候，他就會拿掉石頭帽子站在第一線。另外感謝劉柏村，帶給我們實驗室不同領域的課外活動與無數的歡樂。特別感謝姚奕全在最後口試以及論文上的協助以及幫忙。也感謝我多年來的好友董憲澤，在學業及生活上的協助，以及提供很多冷笑話。

接著謝謝碩士班以及專題生成員。感謝鄧鈞元、陳冠宇、湯季高一起經歷半夜睡實驗室的日子。感謝專題生楊麒瀚、姜翔耀、陳思漢在實驗上的協助。感謝何瑜修在運動健身上的陪伴。另外感謝有邱詩雅、黃少農、莊如瑛、陳欣源、徐婉婷、許書豪、陳奎岳、胡勝翔、蔡沁穎、邱維剛、田丞芳、黨希昀、廖麒雅、黃耀輝、周宏宇、蔡豐仰、梁宗琦、洪唯齡等在生活上的互相照應及幫助。

感謝我的女友孫珮容，在學業最後很難熬的這半年，每一天最快樂的時候，就是能夠在電話裡說話的時候，雖然相隔兩地，但滿滿的鼓勵及甜甜的思念，總是可以圍繞在我的身邊。最後感謝我的父親譚茂崧先生以及母親陳素蘭女士，在經濟上的無條件支持，讓我可以沒有後顧之憂的完成學業。金錢是可以量化，計算以及償還的，但是您們的愛是我花一輩子都無法還清的。所有的榮耀獻給我的家人。

人生不能重頭開始，但是沒關係，心境可以從零開始，這樣的每一天，都會是新的旅程。



# Contents

	Page
摘 要.....	i
ABSTRACT.....	iii
Acknowledgements.....	v
Contents.....	vii
Table Captions .....	x
Figure Captions.....	xi
Chapter 1 Introduction.....	1
1.1 Background.....	1
1.2 Overview.....	5
Chapter 2 Literature Review.....	8
2.1 Backend interconnect challenges.....	9
2.2 Classification of dense low- $k$ materials.....	12
2.2.1 Fluorinated Silicate Glass.....	13
2.2.2 Carbon-doped Oxide (CDO).....	13
2.2.3 SiLK <sup>TM</sup> .....	14
2.2.4 Silsesquioxane based materials.....	15
2.3 Porous low- $k$ materials.....	16
2.3.1 Silica aerogel and xerogel low- $k$ dielectrics .....	17
2.3.2 Pure Silica-Zeolite low- $k$ film.....	18
2.3.3 Nano-Clustering Silica (NCS) .....	19
2.3.4 Templated-type (porogen) low- $k$ dielectrics .....	19
2.4 Selection of porogens.....	20
2.4.1 Linear amphibic block polymer.....	20
2.4.2 Dendrimers polymer .....	21
2.4.3 Star-shape polymers.....	22
2.4.4 Cage supramolecules .....	23
2.4.5 Well-dispersion porogen .....	24
2.4.6 Reactive polymers.....	24

2.5 Challenges in porous low- $k$ .....	26
2.5.1 Pore size.....	27
2.5.2 Porogen dispersion.....	28
2.5.3 Porogen loading and high porosity .....	29
2.6 Post-integration porogen removal scheme.....	31
Chapter 3 Experimental .....	60
3.1 Materials candidates .....	60
3.1.1 MSQ/porogen hybrid materials .....	60
3.1.2 Porogen surface modification .....	61
3.2 Sample preparation .....	61
3.2.1 The <i>in-situ</i> porogen activity test .....	61
3.2.2 Porogen modification.....	63
3.2.3 Different porosity low- $k$ film with and without modification .....	65
3.2.3.1 Porosity .....	66
3.2.3.2 Pore size and porogen size.....	66
3.2.3.3 Electrical characteristics .....	67
3.2.3.4 Chemical characteristics .....	68
3.2.3.5 Mechanical strength.....	68
Chapter 4 Effect of Curing on the Porogen Size in the Low- $k$ MSQ/SBS Hybrid Films .....	73
4.1 <i>In-situ</i> porogen size test.....	73
4.2 <i>In-situ</i> viscosity test.....	76
4.3 Structure variation and porogen aggregation.....	78
4.4 Mechanical strength.....	83
4.5 Summary .....	84
Chapter 5 Effect of Surfactants on the Porogen Size in the Low- $k$ Methylsilsesquioxane/Polystyrene Hybrid Films .....	92
5.1 Porogen size in the precursor.....	93
5.2 <i>In-situ</i> porogen size test .....	94
5.3 Pore size, distribution and porosity.....	96
5.4 Structure variation vs. porogen behavior .....	96
5.5 Matrix structure variation with charged porogen.....	101

5.6 Dispersion mechanism.....	103
5.7 Summary.....	107
Chapter 6 Well-dispersed Ultra-Low- <i>k</i> Porous Methylsilsesquioxane using a Cationic Surfactant-modified Polystyrene Porogen .....	117
6.1 Porogen size in the precursor.....	118
6.2 Porosity and pore size, shape.....	119
6.3 Dielectric constant and mechanical properties .....	124
6.4 Summary.....	127
Chapter 7 Concusions.....	136
References.....	139
Vita.....	153



## Table Captions

Table 2.1 Type of ILD materials .....	33
Table 2.2 Principle properties of SSQ based dielectric materials.....	34
Table 2.3 Commercially available SSQ-based low- $k$ materials.....	35
Table 2.4 The pore size (nm) from PCL porogen under different low- $k$ process .....	36
Table 2.5 The property of reactive-porogen on SSQ-based low- $k$ materials .....	37
Table 2.6 The impact of porosity change on SSQ-based low- $k$ materials. ....	38
Table 5.1 The zeta potential and the corresponding particle size of PS porogen in the solution as a function of surface modification.....	109
Table 6.1 Density and porosity of low- $k$ films by using XRR.....	129

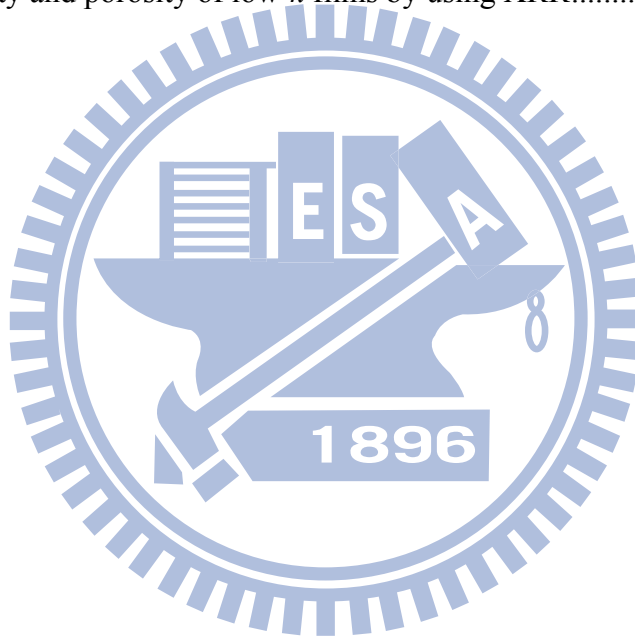
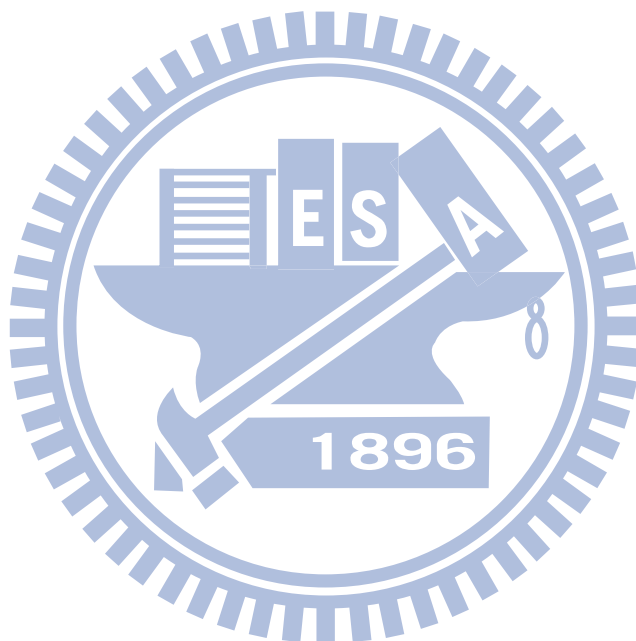


# Figure Captions

Figure 1.1 Formation schemes of porous low- $k$ dielectrics in copper/low- $k$ interconnects: (a) immediately after ILD deposition and (b) post-integration porogen removal scheme after Cu CMP step forming a copper/low- $k$ layer. ....	7
Figure 2.1 Industry average “Moore’s law” and chip size trends. ....	39
Figure 2.2 Device scaling projection trend shown in terms of gate length (half pitch) for Flash, DRAM, and MPU/ ASIC microelectronics products. ....	40
Figure 2.4 Decrease in interconnect delay and improved performance are achieved by using Cu and low- $k$ dielectric. ....	42
Figure 2.5 Historical transition of ITRS low- $k$ roadmap .....	43
Figure 2.6 Basic structure of FSG matrix. ....	44
Figure 2.7 Depiction of possible bond rearrangements upon SiOF film hydration to produce Si–OH bonding and the release of HF from the film. ....	45
Figure 2.8 Carbon-doped silica glass and schematic bonding structure. ....	46
Figure 2.9 The typical precursors of CDO materials. ....	47
Figure 2.10 Organic SiLK™ chemical structure units. ....	48
Figure 2.11 Basic structure units of SSQ dielectric materials consist of random, ladder and cage structures. R= H, CH <sub>3</sub> for HSQ and MSQ respectively. ....	49
Figure 2.13 Schematics of the nano clustering silica (NSC) formulation and its film deposition and curing processes. ....	51
Figure 2.14 The conventional formation of porous low- $k$ by using template-type porogen method. ....	52
Figure 2.15 Schematic structures of phase behaviors of PEO-b-PPO-b-PEO triblock ..	53
Fig. 2.17 Star-shape polymer porogens: PCL4, four-armed poly(ecaprolactone) and PCL6, six-armed poly(e-caprolactone). ....	55
Figure 2.18 $\beta$ -Cyclodextrin ( $\beta$ -CD), a cage supramolecular porogen .....	56
Figure 2.19 The synthetic scheme: (a) sol-gel reaction and (b) ATRP method to prepare hybrid block copolymers based on MSQ. ....	57
Figure 2.20 The energy and the distance of relationship for two particles. ....	58
Figure 2.21 The integration scheme of the post-integration porogen removal scheme. ..	59
Figure 3.1 The molecular structure of (a) MSQ as the low- $k$ matrix; (b) PS-b-PB-b-PS and (c) PS as the high-temperature porogens. ....	70
Figure 3.2 The molecular structure of surfactant: (a) NaDBs, and (b) DB. ....	71
Figure 3.3 Typical geometry of GISAXS measurement. ....	72
Figure 4.1 2-D GISAXS scattering patterns of the hybrid low- $k$ films as a function of	

cure temperature under (a) slow curing and (b) rapid curing condition. ....	86
Figure 4.2 $\ln(I)-q^2$ plots along $q_{xy}$ from 2D GISAXS scattering patterns of the hybrid low- $k$ films cured at various temperatures under (a) slow and (b) rapid curing conditions.....	87
Figure 4.3 Porogen sizes in the hybrid low- $k$ films as a function of cure temperature under (a) slow and (b) rapid curing conditions.....	88
Figure 4.4 Viscosity of the hybrid low- $k$ films as a function of cure temperature under (a) slow curing profile at 2°C/min to 250°C (b) isothermal at 200°C. ....	89
Figure 4.5 (a) Infrared spectra of MSQ/SBS hybrid films cured up to various temperatures: 25, 100, 150 and 200°C. (b) The ratio of network/cage structure in the MSQ/SBS hybrid films as a function of cure temperature between 30 and 200°C at an interval of 10°C. ....	90
Figure 4.6 The viscosity, porogen size, and network/cage structure ratio of the MSQ/SBS hybrid films as a function of temperature during slow curing....	91
Figure 5.1 2-D GISAXS scattering patterns of the low- $k$ MSQ/PS hybrid films as a function of cure temperature: (a) PS without modification, (b) NaDBS-modified PS, and (c) DB-modified PS. ....	110
Figure 5.2 Porogen sizes and distribution in the low- $k$ MSQ/PS hybrid films as a function of cure temperature: (a) PS without modification, (b) NaDBS-modified PS, and (c) DB-modified PS. ....	112
Figure 5.3 2-D GISAXS scattering patterns of the low- $k$ porous MSQ films after removal of PS porogens at 400°C: (a) PS without modification, (b) NaDBS-modified PS, and (c) DB-modified PS. ....	113
Figure 5.4 (a) The viscosity, (b) porogen size, and (c) the ratio of network-/cage- Si-O in the low- $k$ MSQ/PS hybrid films as a function of cure temperature for NaDBS-modified PS (●), DB-modified PS (■), and PS without modification (▲). ....	114
Figure 5.5 FTIR spectra (880 to 1170 $\text{cm}^{-1}$ ) of low- $k$ MSQ/PS hybrid films at 25°C for PS without modification, NaDBS-modified, and DB-modified PS.....	115
Figure 5.6 (a) Peak position and (b) peak intensity of Si-OH infrared absorption band as a function of cure temperature for NaDBS-modified PS (●), DB-modified PS (■), and PS without modification (▲).....	116
Figure 6.1 The size and surface potential of PS porogen under different pH value and surface modification by DB. ....	130
Figure 6.2 Morphology of the low- $k$ porous films with different porosity as a function of: (a) no modification, (b) modification by DB. ....	131
Figure 6.3 2-D GISAXS scattering patterns of the low- $k$ porous films with the different porosity under porogen as a function of : (a) no modification, (b)	

modification by DB. ....	132
Figure 6.4 Pore size and distribution in the low- $k$ porous films with different porosity as a function of: (a) no modification, (b) modification by DB. ....	133
Figure 6.5 The (a) dielectric constant, (b) ratio of network/cage and (c) mechanical strength of porous low- $k$ film with and without modification under different porosity.....	134
Figure 6.6 2-D GISAXS scattering patterns of the low- $k$ porous films under modification with the different porogen loading. ....	135



# Chapter 1

## Introduction

This work discusses the primary issues around pore size control of porous low- $k$  materials manufactured by using “low- $k$  matrix/pore generator (porogen)” hybrid material in a novel post-integration porogen removal scheme. Chapter 1 introduces the background, motivation and organization of this dissertation.

### 1.1 Background

The improvement in device density and performance has significantly impacted the feature size of the wiring structure for interconnects. As the feature size in integrated circuit is scaled down, the increase in propagation, Resistance-Capacitance (RC) delay, crosstalk noise and power dissipation of the backend interconnect becomes a limiting factor [1]. The impact can be examined by evaluating the RC delay of the multilevel interconnects [2]. To minimize the increase of RC delay, the industry first introduced copper metallization ( $1.9 \mu\Omega\text{-cm}$ ) to reduce the resistance (vs.  $\text{Al} \sim 3.3 \mu\Omega\text{-cm}$ ) as well as improve the electromigration performance of wiring [3]. As the minimum device dimensions reduce beyond 250 nm,  $\text{SiO}_2$  insulator is no longer suitable. In order to continually reduce the RC delay of interconnects, low dielectric constant (low- $k$ )



materials have been introduced primarily to replace the interlayer dielectric (ILD), SiO<sub>2</sub> ( $k \sim 4.2$ ). Therefore, the need of lowering the  $k$ -value of bulk SiO<sub>2</sub> can be attained by lowering the density of matrix and/or addition of lower polarizability atoms or bonds such as fluorosilicate glass (FSG,  $k = 3.7$ ) [4]. Organic SiLK<sup>TM</sup> ( $k = 2.65$ ) was first introduced by IBM at 0.13  $\mu\text{m}$  technology node [5]. However, inorganic dielectric such as carbon-doped oxide (CDO) was adopted by the majority of semiconductor companies mainly in 90 nm and beyond. Major commercially available CDOs are Aurora<sup>TM</sup> ( $k = 2.9$ , ASM), Coral<sup>TM</sup> ( $k = 2.85$ , Novellus), and Black Diamond<sup>TM</sup> ( $k = 2.65$ -3.0, Applied Materials) [6,7].

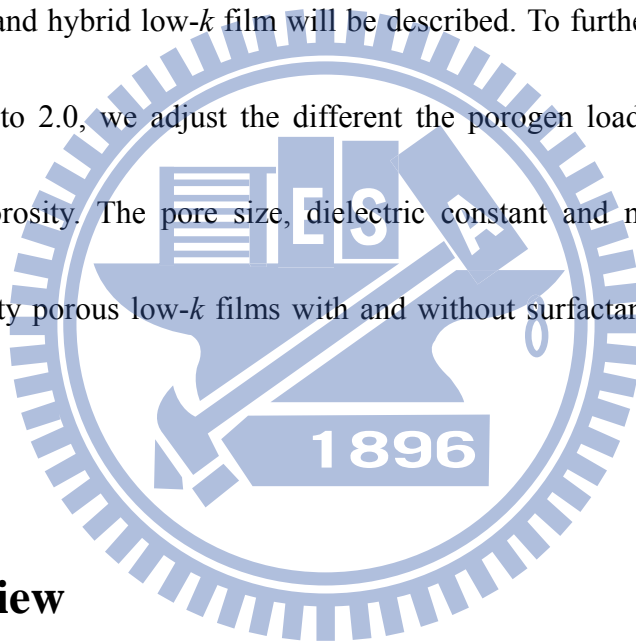
Moving further toward 45 nm node, the incorporation of porosity, in which air has  $k_{\text{air}} = 1$ , the lowest attainable value, becomes essential for producing viable low- $k$  materials with  $k < 2.5$  [8]. And next 22 nm technology node and beyond, it is well recognized that the incorporation of porosity is critical to the search for viable low- $k$  dielectrics ultra low- $k$  materials with  $k$  value  $< 2.3$  [9]. Conventionally, porous low- $k$  dielectric films are generally formed following the deposition of a low- $k$  matrix with a thermally labile templating agent or pore generator (porogen) [10], which are burned out by thermal treatment at low temperatures (typically  $\leq 200^\circ\text{C}$ ) immediately following the deposition of the film as illustrated in Figure 1.1(a). However, such porous films might encounter reliability issues, such as high leakage and low dielectric breakdown strength

at the barrier/low- $k$  interface, because of the insufficient coverage for large pores induced by plasma damage during the etching process [11,12,13]. To circumvent such reliability issues, a novel post-integration porogen removal method is proposed, which uses a high decomposition temperature ( $T_d > 350^\circ\text{C}$ ) porogen in the material design and an integration scheme [14,15,14,15]. It uses a high temperature porogen, such as poly(styrene-*b*-butadiene-*b*-styrene), and poly(styrene-*b*-4-vinylpyridine) [16] to defer the formation of a porous low- $k$  dielectric, until the completion of the copper chemical mechanical polishing (CMP) step, and then thermally removes the sacrificial porogen from the hybrid dielectric film, as illustrated in Figure 1.1(b). In the post-integration porogen removal scheme, the porogen in hybrid low- $k$  matrix/porogen films must survive at the highest possible processing temperature (preferably  $300\text{-}350^\circ\text{C}$ ) cycling of back-end-of-line (BEOL) processing steps. For such hybrid films to survive the backend processing such as CMP in the post-integration porogen removal scheme, the hybrid low- $k$  material should possess the sufficiently strong mechanical strength. Moreover, the mechanical properties such as Young's modulus of the hybrid films depend on the porogen morphology, size, and size distribution. Yet, the interaction between porogen and low- $k$  matrix during curing and their impact on the porogen size of low- $k$ /porogen hybrid films are not fully understood. Thus, it is of critical interest to understand the porogen behavior and how to control its size in the low- $k$  matrix/porogen

hybrid films before burning out porogen to form a porous low- $k$  film. In this study, porogen aggregation behavior was elucidated by *in situ* grazing incidence small-angle X-ray scattering (GISAXS) and viscosity test. In general, 2D GISAXS is a powerful instrument to measure the characteristics of pore in the porous materials. That can measure pore size in the interlayer of porous film and do not cause any damage of sample. The principle is that detect the scattering signal from the second phase such as pore in the sample. In this study, we also choose GISAXS to analysis the pore size and distribution of porous low- $k$  film. Specifically, we use 2D GISAXS to analysis the porogen size variation in the hybrid low- $k$  film by *in-situ* test. On the other hand, we use *in-situ* viscosity test and Fourier transform infrared analysis (FT-IR) to define the relationship between of matrix structure variation and porogen aggregation.

Therefore, in this study, methylsilsesquioxane (MSQ) and high  $T_d$  polymers, poly(styrene-block-butadiene-block-styrene) (PS-*b*-PB-*b*-PS, SBS) and were used as low- $k$  material matrix and high temperature porogens. In order to define the aggregation and diffusion of porogen before burning out, the thesis prior to focus on the porogen activity in the hybrid film during thermal profile. The effects of curing rate (slow: 2°C/min vs. rapid: 200°C/min) and cure temperature on the SBS porogen size in the hybrid low- $k$  films cured up to 200°C were studied by *in-situ* GISAXS, viscosity measurement, and FT-IR analysis. The next task is to disperse/control porogen in the

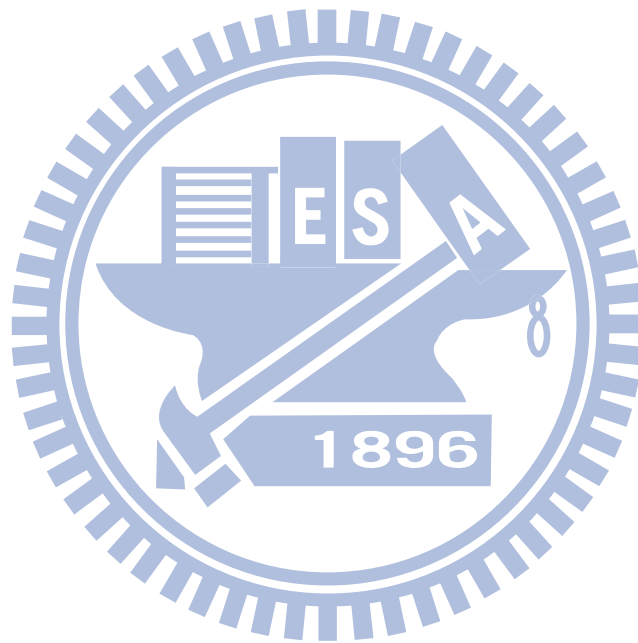
hybrid low- $k$  film. We replace the lower molecular weight polymer polystyrene (PS) as high temperature porogen. An anionic surfactant, sodium dodecylbenzenesulfonate (NaDBS) and a cationic surfactant, domiphen bromide (DB), were used to modify the PS porogen surface in the solution and the low- $k$  hybrid films. The effect of surface modification on the porogen and pore size in the low- $k$  MSQ/PS hybrid films at 10wt% PS loading under a slow curing rate will be studied. And the well-disperse porogen in low- $k$  solution and hybrid low- $k$  film will be described. To further reduce the dielectric constant down to 2.0, we adjust the different the porogen loading (10 to 50wt%) to increase the porosity. The pore size, dielectric constant and mechanical strength of different porosity porous low- $k$  films with and without surfactant modification will be elucidated.



## 1.2 Overview

This thesis is organized into seven chapters. The contents of each chapter are as follows. Chapter 2 reviews the technology options, low- $k$  materials, and the challenges of porous ultra-low- $k$  dielectrics including aggregation and dispersion of porogen. Chapter 3 covers the experimental methods and instrumentation. Chapter 4 discusses the aggregation and diffusion of porogen in the low- $k$  MSQ/SBS hybrid films during thermal profile. Chapter 5 further addresses the dispersion of porogen in the hybrid

low- $k$  film by using different ionic surfactant to modify the porogen surface. Chapter 6 discusses the dielectric constant, pore geometry and mechanical strength on different porosity porous film with and without porogen modification. Finally, Chapter 7 summarizes key results in this study.



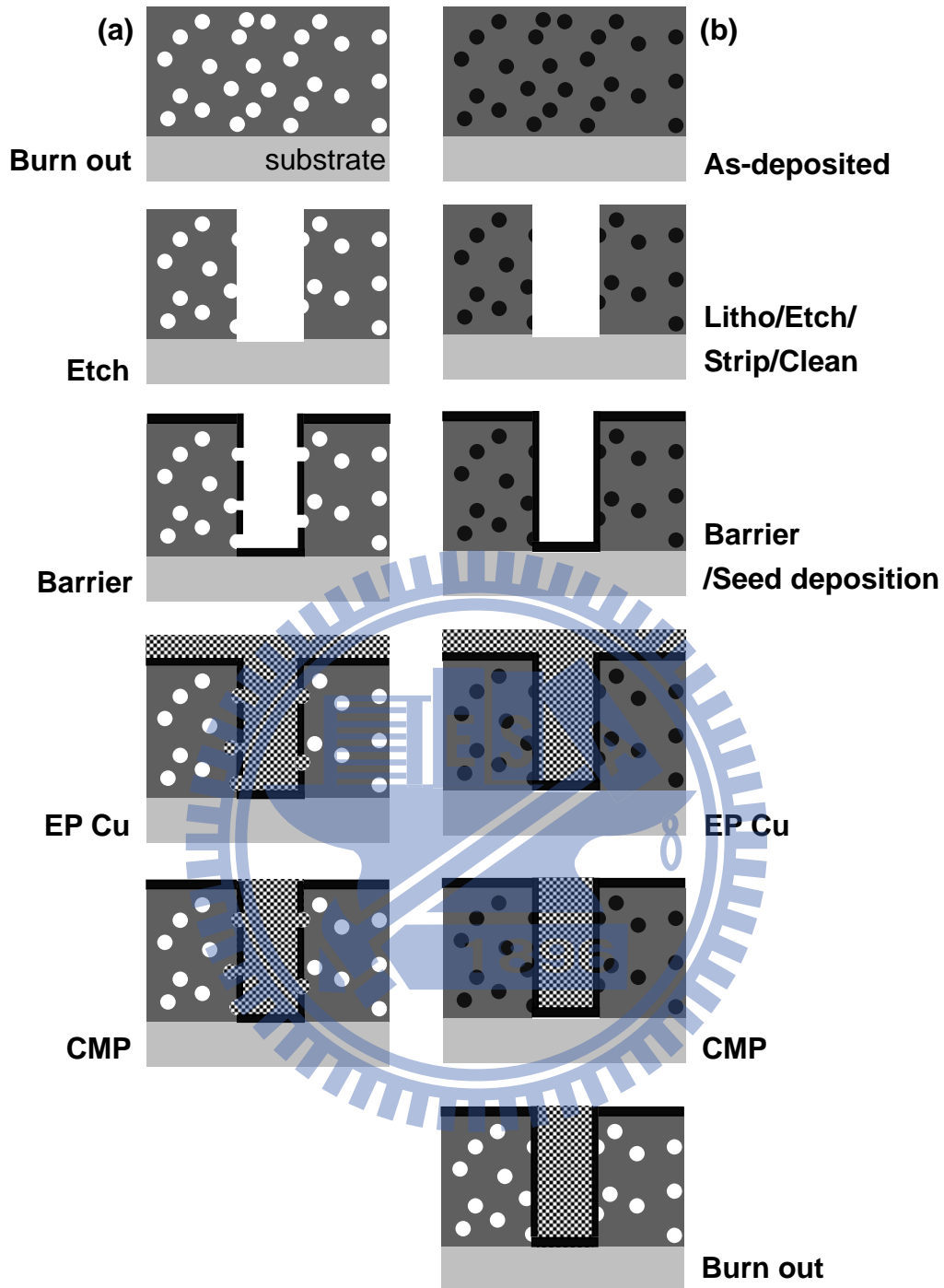


Figure 1.1 Formation schemes of porous low- $k$  dielectrics in copper/low- $k$  interconnects:

(a) immediately after ILD deposition and (b) post-integration porogen removal scheme after Cu CMP step forming a copper/low- $k$  layer.

# Chapter 2

## Literature Review

According to Moore's Law [17,18], “the number of transistors that can be placed inexpensively on an integrated circuit(IC) has increased exponentially, doubling approximately every two years“. The future development of integrated electronics or microelectronics depend on the continuous miniaturization allowing more components and more functions to be installed per unit area as shown in Figure 2.1, predicted by 2009 International Technology Roadmap for Semiconductor (ITRS) [19]. Figures 2.2 shows the trend of various device gate lengths scaling, including Flash, DRAM and MPU/ASIC microelectronics products, as predicted by ITRS. However, the continuous feature size shrinking has brought attention to several interconnected issues, such as RC delay, crosstalk noise, and power dissipation. Chapter 2 offers an overview of the development of backend interconnect technology and low- $k$  materials. In addition, the porous low- $k$  materials play an important role in the backend interconnects. The needs, materials, pore generator (porogen) and challenges of ultra-low- $k$  dielectric materials are also briefly reviewed.

## 2.1 Backend interconnect challenges

The impact of interconnects scaling can be examined by RC delay of multilevel interconnects. Figure 2.3 shows the typical schematic interconnect cross-section with parasitic capacitance. The size reduction in line and space width of metal enlarges metal line resistance and parasitic capacitance, resulting in serious impact on signal propagation delay and crosstalk noises between metal lines of interconnect. Since one of the major signal delays is associated with interconnect delay, RC delay have become our main concern. Generally, RC delay can be described according to Figure 2.3. By assuming the minimum metal pitch is twice the metal width (W) and the dielectric thickness between the metal lines is the same as the metal height (T), the following equation can be used to predict and calculate the RC delay respectively [20,21].

$$R = \rho \frac{L_m}{W t_m} \quad (2.1)$$

$$C = 2(C_L + C_V) = 2k \left( \frac{L_m t_m}{W^2} + \frac{L_m W}{T_m} \right) \quad (2.2)$$

$$\tau = RC = 2\rho k \left( \frac{L_m^2}{W^2} + \frac{L_m^2}{t_m^2} \right) \quad (2.3)$$

Where R is the resistivity,  $L_m$  is the interconnect line length, W is the interconnect line width,  $k$  is the permittivity, and  $t_m$  is the thickness of metal. Continuous scaling down



for achieve higher packing density will lead to the size reduction of  $W$  and  $t_m$ , that will induce higher RC delay. Therefore, according to above RC delay approximation equation, proper improvement of RC delay can be achieved by modification of resistivity ( $\rho$ ) of metal line and relative dielectric constant ( $k$ ) of inter dielectric layer (ILD). In the early dawn of integrated circuit era, the combination of aluminum (Al) alloys with  $\rho = 3.3 \mu\Omega\text{-cm}$  and silicon dioxide ( $\text{SiO}_2$ ,  $k = 4.0$ ) dielectric has been utilized extensively for interconnect of semiconductor industry. It is because of their mature subtractive dry-etch processes, and for Al interconnect the production compatibility with fabricated device which have no performance issues. Even so, the relentlessly ICs scaling toward smaller geometry size for improvement of higher integration density and higher speed, demands on the introduction of new material and integration. Beyond 250 nm node, Al/SiO<sub>2</sub> interconnects system was no longer sufficient materials to fulfill the device geometry shrinkage requirement as shown in Figure 2.4 [22]. In order to overcome above mentioned problems, new materials with low resistivity and low dielectric constant for use as metal line and ILD materials were urgently studied and developed. Copper (Cu) interconnect was pronounced as one of the most prominent metallization. Cu interconnect is then widely developed due to its low resistivity of  $\rho = 1.9 \mu\Omega\text{-cm}$ . Lower interconnect delay is gained from Cu/low- $k$  interconnect system compare to Al/SiO<sub>2</sub> interconnect system, utilizing 37 % lower

resistivity of copper than aluminum [22]. The capacitance of interconnect is dominated by line-to-line capacitance. Therefore, lowering dielectric constant (capacitance) was indeed crucially needed after the implementation of copper metallization.

The copper dual damascene process has been extensively adopted in the production line, but no consensus exists about the preferred IMD material for 22 nm technology node and beyond. In fact, the implementation of backend interconnect with a required effective dielectric constant ( $k_{\text{eff}}$ ), which involves the  $k$ -values of dielectric, barrier, and etchstop layer and their respective dimension (thickness, width), was continuously revised and relaxed by ITRS year to year as shown in Figure 2.5 [23]. In recent years, some of integration strategies and materials development have been proposed to further reduce the  $k_{\text{eff}}$  smaller than 2.0, such as air-gap [24], carbon nanotubes [25], and graphene nanoribbons [26]. However, it is not easy to successfully integrate these new materials in the near-term because the industry has to radically change the conventional integration and process modules of backend interconnect. In addition, according to the 2010 ITRS, IMD materials with a bulk dielectric constant ( $k_{\text{bulk}} \leq 2.2$ ) are expected to be used in 2013. So far, the manufacturability solution for 20 nm and beyond is not clear. Therefore, the search for low- $k$  materials with  $k_{\text{bulk}} < 2.2$ , or even  $< 2.0$ , is imperative for semiconductor industry and academia. This study focuses on the reducing of ILD  $k$ -value by controlling the structure-property relationship of novel type low- $k$  materials,

and while maintaining the conventional backend interconnect processes.

## 2.2 Classification of dense low- $k$ materials

Generally, the major deposition techniques for formation of ILD are divided into primary chemical vapor deposition (CVD) also known as “dry” process which has been widely adopted by chip manufacturers and showed highly reliable. The second one knows as “wet” process called spin-on method which has not been greatly developed in the process. There are some trade-off between CVD method and spin-on method. Spin-on process simply involves the coating of liquid/viscous precursor on the substrate before final curing to remove the solvent. It provides planarizing property that shows in a smoother surface which is highly desirable, and the cost is cheaper. Table 2.1 listed the CVD and spin-on of various ILD materials with their dielectric constant value. Compare to CVD method which involves various gases flow and deposit on the substrate even though it also provides better conformal coverage of the topography, the spin-on method benefit on cleanliness and minimal waste production. Therefore, the spin-on method was selected to study the structure-property relationship of novel low- $k$  materials in this dissertation. Then, next section will introduce the some of potential low- $k$  materials.

### 2.2.1 Fluorinated Silicate Glass

The fluorinated silicate glasses (FSG) invented by Novellus System Inc and the FSG has dielectric constant value as low as  $k=3.6$ . FSG possesses lower dielectric constant than  $\text{SiO}_2$  due to incorporation of fluorine into  $\text{SiO}_2$  matrix film. Fluorine incorporation leads to a less dense, more porous film by creating voids in the  $\text{SiO}_2$  matrix. Typical FSG film matrix shows in Figure 2.6. Replacing Si–O in the  $\text{SiO}_2$  matrix with Si–F reduces the polarizability of the matrix. The above reasons contribute to a lower dielectric constant of the FSG dielectric layer. [27, 28] FSG film has some drawback, for instance SiOF film is hydrophobic, in the meantime the fluorine atom will tend to react with hydrogen atom from water absorb in the release of HF moisture when heated to elevate temperature. The moisture of HF will travel along the interface of ILD and metal causing adhesion become poorer as explained by Figure 2.7. [29]

### 2.2.2 Carbon-doped Oxide (CDO)

Basically, CDO manage to utilize the chemical vapor deposition (CVD) processing method. CDO low- $k$  is also often designated as SiCOH (carbon-doped silicon oxide). The CDO matrix exists organic bonding such as  $\text{CH}_3$  backbone that concern lower polarizability in comparison to Si–O as shows in Figure 2.8. Instead of lower polarizability,  $\text{CH}_3$  also reduce the density of matrix by induced the matrix steric

hindrance. Regardless of the precursor used, SiCOH can reach  $k$  value in the range of 2.4-3. The  $k$ -value depends on the number of  $\text{CH}_3$  groups build into the structure. The widely studied precursor for SiCOH low- $k$  have been deposited by CVD methods were monomethylsilane (1MS), dimethylsilane (2MS), trimethylsilane (3MS), tetra-methylsilane (4MS), Hexamethyldisiloxane (HMDSO), bis-trimethylsilylmethane (BTMSM), tetravinyltetramethylcyclotetrasiloxane (TVTMCTSO), Vinyltrimethylsilane (VTMS), and tetramethylcyclotetrasiloxane (TMCTS) [30,31,32,33,34,35,36] as shows in Figure 2.9. CVD CDOs are mainly use in 90nm node. Commercially, the most common CVD OSG materials are Aurora<sup>TM</sup> ( $k=2.9$ , ASM), Coral<sup>TM</sup> ( $k=2.85$ , Novellus), Black Diamond<sup>TM</sup> ( $k=2.65-3.0$ , Applied Materials).

### 2.2.3 SiLK<sup>TM</sup>

Spin-coated base SiLK<sup>TM</sup> was an organic polymer dielectric founded by Dow Chemical in mid 1997. In April 2000, IBM reported the complete integration of SiLK<sup>TM</sup> dielectric and copper wiring, and announced its intent to commercially fabricate integrated circuits using SiLK<sup>TM</sup> resin. Toshiba/Sony and Fujitsu also accommodated SiLK resin with hybrid stacks. Aromatic thermosetting polymer SiLK<sup>TM</sup> with  $k=2.65$  has been proved its compatibility with Cu-dual damascene 0.13  $\mu\text{m}$  technology node system [37]. However, the relatively weak mechanical properties ( $E \sim 3\text{GPa}$ ) of SiLK<sup>TM</sup>

and its poor mismatch of coefficient of thermal expansion (CTE: 66 to 165 ppm/°C) with copper wires and substrates have prevented a wide adoption of SiLK™ in high-volume semiconductor manufacturing. Structure repeating unit of organic SiLK™ shows in Figure 2.10 [38].

#### 2.2.4 Silsesquioxane based materials

Silsesquioxane (SSQ) based low- $k$  material or commonly called T-resin are organic-inorganic polymer with empirical chemical formula  $(R-SiO_{1.5})_m$ . The substituents (R) can include hydrogen, alkyl, alkenyl, alkoxy and aryl. Figure 2.11 illustrates the structure of basic units of SSQ [39]. The contribution of organic substituents benefits in lowering the dielectric constant because they provide lower density of the matrix structure. For the addition, they also attributed to less polarizability organic bond (Si-CH<sub>3</sub>) compare with Si-O bonds in SiO<sub>2</sub>. SSQ based low- $k$  materials is also one kind of organosilicate glasses (OSG) which yield  $k = 2.5-3.3$  after curing step [40,41,42]. The common used SSQ based materials for microelectronic application are mainly hydrogen-silsesquioxane (HSQ) and methyl-silsesquioxane (MSQ). HSQ has hydrogen as a terminal group and MSQ has methyl as a terminal group. The contribution of larger -CH<sub>3</sub> group that will cause steric hindrance rather than smaller -H group will lower the density of the matrix. Besides, the Si-CH<sub>3</sub> bond

possesses less polarization compare to Si-H. Therefore, MSQ material has lower dielectric constant than HSQ material. Table 2.2 summarizes the principle properties of SSQ based dielectric materials compare with SiO<sub>2</sub>. Subsequently, the commercially available SSQ based low- $k$  materials are summarized in Table 2.3 which has  $k < 3.0$ . [43,44]

## 2.3 Porous low- $k$ materials

The above mentioned low- $k$  materials were all classified into dense low- $k$  materials. In fact, an ultra-low- $k$  material with  $k$ -value  $\leq 2.0$  is difficult to obtain even though the porosity is increased, and fully densified materials has seemingly reached their lowest capability.. Figure 2.12 shows ideal cases for a dry film, which are quite different from typical experimental values [45]. Therefore, the research has to move on with introduction of porosity into the dense materials, which is the only way to achieve dielectric constants  $< 2$ . Pores can be any shapes and morphology, including cylindrical, spherical and plate. Pore size, according to the International Union of Pure and Applied Chemistry (IUPAC) [46], is defined as follows:

Macroporous with dimensions  $> 50$  nm;

Mesoporous with dimensions of 2~50 nm;

Microporous with dimensions  $< 2$  nm.

The major of porous materials is considered for ILD applications are classified as mesoporous. That is, the average pore size in many candidate porous materials ranges from about 2 to 10 nm. There are two type pore formation inside the dense low- $k$  matrix. The primary one is that pores are inherently formed inside the matrix through sol-gel process such as aerogel and xerogel low- $k$  film. The secondary method of pores formation is though the template agent or pore generator (porogen) which accommodates the present of sacrificial materials that are decomposed upon the thermal process. Following, we will discuss the fact and issue of each porous low- $k$  materials.

### **2.3.1 Silica aerogel and xerogel low- $k$ dielectrics**

SiO<sub>2</sub> aerogel thin film has attracted significant attention because of their unique properties such as ultralow dielectric constant, high porosity, and high thermal stability. SiO<sub>2</sub> aerogel thin films usually take the advantage of aging processes. However, SiO<sub>2</sub> aerogel thin films usually synthesis above the supercritical pressure (> 60 bar) and high temperature of drying solvent process, which is very expensive and hazardous. Thus, it will become constraint for the production in industrial application [47]. Due to their high porosity, SiO<sub>2</sub> aerogel thin film have not display superior mechanical properties [48]. SiO<sub>2</sub> xerogel thin films also employ the same aging technique as SiO<sub>2</sub> aerogel thin film. The differences between aerogel and xerogel is SiO<sub>2</sub> xerogel prepared by the



ambient drying process which involve pre-drying step that called surface modification process known as silylation. The intention of silylation process is to change the surface hydroxyl ( $-OH$ ) groups into inert methyl ( $-CH_3$ ) groups. This procedure ensure the film absorb minimal moisture from the environment [49]. Both  $SiO_2$  xerogel and aerogel has been reported to reach  $k$ -value  $< 2$  at porosity level of 70~90% [50,51,52,53].

### 2.3.2 Pure Silica-Zeolite low- $k$ film

PSZ low- $k$  film offers several advantages over amorphous silica including crystalline structure as well as intrinsically uniform and small pore size [54,55]. Typical PSZ materials have high modulus and low dielectric constant, but have challenges such as high surface roughness [56], which can be resolved by adding a chemical mechanical polishing step. The other major problem is the high moisture absorption of PSZ film [57,58]. This is disadvantageous for the practicability of PSZ film due to the  $k$ -value of water is close to 80. Therefore, there have been some efforts to overcome this problem, for example, by performing fluoro-organic functionalization or silylation using 1H,1H,2H,2H-perfluorooctyltriethoxysilane, 3,3,3-trifluoropropyltrimethoxysilane [59], trimethylchlorosilane (TMCS), hexamethyldisilazane (HMDS) [ 60 ], and/or methyltrimethoxysilane (MTMS) during the zeolite synthesis and/or during heating processes to make the surface more hydrophobic [61,62].

### 2.3.3 Nano-Clustering Silica (NCS)

A novel pore forming method based on spin-on nano-clustering silica (NCS), schematically illustrated in Figure 2.13 [63]. The nano-clustering silica, a MFI-type zeolite film was prepared by sol-gel method. NCS precursor prepared by mixing main matrix of silica source tetraethoxysilane (TEOS) as a soldier in the existence of organic structure directing agent such as tetrapropylammonium hydroxide (TPAOH) as a commander in the present of appropriate solvent such as ethanol. The hydrophobicity of the surface of precursor was modified by adding alkoxysilane (AS) such as methyltrimethoxysilane (MTMS) as a component of the matrix. The difference between pure zeolite low- $k$  and NCS is the addition of methyl ( $-\text{CH}_3$ ) groups directly into the precursor.

### 2.3.4 Templated-type (porogen) low- $k$ dielectrics

Furthermore, the incorporation of thermally-labile pore generator also can produce porous low- $k$  thin film. The removal of porogen upon high temperature heating will be replaced by pores inside the matrix. First method, incorporation of porogen into the low- $k$  matrix can be accomplished by simply dispersing or mixing the porogen into the solution of low- $k$  precursor [64,65,66]. Porogen size determines the final pore size that

exists inside the matrix. Percentage of porogen added or also called porogen loading determines degree of porosity inside the final cured matrix [67,68]. However, during thermal heating process, the random distribution of pores tends to agglomerate and coalescence which cause a burden to the mechanical strength of final low- $k$  film especially when the porogen loading is increased as shown in Figure 2.14 [69,70].

Recently studies have shown that various polymers could be applied in the SSQ based matrix to form more ordered pore size and pore shape with narrower pore size distribution will be described in Section 2.4.

## **2.4 Selection of porogens**

### **2.4.1 Linear amphiblic block polymer**

Regarding to their ability to self assembly and form micelle as showed in Figure 2.15 [71], block copolymers have become one of the promising candidates for low- $k$  dielectric. Amphibilic di-(or tri-) block copolymer such as PEO-b-PPO-b-PEO [71], PS-b-PEO [72], PS-b-P2VP [73], PS-b-P4VP [18], etc have been studied widely. However, these polymers exhibit very limited miscibility with MSQ precursors, which results in severe phase separation depending on their loading levels, and in large, interconnected pores in cured MSQ dielectrics. However, with increases in the porosity, the pore size increases and the pore size distribution broadens, indicating that the

generated pores change from closed-cell structures to interconnected bicontinuous structures, which is attributed to changes in the phase separation of the blends of the porogen and matrix components with changes in the blend composition [74]. The pore size and size distribution are also found to be affected by the numbers of hydroxylsilyl and alkoxysilyl groups in the PMSSQ precursor. Moreover, neutron reflectivity measurements on these porous films found localized higher porosities at the interface between the porous films and their silicon substrates [75].

#### **2.4.2 Dendrimers polymer**

Dendrimers possess three distinguishing architectural components an initiator core, interior layers, and terminal end groups [76,77], and consist of a well-defined, highly branched, compartmentalized structure that is spherical in shape and of nanometre scale. However, both dendrimer porogens and dielectric materials must meet the following requirements if they are to be used to successfully fabricate low- $k$  dielectrics containing closed nanopores. Firstly, the dendrimer porogen should thermally degrade at temperatures lower than the degradation temperature of the dielectric material. Secondly, the dielectric material component must be dimensionally stable or become dimensionally stable during the thermal processes required to burn out the dendrimer porogen component from the dielectric film and in the fabrication of ICs. Thirdly, the

dendrimer and dielectric components should homogeneously dissolve in a mutual solvent without any phase separation. Fourthly, the components must be highly miscible to prevent or minimize any unfavorable phase separation during film formation processing, i.e., solution casting and subsequent drying processes. Finally, both the dendrimer and dielectric components must retain their miscible state without any unfavorable phase separation until the dendrimer porogen is thermally burned out during the post-thermal processing of the dried film, at which point the imprints of the dendrimer molecules are created as nanopores in the resulting dielectric film. The dendrimers were found to be miscible with the PMSSQ precursor, and their sacrificial thermal decompositions result in closed, spherical nanopores in the cured PMSSQ dielectric thin films as showed in Figure 2.16 [78].

### 2.4.3 Star-shape polymers

Star-shape polymers are very attractive as porogens for imprinting closed nanopores in dielectrics because of their spherical shape in the nanometre size range. Some aliphatic star-shape polymers that completely decompose at temperatures  $< 400^{\circ}\text{C}$  even in an inert atmosphere have been reported, such as star shape poly( $\epsilon$ -caprolactone)s (PCLs) [79, 80, 81] as showed in Figure 2.17. Among the star-shape polymers PCLs have been extensively investigated for use as porogens in

SSQ dielectrics because of the following chemical characteristics. PCL polymers consist of non-polar pentylenyl and polar ester segments in each repeat unit in the backbone. In addition, they have hydroxyl groups at their arm ends. The PMSSQ dielectric precursor contains hydroxysilyl and alkoxysilyl groups. The PCL polymers are therefore likely to be miscible with the MSQ precursor. Star-shape PCLs with 4–48 arms have been reported. By increasing porosity, star-shape PCL porogens have a tendency to aggregate that is worsened by the cross-linking of the MSQ precursor matrix. Other star-shape porogens exhibit similar problems [82].

#### 2.4.4 Cage supramolecules

Cyclodextrins (CDs) are cyclic oligosaccharides consisting of at least six glucopyranose units joined together by an  $\alpha$ -linkage:  $\alpha$ -cyclodextrin ( $\alpha$ -CD) (6 glucose units),  $\beta$ -cyclodextrin ( $\beta$ -CD) (7 glucose units), and  $\gamma$ -cyclodextrin ( $\gamma$ -CD) (8 glucose units) (Figure. 2.18) [83,84]. They are composed of a hydrophobic interior and a hydrophilic exterior; in particular, the hydrophilic exterior may produce favorable interactions with dielectric materials with polar characteristics. These aliphatic compounds are thermally labile cage supramolecules with a maximum diameter of 1.5–2.0 nm. However, the loadings of > 50 wt% were also found to generate wormlike and interconnected pores, as observed for the porous silicates imprinted with CDs.

### 2.4.5 Well-dispersion porogen

Every porogen will meet a large issue is the aggregation in the hybrid film. Recent studies demonstrated that significant porogen diffusion and aggregation occurred under slow curing condition and resulted in larger porogen size in the MSQ/porogen hybrid film [85]. The rapid curing rate could achieve smaller porogen size and tighter distribution by rapidly forming a cross-linked low- $k$  matrix to freeze up porogen aggregation sterically. But the rapid curing method also lead to residual stress in the porous thin film [86]. Thus, the dispersion of porogen and its impact on the aggregation behavior of porogens prior to the formation of a cross-linked low- $k$  matrix are interested. The huge amount of research concerning particle dispersion in colloids shows that the state of the dispersion can be modified, for example, by a highly charged, sterically stabilized polymer and pH value to obtain a high-stability dispersion with the electrostatic and steric effect [87,88,89,90,91]. In this study, we will report the well-dispersion porogen in the solution and hybrid low- $k$  films.

### 2.4.6 Reactive polymers

The special approach as reactive-porogen method has been proposed to overcome the aggregation of porogen. The reactive porogen were grafted on the low- $k$  matrix

during synthesized scheme by using the sol-gel reaction [92] or atom transfer radical polymerization (ATRP) [93] as showed in Figure 2.19. This method can control the position of porogen in the hybrid film. During processing and film formation, it is also critical that phase separation between the porogen and the low- $k$  matrix occurs during vitrification and that the size scale of kinetic phase separation be limited. On the other hand, the pore size is controlled in the porous film due to the porogen can not diffuse and aggregate in the hybrid film. In general, the grafted porogen will form the small and uniform pore size in the porous film after removal process [93]. Yet, the disadvantage of reactive-porogen method is a complicated scheme for forming the hybrid low- $k$  film and the porogen can not be grafted fully at low- $k$  matrix. There are large numbers un-grafted porogen in the hybrid film causes the porous film hard to appear high porosity (typical  $\leq 20$  vol.%) [94,95]. For example, the loading of PCL porogen mixing in the matrix from 10 to 20 wt%, the pore sizes are ranging from 5.3 to 14.2 nm. On the other hand, the reactive-poregen PCL of 10 and 20 wt% loading is grafted on the MSQ matrix, the pore sizes are ranging from 5.2 to 10.0 nm. That indicates the reactive-porogen will form smaller pore size than the mixing process. When the loading of reactive-porogen PCL rises to 30~40 wt%, the pore size will range from 15.1 to 17.1 nm. The results show the reactive-porogen is also occurs the aggregation by increasing porogen loading due to the porogen can not be grafted fully at low- $k$  matrix as



summarize in the Table 2.4 [10]. In addition, Table 2.5 shows the characteristics of the other reactive-porogen on MSSQ based low- $k$  material.

## 2.5 Challenges in porous low- $k$

As reviewed above, there are two principal methods for producing the templated-type (porogen) low- $k$  dielectric materials containing closed nano-pores, which are the most promising inter dielectric layers for the production of advanced ICs by the semiconductor industry. One method is the mixing of porogen and matrix in solvent to form the precursor and hybrid low- $k$  film. The second is chemically linking the relative-porogens to the network polymers as block components of the backbone or through grafting. Finally, the porogen template approach requires that the dielectric matrix film has a higher degree of cross-linking so that it is dimensionally stable when the pores are created. The porous structure is therefore affected by any further processes associated with the resulting nanoporous dielectric film; this is why silicate and organosilicate precursors and their cured dielectrics are appropriate for the porogen template approach to producing low- $k$  nanoporous dielectrics. Thus, the study focus on the SSQ based materials as dielectric matrix. Because of the reactive-porogen method is too complicated and hard to deliver high porosity (typical < 20 wt% loading of porogen); the mixing process of porogen and matrix is paid close attention in this study.

However, there are some practical requirements if these relationships between the sacrificial porogens, imprinted pores and porosity are to be maintained. Firstly, the sacrificial porogen should be compatible with the dielectric matrix material in order to avoid porogen aggregation. Secondly, the sacrificial porogens should be uniformly distributed throughout the film volume in order to avoid the coalescence or interconnection of the pores.

### 2.5.1 Pore size

Porous materials will pose even greater challenges to both characterization and integration. Some key material properties directly related to integration issues include pore size, distribution and structure. The average pore size in a low- $k$  porous dielectric layer film must be smaller than the smallest device feature; the minimum metal feature size is nowadays approaching 22 nm and may reach 13 nm in the near future. The pore size distribution (uniform vs. random) may affect the mechanical property of the low- $k$  film. Mechanically, the low- $k$  layers must be strong enough to endure at least the CMP process. The elastic modulus, hardness must be high enough to prevent cohesive failure, cracking or delamination. The minimum requirement of modulus for pass the CMP process is 4 GPa, and hardness has to be larger than 0.5 GPa [96]. An isolated pore structure is often preferred to interconnected pore structure since interconnected pore

may create leakage current paths [97] and have an adverse effect on the mechanical strength. In past paper, the density of the elastic strain energy increases as the pore size decreases. On the other hand, the effective bulk elastic modulus of nanoporous structures with small pore size is larger than that of nanoporous structures with large pore size [98]. Thus, the smaller pore size plays an important role in the porous low- $k$  film. In this study, the post-integration porogen removal approach is proposed to form the porous low- $k$  film. The property of hybrid low- $k$  film will be discussed due to the pore size, distribution, and structure depends on the porogen behavior in the hybrid film before burning out. We will introduce the basic porogen behavior in next section.

### **2.5.2 Porogen dispersion**

However, the pore size was affected significantly by porogen size in the precursor and hybrid film before burning out step. The diffusion and aggregation of porogen will form many large mass in the hybrid film and later larger pore in the porous film. The mixed system of low- $k$  precursor contains the matrix, porogen, and solvent. A homogeneous and uniform solution is recommended a well low- $k$  precursor. The solvent evaporates from the precursor with increasing temperature in which that may be causes the phase separation of porogen and matrix. Significant porogen aggregation occurs in this tern due to the porogen diffuse in the incomplete cross-linking matrix. The isolated

porogen polymer regarded as a nano-particle, and porogen will diffuse and aggregate in the system. In general, the forces of inter-particle including attraction or repulsion will affect the behavior of the particle as showed in the Figure 2.20. There were the repulsive force ( $V_R$ ) and attractive force ( $V_A$ ) between two particles. The  $V_R$  indicates the electrostatic forces and steric effect, and that lead particles to exclude the other particles. On the contrary, the  $V_A$  indicates the van der Waals force, and that lead particles to attract each other [99,100,101]. When two particles approached each other from infinite space, the energy amount ( $V$ ) could reach to minimum after passing through the energy barrier ( $V_{max}$ ). However,  $V_R$  is raised will lead  $V_{max}$  increased and the particles difficult to approach the other particles. Thus, the increased of electrostatic forces and steric effect can prevent the porogen aggregation. The study will focus on the dispersion of porogen before removal process. A novel method is proposed to increase the electrostatic forces of porogen and control its size in the hybrid film. Finally, that will remain the smaller pore size in the porous film.

### 2.5.3 Porogen loading and high porosity

According to 2010 ITRS, upcoming 22 nm technology node of IC industry requires dielectric materials with  $k$ -value  $< 2.3$ , which requires an increase in free volume by incorporating porosity through nanoporous pores, as well as a reduction of polarizability.

For example, for a dense materials such as MSQ ( $k \sim 2.9$ ), a high porosity,  $\sim 60\%$  is required in order to obtain an ultra-low- $k$  porous MSQ of  $k \sim 2.0$ . In the porous low- $k$  films, the porosity is critical parameter controlling the dielectric constant, mechanical strength, and stress. Moreover, small and isolated pores with a tight pore size distribution are highly desired in order to achieve better mechanical strength and better barrier reliability because a conformal and continuous barrier can be formed onto such a porous low- $k$  film [102].

However, there is huge challenge in maintaining the pore size without aggregation or forming interconnected pores at high porosity. Many studies show that the pore size increases and pore shape becomes interconnected or elliptic with increasing porosity (or porogen loading) in the low- $k$  porous film [103,104]. Larger or interconnected pores at high porosity can significantly reduce the mechanical strength of porous low- $k$  film [71,105]. In addition, closed nanopore can be obtained, within certain boundary conditions related to the nature and total load of the porogen as summarized in the Table 2.5 [71,79,105,106,107,108,109,110,111]. The past study indicate the obvious aggregation of pore at porogen loading  $> 25\%$  and focus on the property of low- $k$  porous film with porosity  $< \text{about } 30 \text{ vol.}\%$  [69]. In this study, the porogen surface modification by ionic surfactant will be used to disperse porogen in the hybrid low- $k$  system. In addition, the porogen loading (or porosity) is also increased in the system.

The property of pore at high porosity (>30 vol.%) and the critical (or ideal) porosity with no-aggregated pore will be discussed.

## 2.6 Post-integration porogen removal scheme

The novel post-integration porogen removal approach, which detail integration scheme is illustrated in Figure 2.21, has been proposed based on material design and integration scheme to circumvent the reliability issues of porous dielectrics mentioned previous section. Malhouitre *et al.* [112] and Fayolle *et al.* [113] have demonstrated that such novel material and scheme could be achieved in a copper single damascene structure with a 25% RC reduction after porogen removal. Recently, post-integration porogen removal approach has been applied to reduce the plasma-induced damage to porous low- $k$  dielectrics because porogen can reduce effective pore size and limit the plasma radical diffusion inside pore [14,15]. For such a scheme, the decomposition temperature ( $T_d$ ) of high-temperature porogen candidates needs to be higher than the maximum processing temperature (> 350°C) with the post-integration porogen removal scheme [114]. Moreover, the mechanical strength of hybrid low- $k$  material should be strong enough to pass all of the backend processing steps, especially the chemical-mechanical polish (CMP) step. On the other hand, for such hybrid dielectrics or its porous form, there are additional concerns relate to moisture uptake induced by

processing steps such as CMP, post-etch cleaning, post-CMP cleaning or resist removal [115,116,117]. Therefore, the structure-property relationship of hybrid low- $k$  materials using in the post-integration porogen removal scheme will be further studied in this dissertation.

The thermal stability of the porogens used in the as-deposited porous low- $k$  film are typically not so high such that porogens can be removed readily to form porosity during dielectric deposition or subsequent thermal treatment. As for the high-temperature porogens in the late porogen removal scheme, it is desirable to attain a high and sharp decomposition temperature by incorporating stable structures such as aromatic rings or double/triple bonds as well as by using similar moieties in a block copolymer. For example, polystyrene-*b*-polybutadiene-*b*-polystyrene (SBS) and polystyrene (PS) could be chosen as a good high-temperature porogen candidate due to its similar aromatic structure which can provide a good thermal stability and desired decomposition temperature. The study focus on the porogen surface modification by using ionic surfactant, and the thermal stability of surfactant is required to consider.

Table 2.1 Type of ILD materials

Material	Dielectric constant	Deposition method
<b>Low-<i>k</i> materials</b>		
Polyimides	3.0-3.6	Spin-on
DLC (diamond-like carbon)	2.8-3.0	CVD
Hydrogen silsesquioxane (HSQ)	2.8-3.0	Spin-on
Black Diamond <sup>TM</sup> (SiCOH)	2.7-3.3	CVD
Spin-on glasses	2.7-3.1	Spin-on
Polyimide-SSQ hybrids	2.7-3.0	Spin-on
SILK <sup>TM</sup>	2.7	Spin-on
Fluorinated polyimides	2.6-2.9	Spin-on
Poly(arylene ethers)	2.6-2.9	Spin-on
Methyl silsesquioxane (MSQ)	2.6-2.9	Spin-on
Poly(arylenes)	2.6-2.8	Spin-on
Poly(norbornenes)	2.5-2.7	Spin-on
Fluorinated Parylene	2.5	CVD
<b>Porous dielectrics</b>		
Polyimide nanofoams	2.2	Spin-on
Mesoporous silica	1.9-2.2	Spin-on
Silica xerogels	1.5-2.2	Spin-on
Silica aerogels	1.1-2.2	Spin-on
(Source:IBM)		



Table 2.2 Principle properties of SSQ based dielectric materials

Property	MSQ	HSQ	SiO <sub>2</sub>
Dielectric Constant	2.8	3.0	4.0
Modulus (GPa)	3-5	6	59
Density (g/cm <sup>3</sup> )	1.2-1.3	1.4-1.5	2.4
Tensile Strength (MPa)	50	80	-

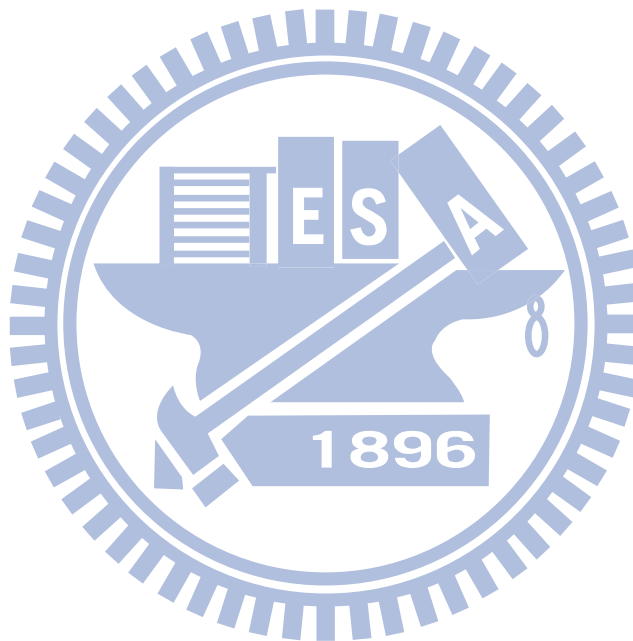


Table 2.3 Commercially available SSQ-based low- $k$  materials.

Material	Trade Name	$k$ -value	Company
HSQ	FOx (flowable oxide)	2.9-3.0	Dow Corning
MSQ	RZ25-15	2.6	Hitachi
MSQ	HOSP	2.6	Honeywell
Porous HSQ	XLK	2.2	Dow Corning
Porous HSQ	LKD 5109	2.2-2.3	JSR
Porous MSQ	Zirkon	2.3	Shipley

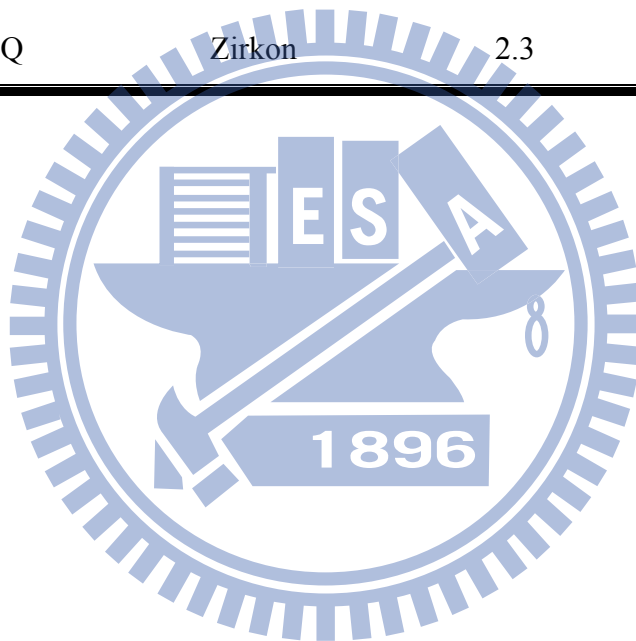


Table 2.4 The pore size (nm) from PCL porogen under different low- $k$  process

Method	Mixing-porogen	Reactive-porogen
10 wt% PCL	5.3	5.2
20 wt% PCL	14.2	10.0
30 wt% PCL	20.0	15.1
40 wt% PCL	--	17.1



Table 2.5 The property of reactive-porogen on SSQ-based low-*k* materials

Matrix	Porogen Loading(wt%)	Porosity (vol.%)	Pore size (nm)	Property	Ref.
MSQ	poly(caprolactone) 20 to 30	--	~20	high porosity but lager pore	C. Nguyen (2000) [92]
MSQ	PMMA 10 to 30	9.4 to 25.4	1.7 to 2.4	small pore but low porosity	H. W. RO (2005) [93]
MSQ	PMMA 20	< 20	10	low porosity	Andreas Heise (2000) [94]
MSQ	BTMSE 10 to 20	8 to 17	--	5 wt% porogen loading creates 4% porosity	W. Oh (2003) [95]

Table 2.6 The impact of porosity change on SSQ-based low-*k* materials.

Matrix	Porogen Loading(wt%)	Porosity (vol.%)	Pore size (nm)	Impact	Ref.
SSQ	PCL	30	~10	E drop to 2.41GPa	J. Hyeon-Lee (2004) [106]
SSQ	$\beta$ -Cyclodextrin 10 to 30	3-10 to 10-20	18.1 to 34.0	2 times pore size at 30% porosity	K. H. Lee (2006) [107]
MSQ	PCL 10 to 30	--	5~20	significant aggregation at loading > 20 wt%	C. V. Nguyen (1999) [79]
MSQ	P123 30 to 50	24 to 53	2.7 to 5.2	2 times pore size by increasing porosity	S. Yang (2001) [71]
MSQ	P123 15 to 50	--	2.9 to 14.3	Pore size increased 5 times	S. Yang (2002) [105]
MSQ	PMMA-PDMAEMA 10 to 50	--	9.5 to 60	large pore size~60nm	H.-C. Kim (2002) [108]
MSQ	TESNB 10 to 30	--	3 to 10	board distribution	A. M. Padovani (2002) [109]
MSQ	PS-PAA 10 to 50	--	2.7 to 10.1	4 times pore size by increasing porosity	Y. Chang (2004), [110]
MSQ	Linear polymer 20 to 50	29.7 to 60.6	2.2 to 7.6	2~3 times pore size by increasing porosity	H.-J. Lee (2008) [111]
	Star polymer 20 to 50	31.7 to 59.4	7.6 to 13.2		

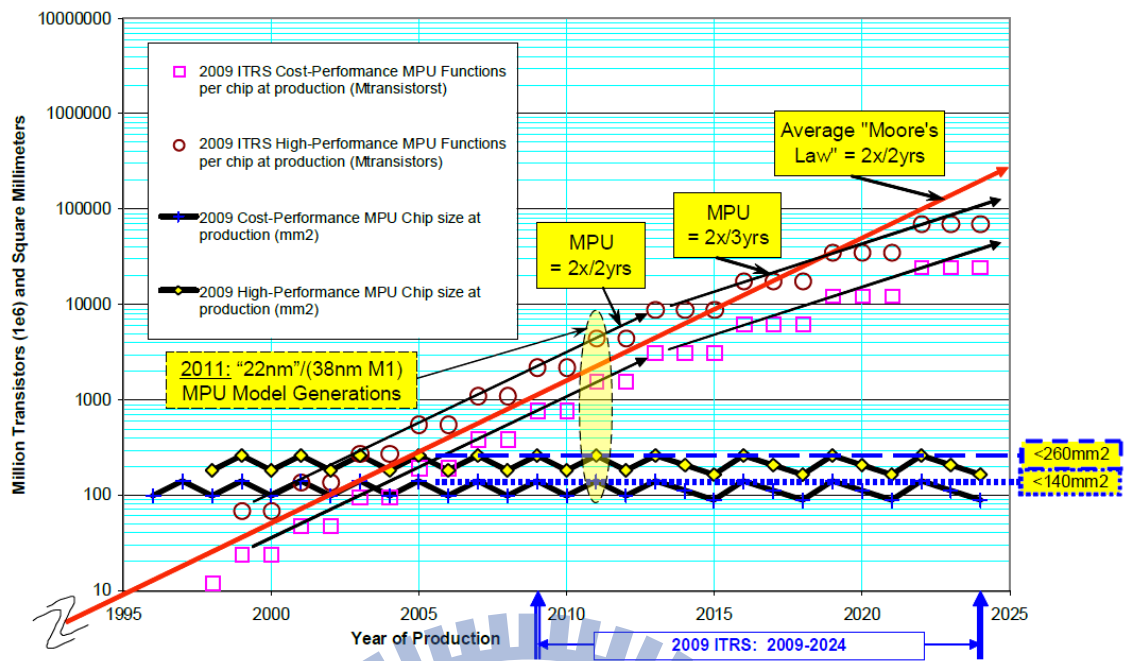
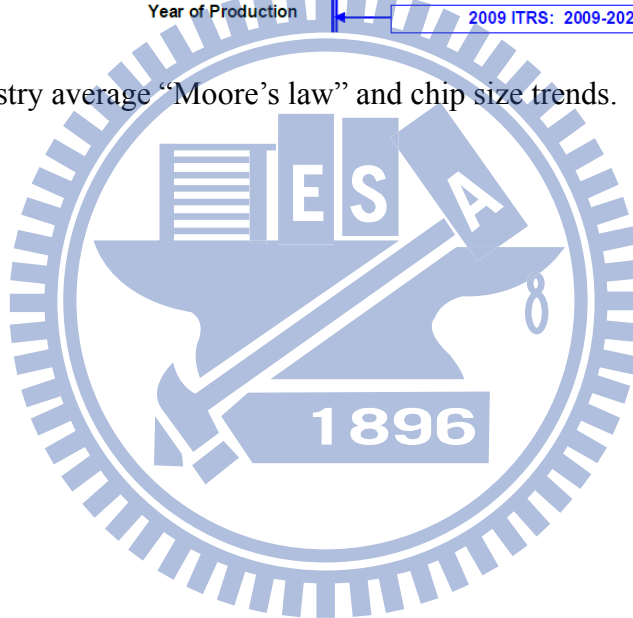


Figure 2.1 Industry average “Moore’s law” and chip size trends.



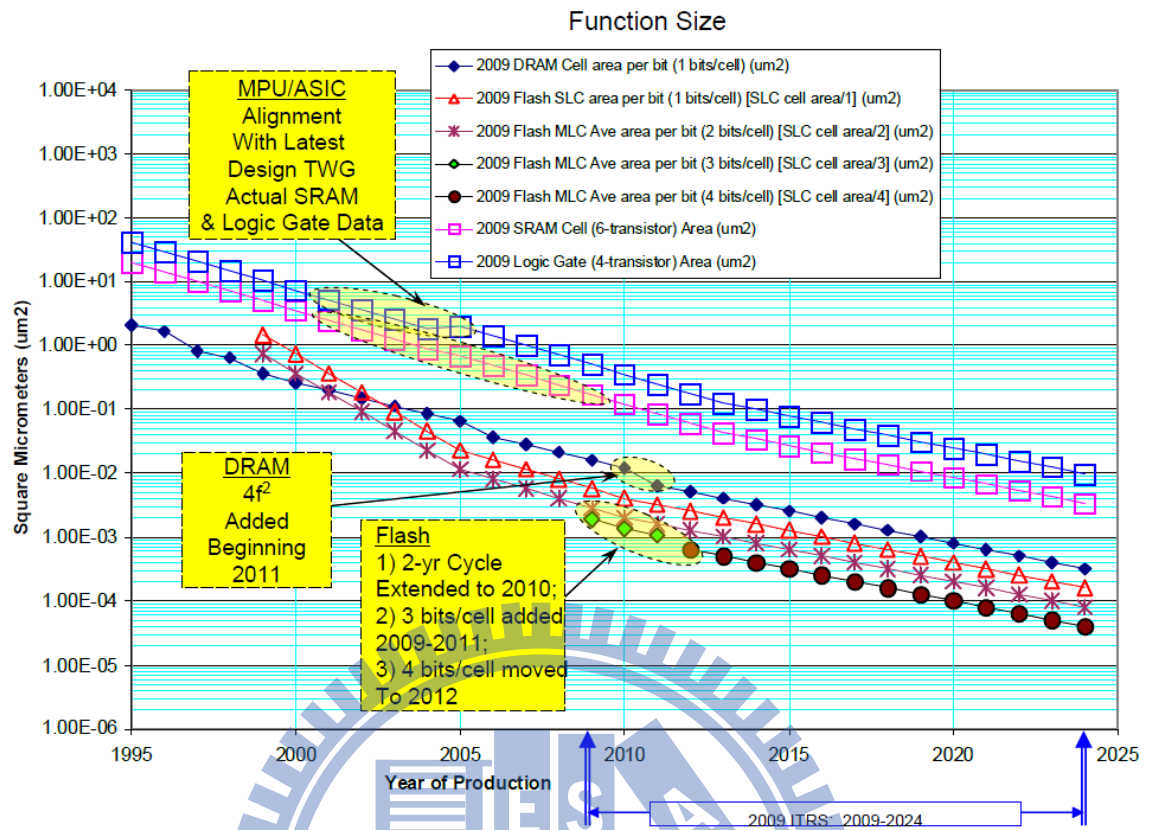


Figure 2.2 Device scaling projection trend shown in terms of gate length (half pitch) for Flash, DRAM, and MPU/ ASIC microelectronics products.

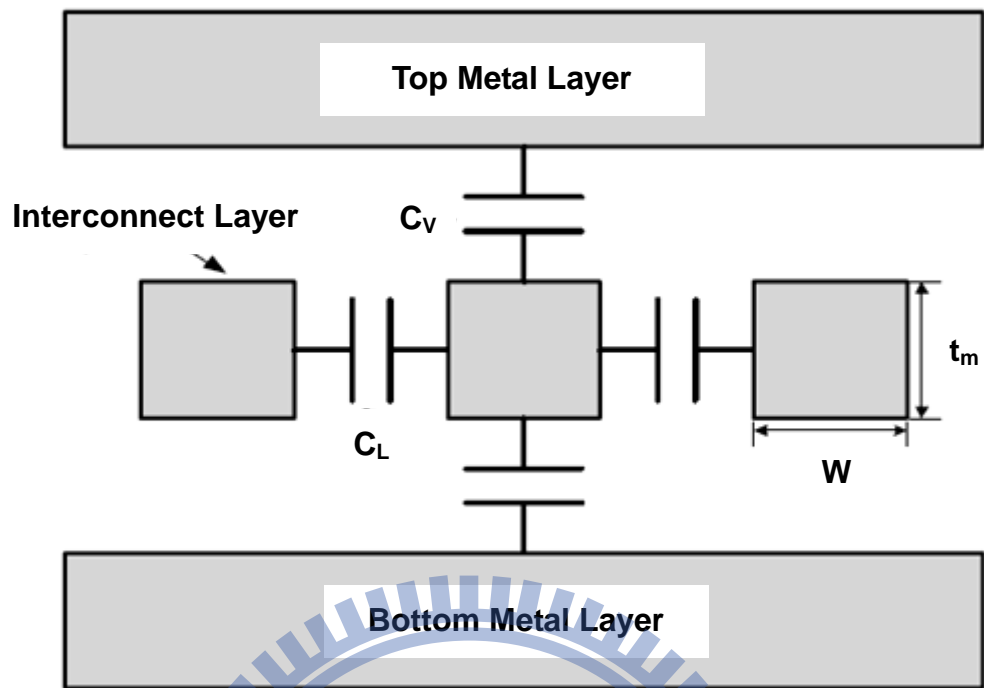


Figure 2.3 Typical schematic interconnect cross-section with parasitic capacitance



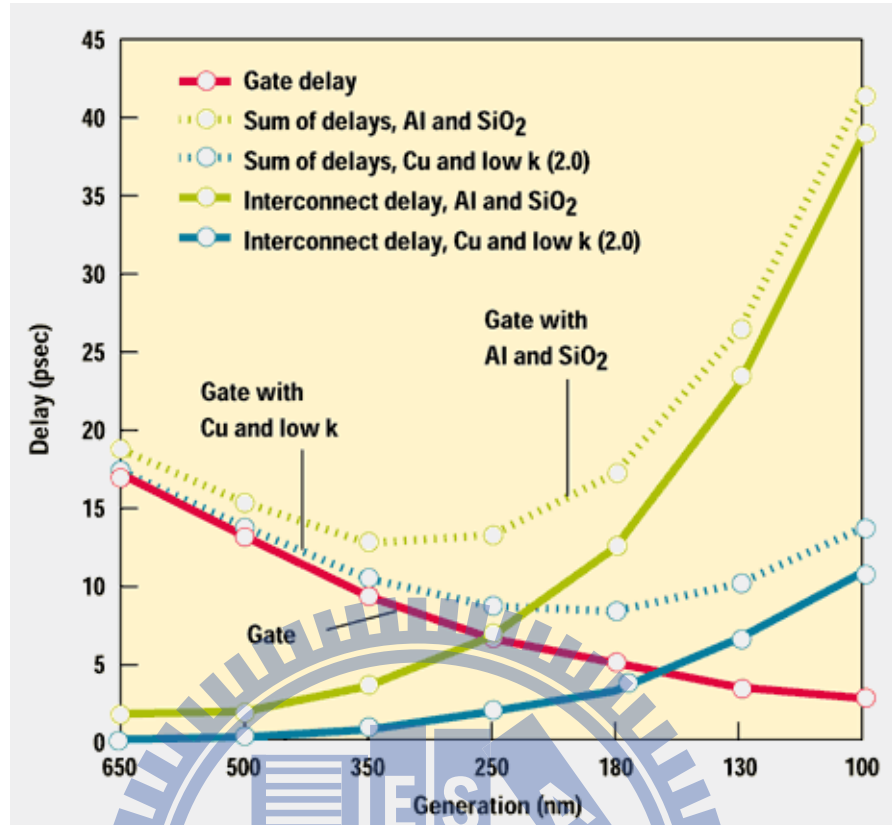


Figure 2.4 Decrease in interconnect delay and improved performance are achieved by using Cu and low- $k$  dielectric.

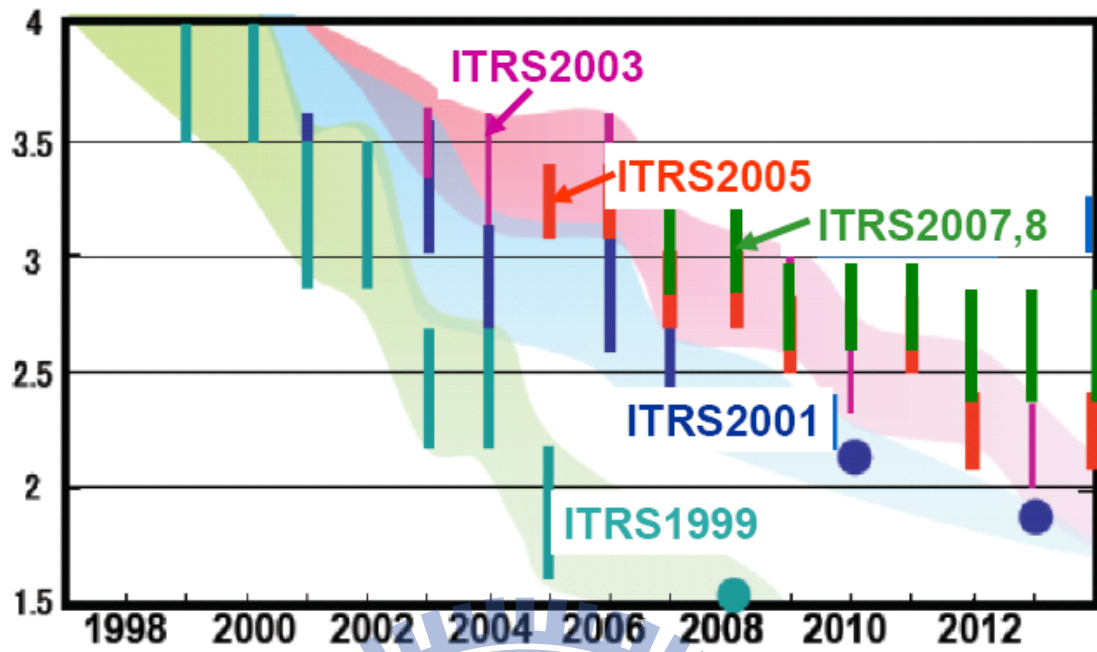


Figure 2.5 Historical transition of ITRS low- $k$  roadmap



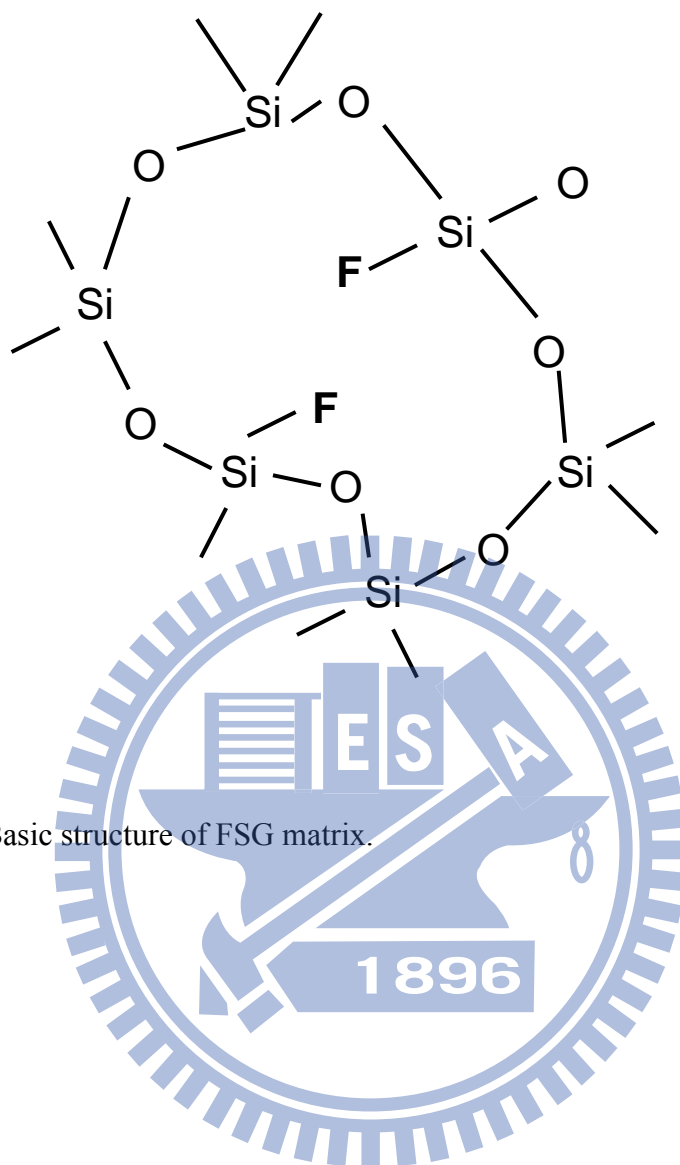


Figure 2.6 Basic structure of FSG matrix.

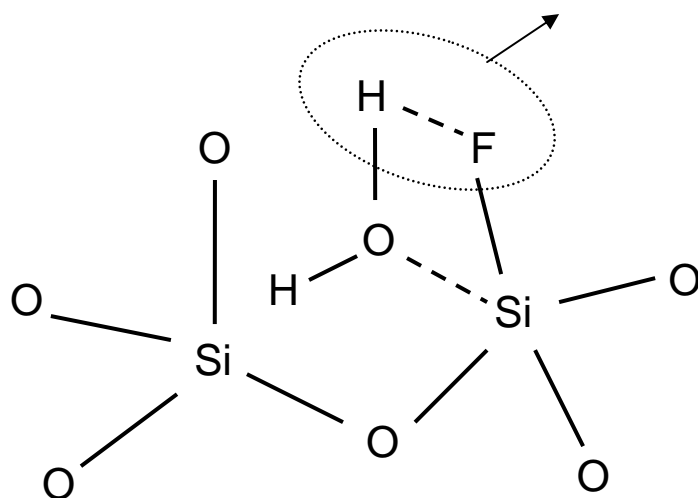


Figure 2.7 Depiction of possible bond rearrangements upon SiOF film hydration to produce Si-OH bonding and the release of HF from the film.

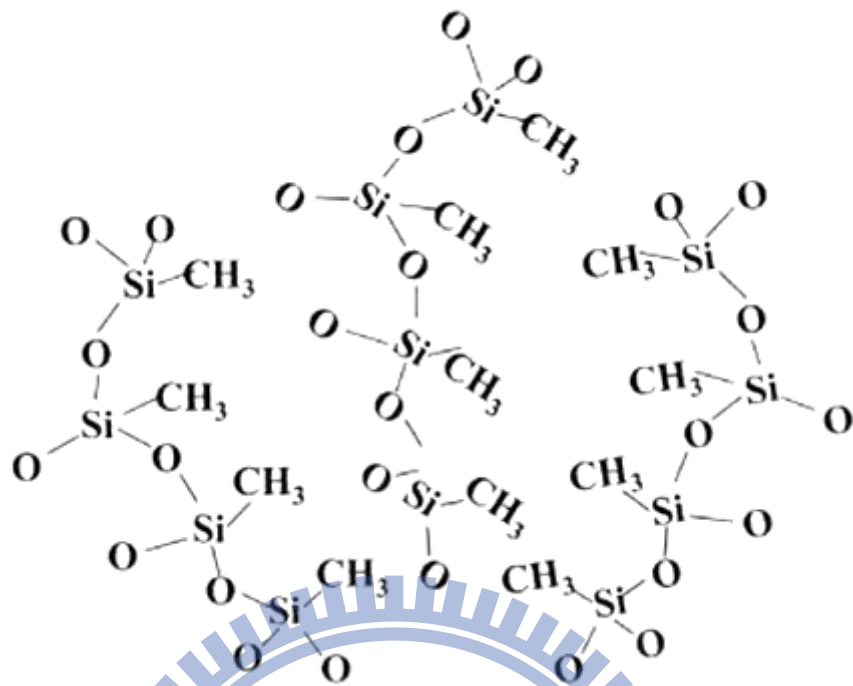
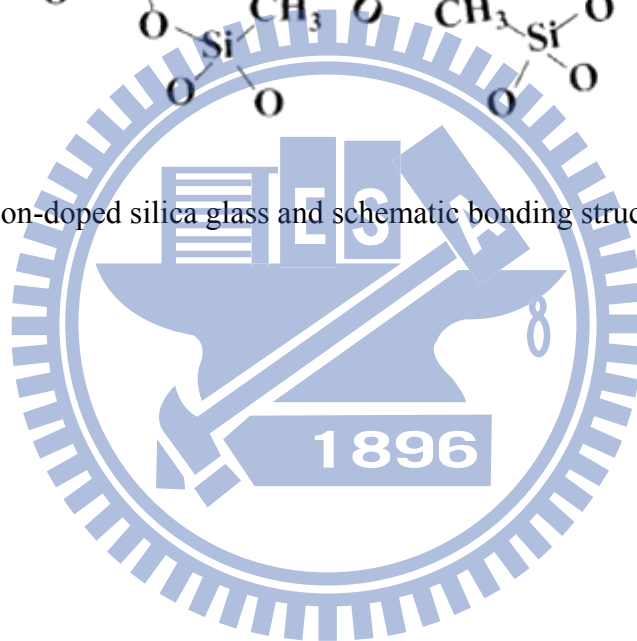


Figure 2.8 Carbon-doped silica glass and schematic bonding structure



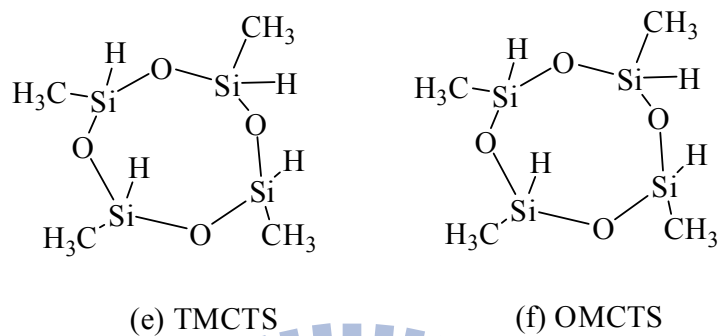
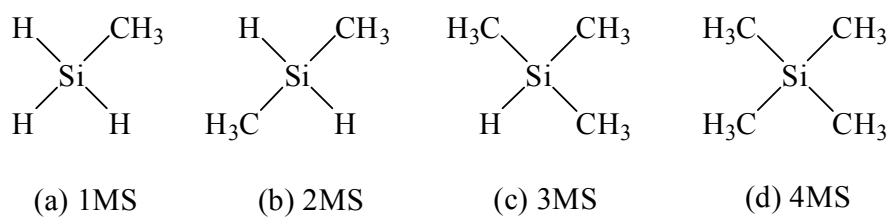


Figure 2.9 The typical precursors of CDO materials.

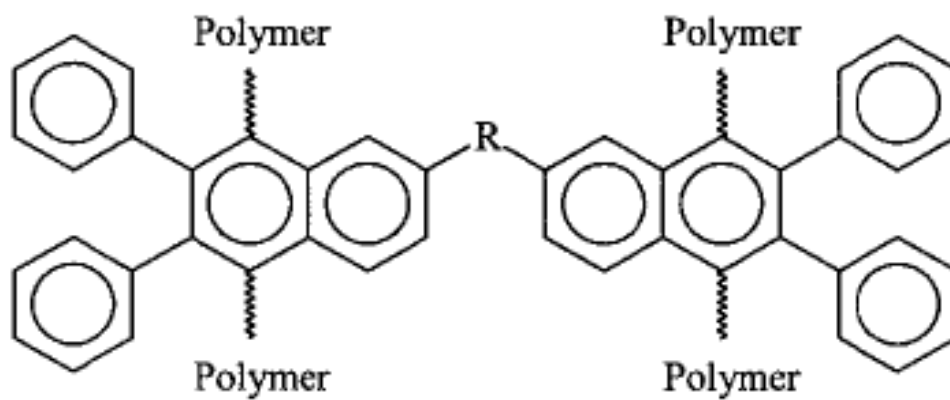


Figure 2.10 Organic SiLK™ chemical structure units.



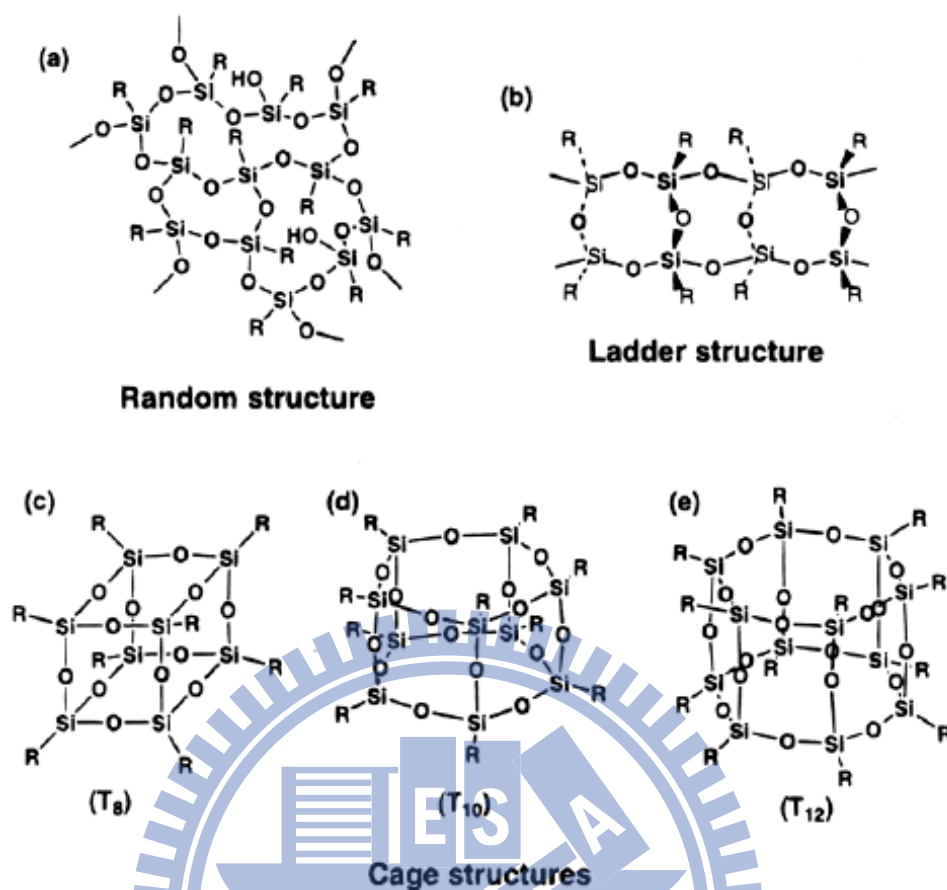


Figure 2.11 Basic structure units of SSQ dielectric materials consist of random, ladder and cage structures. R= H, CH<sub>3</sub> for HSQ and MSQ respectively.



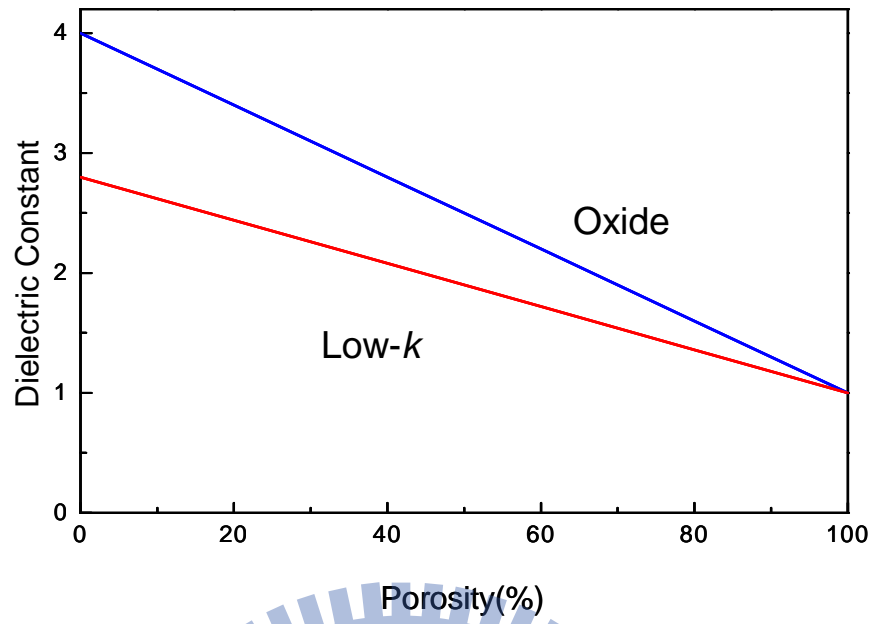
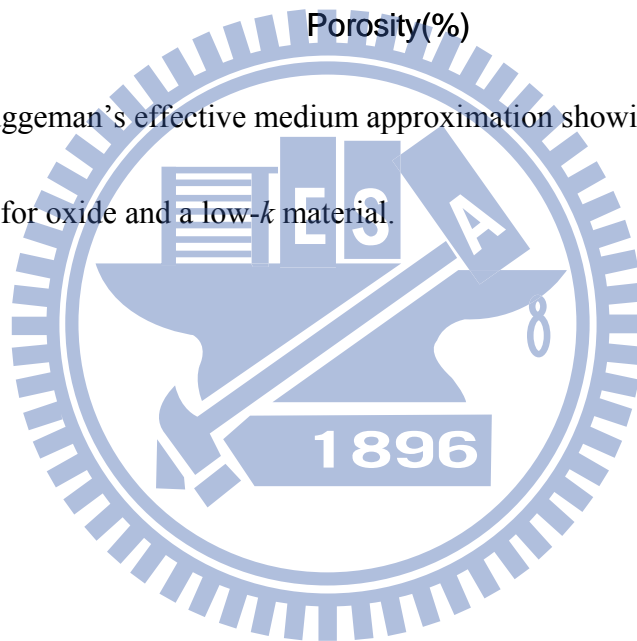


Figure 2.12 Bruggeman's effective medium approximation showing dielectric constant versus porosity for oxide and a low- $k$  material.



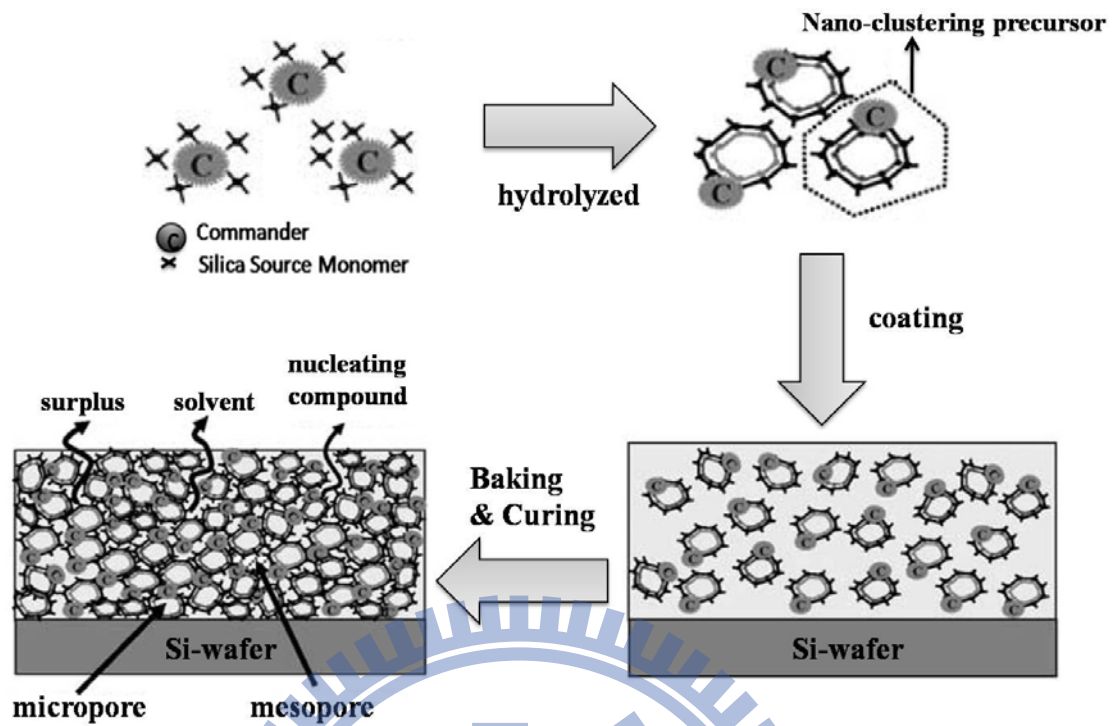


Figure 2.13 Schematics of the nano clustering silica (NSC) formulation and its film deposition and curing processes.

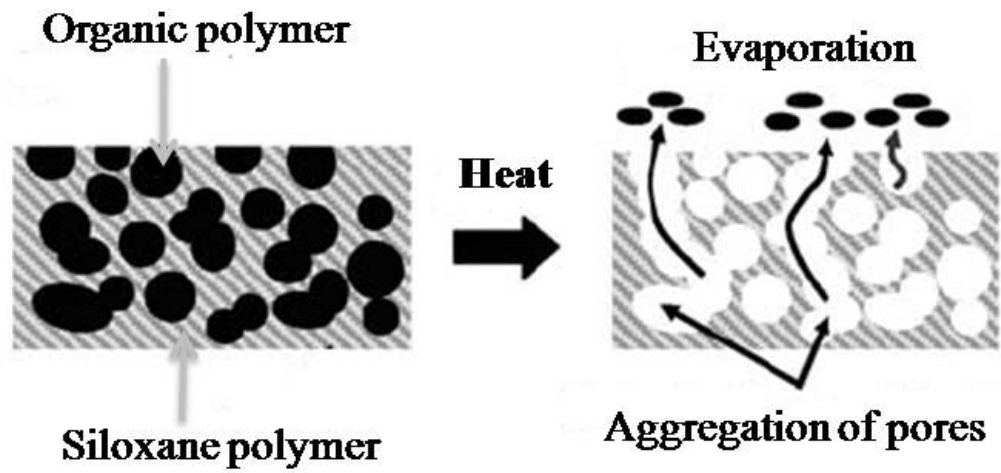
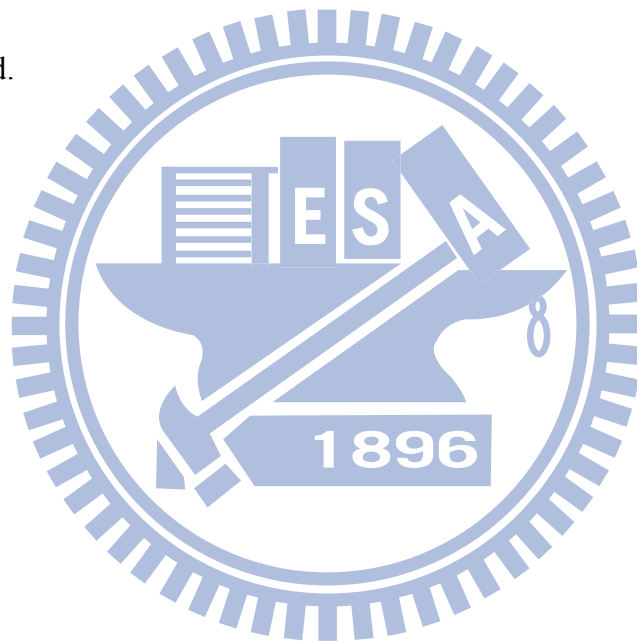


Figure 2.14 The conventional formation of porous low- $k$  by using template-type porogen method.



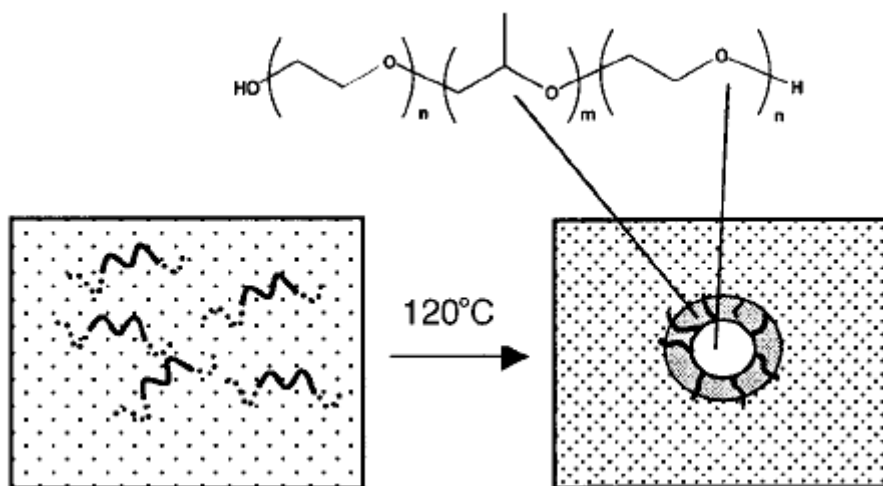


Figure 2.15 Schematic structures of phase behaviors of PEO-b-PPO-b-PEO triblock copolymers in MSQ matrixes.



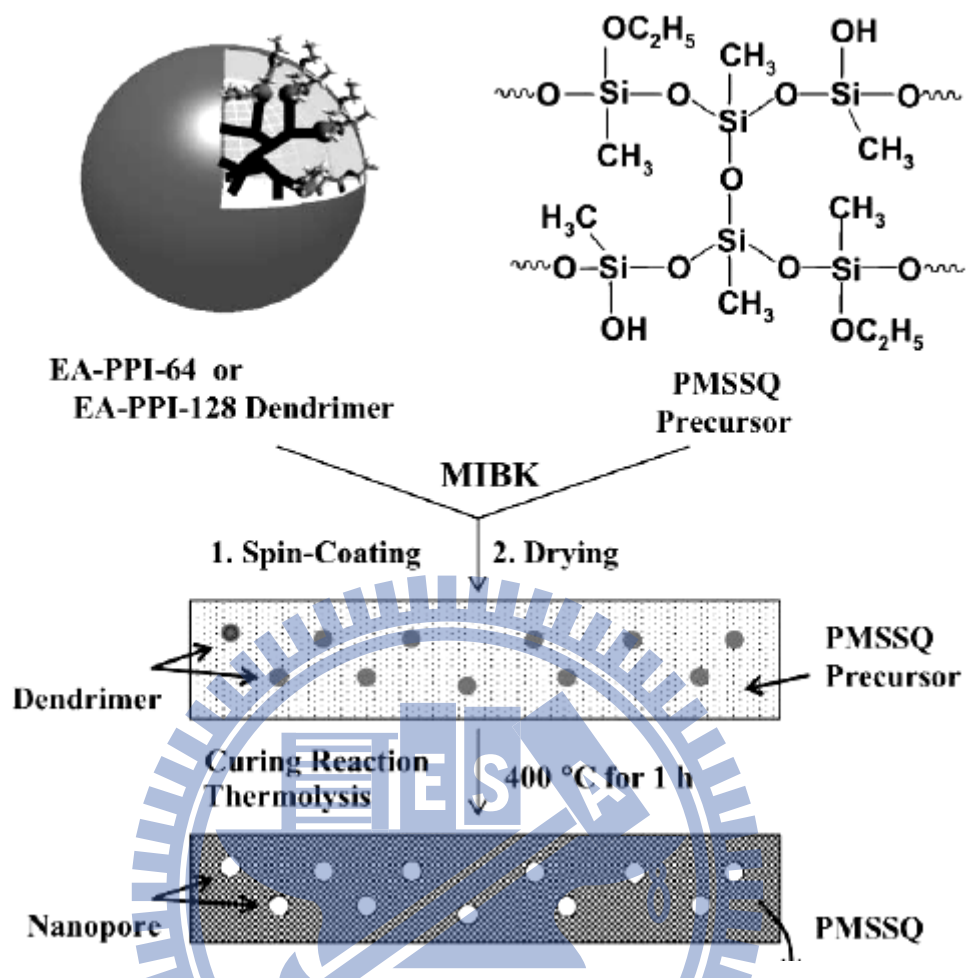


Fig. 2.16 Procedure for preparation of a nanoporous organosilicate dielectric thin film from a curable polymethylsilsesquioxane precursor matrix and a thermally labile globular dendrimer porogen (EA-PPI-64 or EA-PPI-128).

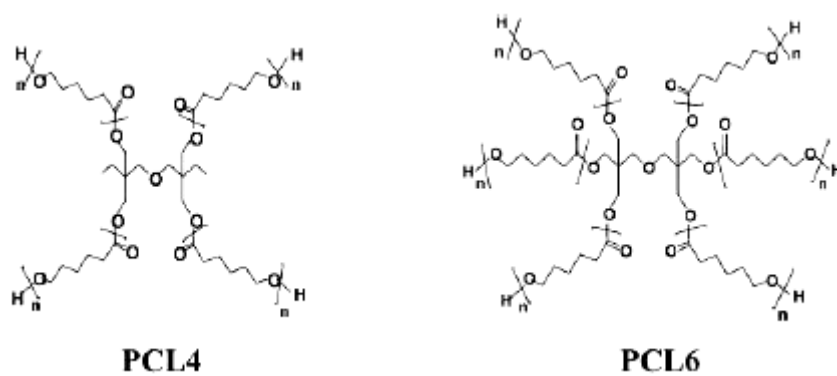
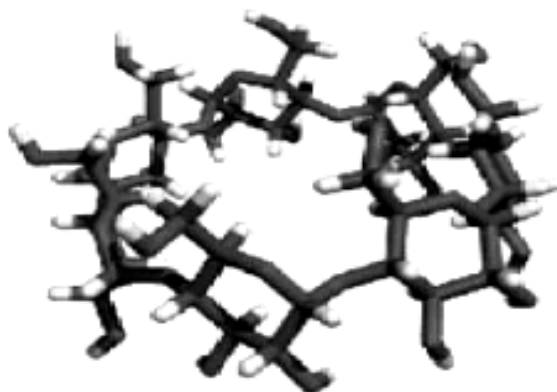


Fig. 2.17 Star-shape polymer porogens: PCL4, four-armed poly( $\epsilon$ -caprolactone) and PCL6, six-armed poly( $\epsilon$ -caprolactone).





**$\beta$ -CD**

Figure 2.18  $\beta$ -Cyclodextrin ( $\beta$ -CD), a cage supramolecular porogen



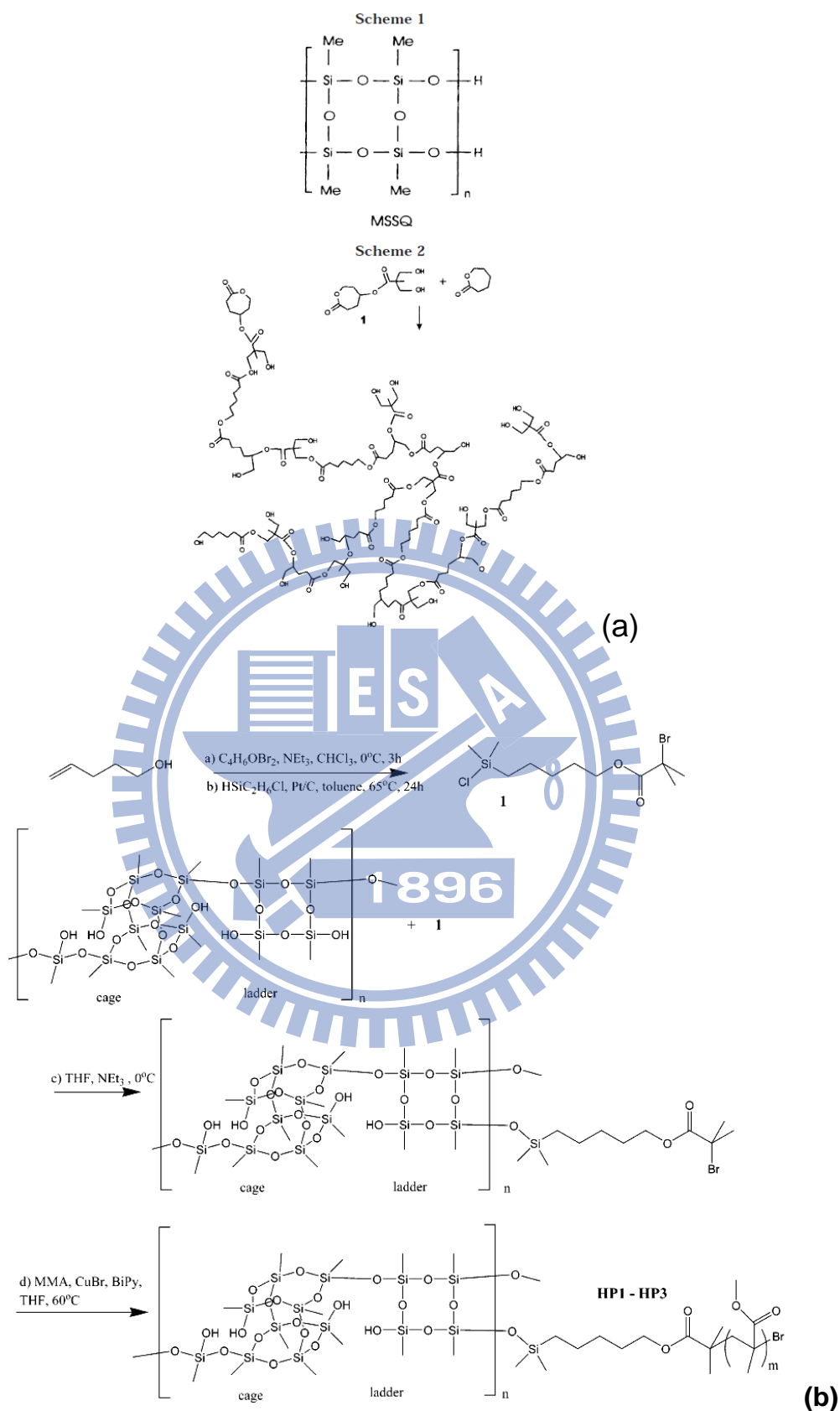


Figure 2.19 The synthetic scheme: (a) sol-gel reaction and (b) ATRP method to prepare hybrid block copolymers based on MSQ.



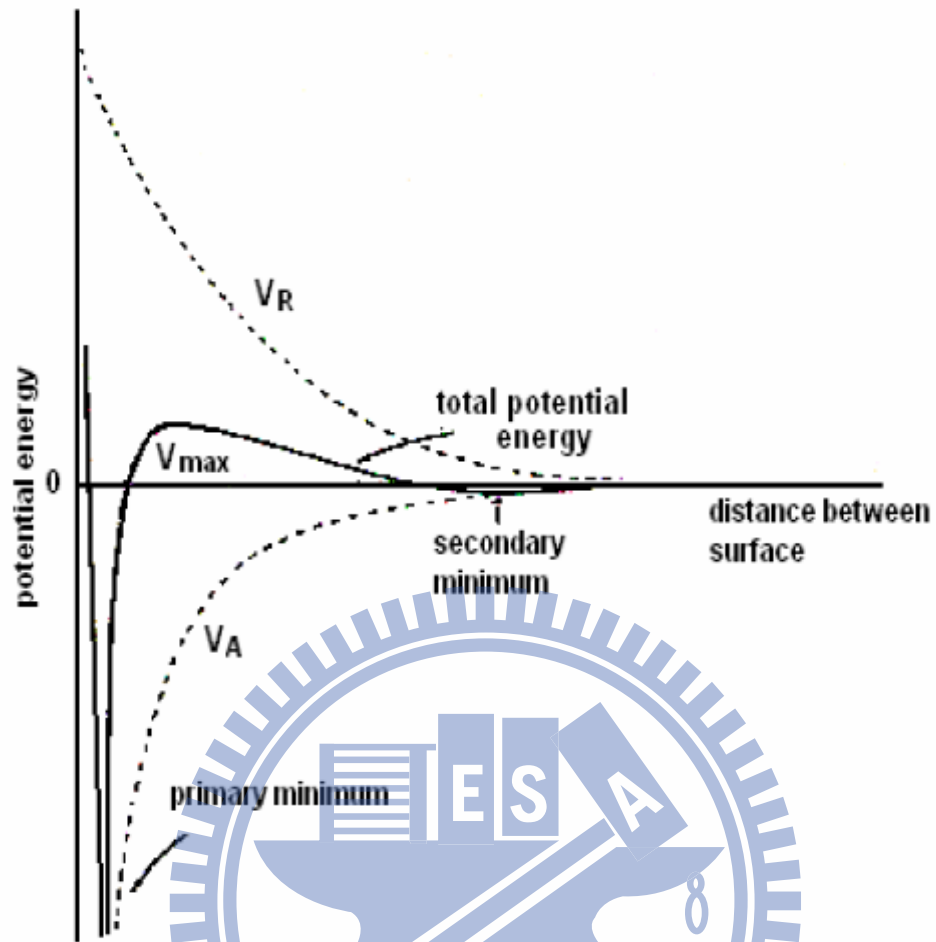


Figure 2.20 The energy and the distance of relationship for two particles.

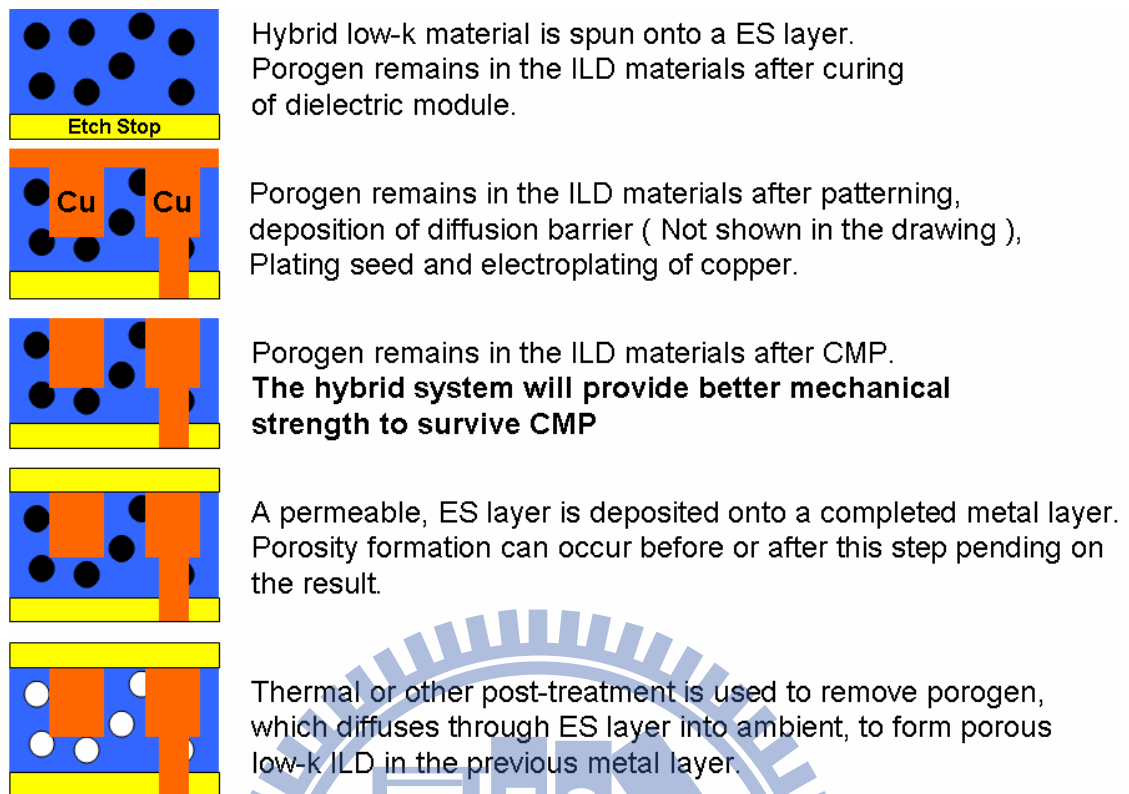


Figure 2.21 The integration scheme of the post-integration porogen removal scheme.

# Chapter 3

## Experimental

This chapter describes the preparation of MSQ/porogen solution, hybrid and porous low- $k$  materials including the materials candidates, deposition processes, and thermal treatment. The approaches used to characterize the meso-/nano- porous dielectric films are also introduced in this chapter.

### 3.1 Materials candidates

#### 3.1.1 MSQ/porogen hybrid materials

The low- $k$  matrix, poly(methylsilsesquioxane) (MSQ), was obtained from Gelest Inc. (Morrisville, PA; CAS No.68554-70-1) as clear white flakes. The molecular-weight distribution of MSQ is from 6000 to 9000 g/mole, and its dielectric constant is about 2.9. High-temperature porogens, PS-*b*-PB-*b*-PS (SBS Mw ~ 90,000 g/mole; 28 wt% PS) and PS (Mw ~ 790 g/mole) were both obtained from Sigma-Aldrich Co. The chemical structures of MSQ, and porogen are illustrated in Figure 3.1 (a) through (c), respectively.

### 3.1.2 Porogen surface modification

For porogen surface modification, we choose two kind of ionic surfactant to modify the porogen. Dodecylbenzensulfonic acid sodium salt ( $C_{12}H_{25}C_6H_4SO_3Na$ , NaDBS,  $M_w=348.48$  g/mole), an anionic surfactant, was procured from Showa Chemical Industry Co., Ltd. On the other hand, a cationic surfactant Domiphen Bromide  $CH_3(CH_2)_{11}N(CH_3)_2(CH_2CH_2OC_6H_5)Br$ , DB,  $M_w=414.48$  g/mole), was obtained from Sigma-Aldrich Co. The chemical structures of ionic surfactant are illustrated in Figure 3.2.

## 3.2 Sample preparation

The study divided into three steps, including (1) the porogen activity in the thermal profile (different curing rate,  $2^\circ C/min$  vs.  $200^\circ C/min$ ), (2) the activity of the modified and unmodified porogen under  $2^\circ C/min$  slow curing, and (3) the properties of porous film at high porosity without and with modification.

### 3.2.1 The *in-situ* porogen activity test

To form hybrid low- $k$  films, MSQ and SBS at 5 wt% loading were dissolved in tetrahydrofuran (THF) to form a hybrid low- $k$  solution without special treatment such as surfactants to further minimize the porogen size. The solution was initially filtered

through a 0.20  $\mu\text{m}$  PTFE filter (Millipore Inc.), and then spun onto (100) silicon wafer at 2000 rpm for 30 s at room temperature to obtain a film thickness of 500 nm.

The size of porogen in the hybrid low- $k$  films were then characterized by *in-situ* grazing incidence small angle X-ray scattering (GISAXS) under two curing profiles: (1) slow curing at 2°C/min and (2) rapid curing at approximately 200°C/min. *In-situ* 2D GISAXS data were collected from 30°C to 210°C in intervals of 20°C, in which data collection time are 5 sec and 2 sec for slow and rapid curing profile, using beamline 23A of the National Synchrotron Radiation Research Center (NSRRC), Hsinchu, Taiwan. All of the GISAXS data were obtained using an area detector that covered a  $q$  range from 0.01 to 0.1  $\text{\AA}^{-1}$ , and the incident angle of the X-ray beam (0.5 mm diameter) was fixed at 0.2° with an X-ray energy of 10 KeV. Then, the pore size was analyzed by sphere model fitting and Guinier's law [118,119].

The interaction between MSQ and SBS was examined by an *in-situ* viscosity measurement using ARES (Rheometric Scientific). The viscosity data were collected from room temperature to 200°C (1) at a slow curing rate (2°C/min), and (2) isothermally at 200°C. The structural change and the degree of cross-linking of MSQ in the MSQ/porogen hybrid films were investigated as a function of temperature ranging from 25 to 200°C by Fourier-transform infrared spectroscopy (FT-IR) using a MAGNA-IR 460 (Nicolet Inc.) in a transmission mode with 64 scans at a spectral

resolution of  $2\text{ cm}^{-1}$ .

The elastic modulus ( $E$ ) of hybrid film was measured using a nanoindenter (MTS, Nano Indenter XP system) with a Berkovich tip. The samples were cured up to  $200^{\circ}\text{C}$  following two different curing profiles to form hybrid low- $k$  films. In the slow curing method, the sample was cured in a quartz tube furnace under  $\text{N}_2$  at a curing rate of  $2^{\circ}\text{C}/\text{min}$  to  $200^{\circ}\text{C}$  for 30 min. In the rapid curing method, the samples were cured for 30 min directly on the hot plate preheated at  $200^{\circ}\text{C}$ . The nominal film thickness of hybrid films for nanoindentation is 1200 nm, while the indentation depth is kept at 100 nm.

### 3.2.2 Porogen modification

PS particles were first dissolved in tetrahydrofuran (THF) to form a solution without modification ( $\text{pH} \sim 7.0$ ). In addition, pH value and surfactants were used to modify the surface property of the PS particles. For pH effect, PS solutions with pH values of 3 and 11 were prepared by adding acid and base, respectively. Moreover, the well-dispersed PS/THF solutions were modified by two types of surfactants: (1) anionic surfactant, NaDBS, below its critical micelle concentration (CMC) of 522.75 mg/L, and (2) cationic surfactant, DB below its CMC of 730.74 mg/L [120]. The zeta potentials of the PS/THF solutions with and without modification were measured using a Zeta Potential Analyzer (Zetasizer HSA3000, Malvern Instruments). The size of the PS

particles in the THF solution was measured using an Ultrafine Particle Analyzer (Honeywell UPA 150).

Then, MSQ and PS particles (with and without surface modification) at 10 wt% loading were dissolved in THF solvent to form a hybrid low- $k$  solution. The solution was initially filtered through a 0.20  $\mu\text{m}$  PTFE filter (Millipore Inc.), and then spun onto a (100) silicon wafer at 2000 rpm for 30 s at room temperature to obtain a film thickness of 500 nm. The size and distribution of the porogen in the hybrid low- $k$  films during the curing step at 2°C/min were then characterized by *in situ* GISAXS. *In situ* 2D GISAXS data were collected from 30 to 200°C at intervals of 10°C. All of the GISAXS data were obtained using an area detector covering a  $q$  range from 0.01 to 0.1  $\text{\AA}^{-1}$ , and the incident angle of the X-ray beam (0.5 mm diameter) was fixed at 0.2° with an x-ray energy of 10 keV. Then, the porogen size was analyzed using sphere-model fitting and Guinier's law [118,119].

The interaction between MSQ and PS was then examined by an *in situ* viscosity measurement using ARES (Rheometric Scientific). The viscosity data were collected from room temperature to 200°C for the MSQ/PS hybrid films with and without modification by surfactants. The interaction between MSQ and surfactant-modified PS was further investigated using a FTIR spectrometer, MAGNA-IR 460 (Nicolet Inc.) in a transmission mode with 64 scans at a spectral resolution of 2  $\text{cm}^{-1}$ .

Finally, the hybrid films (with and without modification) were cured in a quartz tube furnace under N<sub>2</sub> at a heating rate of 2°C/min to 400°C for 1 hr to form the porous low-*k* films after completely burning out the porogens. Their pore sizes were also characterized using the GISAXS technique. The porosity of the porous low-*k* films were obtained from its density, which was measured by X-ray reflectivity (XRR) (Bruker D8 Discover), with a Cu K<sub>α</sub> source ( $\lambda=0.154$  nm), using  $\omega$ -2 $\theta$  scan mode. The scanning region ranged from 0 to 2°. The XRR data was analyzed by LEPTOS simulation software, to fit the density of porous low-*k* film.

### **3.2.3 Different porosity low-*k* film with and without modification**

First, PS particles were dissolved in THF to form a well-dispersed solution using different treatments: (1) without modification, (2) pH modification at a value ranging from 3 to 11, and (3) with a cationic surfactant, DB below its critical micelle concentration 730.74mg/L. The zeta potentials of PS/THF solutions with and without modification were measured using a Zeta Potential Analyzer (Zetasizer HSA3000, Malvern Instruments). The size of the PS particles in THF solution was measured using an Ultrafine Particle Analyzer (Honeywell UPA 150).

Then, MSQ and PS (with and without surface modifications) of 10, 20, 30, 40,



and 50 wt % loading were dissolved in THF solvent to form a hybrid low- $k$  solution. The solution was initially filtered through a 0.20  $\mu\text{m}$  PTFE filter (Millipore Inc.), and then spun onto a (100) silicon wafer at 2000 rpm for 30 s at room temperature to obtain a film thickness of 500 nm. The sample was cured in a quartz tube furnace under  $\text{N}_2$  at a curing rate of  $2^\circ\text{C}/\text{min}$  to  $400^\circ\text{C}$  for 60 min to remove the porogen.

### 3.2.3.1 Porosity

All of the film density in the porous low- $k$  films was measured by X-ray reflectivity (XRR). The porosity of the porous low- $k$  films were obtained from its density, which was measured by X-ray reflectivity (XRR) (Bruker D8 Discover), with a  $\text{Cu K}_\alpha$  source ( $\lambda=0.154$  nm), using  $\omega$ -2 $\theta$  method with scan angle from  $0^\circ$  to  $2^\circ$ . The XRR data were analyzed by LEPTOS simulation software using a genetic algorithm model [121]. Film thickness were also confirmed by using an n&k Analyzer 1280 (n&k Technology, Inc.) at wavelengths ranging from 190 to 900 nm.

### 3.2.3.2 Pore size and porogen size

The pore size in the porous low- $k$  films were then characterized by 2D GISAXS. The pore morphology of porous MSQ films was examined by FIB-SEM (Nova Nanolab 2000 system, FEI Company). The pore morphology of porous low- $k$  films was

examined by a focus ion beam/ scanning electron microscope (FIB/SEM) dual-beam system (FEI Nova 200) after sputtering etch  $\sim 40$  nm off the surface of the low- $k$  films. Moreover, the pore size and porogen size were further obtained by GISAXS. GISAXS was a versatile tool for characterizing nanoscale density correlations and/or the shape of nanoscopic objects at surfaces, at buried interfaces, or in thin films. The incidence beam extracted from a super-conducting wavelength-shifter X-ray source, was monochromated to a wavelength ( $\lambda$ ) of 1.55 Å by a Ge (111) double crystal monochromator, with  $\Delta\lambda/\lambda \sim 10^{-3}$  resolution. The two dimensional image were recorded by a low-noise 16-bit charge-coupled device (CCD) camera. All GISAXS data were corrected for sample transmission, background, and the detector sensitivity. Then the pore size was analyzed by Guinier's law. A typical geometry of GISAXS measurement was depicted in Figure 3.3. The area detector records the scattering intensity of scattered rays over a range of exit angles ( $\beta$ ) and scattering angles ( $\psi$ ) in the surface plane [122]

### 3.2.3.3 Electrical characteristics

The  $k$  was characterized by capacitance-voltage (C-V HP 4280) measurement, using metal insulator semiconductor (MIS) structure configuration [Al electrode/MSQ film/Si (50 ohm-cm)] at room temperature. To accurately measure the dielectric constant by C-V dot measurement, three circular aluminum dots of nominal diameters

200, 400, and 800 mm were used to minimize the geometric effect. Aluminum electrodes with a thickness of 1  $\mu\text{m}$  were coated onto the dielectric films by ULVAC EBX-6D thermal evaporator through a shadow mask. Prior to CV-dot measurement, the samples were kept in a small vacuum chamber which was pumped to  $10^{-2}$  torr. The dielectric constant ( $k$ ) of the films was determined by the following Equation (3.1)

$$k = \frac{C}{A} \times \frac{d}{\epsilon_0} \quad (3.1)$$

where  $C$  is the capacitance of the MIS structure,  $d$  is the film thickness,  $A$  is the area of the aluminum dot,  $\epsilon_0$  is the permittivity of free space ( $8.854 \times 10^{-12}$  F/m)

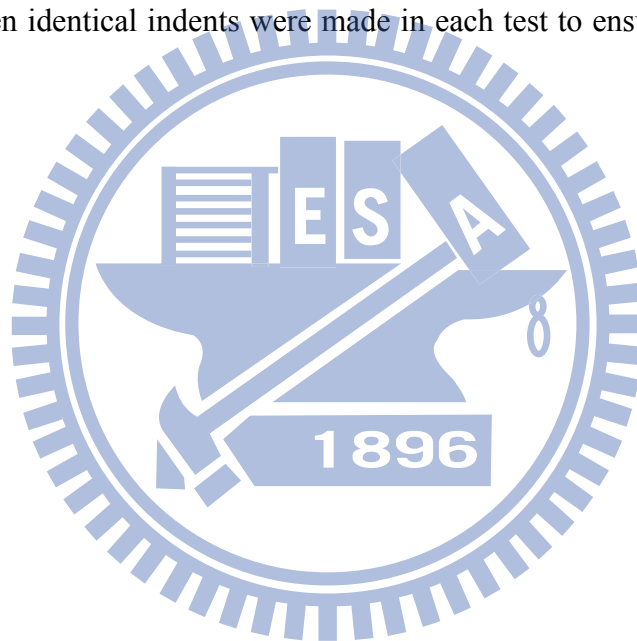
#### 3.2.3.4 Chemical characteristics

The structural transformation and MSQ's ratio of network/cage in the matrix were studied using Fourier-transform infrared spectroscopy (FT-IR). The measurements were performed using a MAGNA-IR 460 (Nicolet Inc., Waltham, MA) in specular mode with  $30^\circ$  incident angle, and 64 scans at  $2 \text{ cm}^{-1}$

#### 3.2.3.5 Mechanical strength

The elastic modulus of the low- $k$  films were measured using a Nanoindenter (MTS,

Nano Indenter XP system) with a diamond tip with Berkovich geometry. A holding segment was inserted in the end of each loaded segment to allow time for the system to equilibrate before it was unloaded. Then, unloading was performed at a constant rate. The early unloaded portion was used to calculate the stiffness, and the holding segment was used to correct the thermal drift. The indentation depth was 100 nm, but the elastic modulus was determined from the first 10% of the film thickness to avoid the substrate effect. About ten identical indents were made in each test to ensure reproducibility and accuracy.



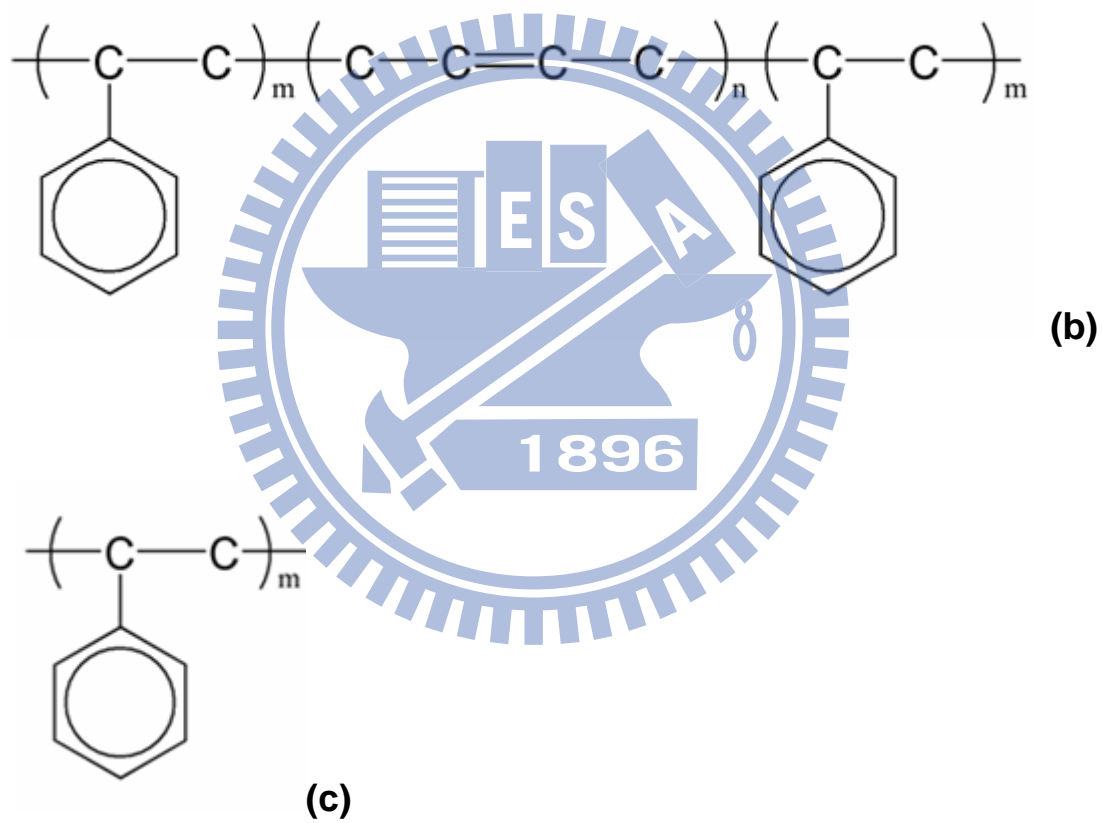
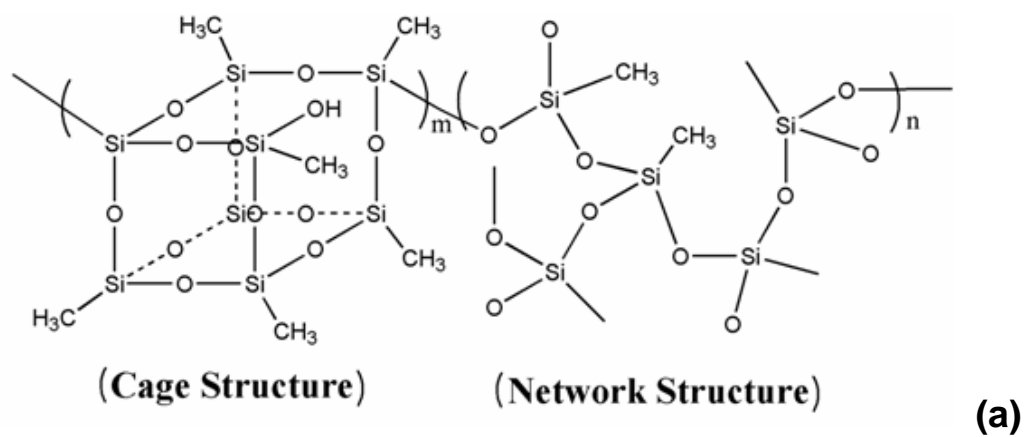


Figure 3.1 The molecular structure of (a) MSQ as the low- $k$  matrix; (b) PS-b-PB-b-PS and (c) PS as the high-temperature porogens.

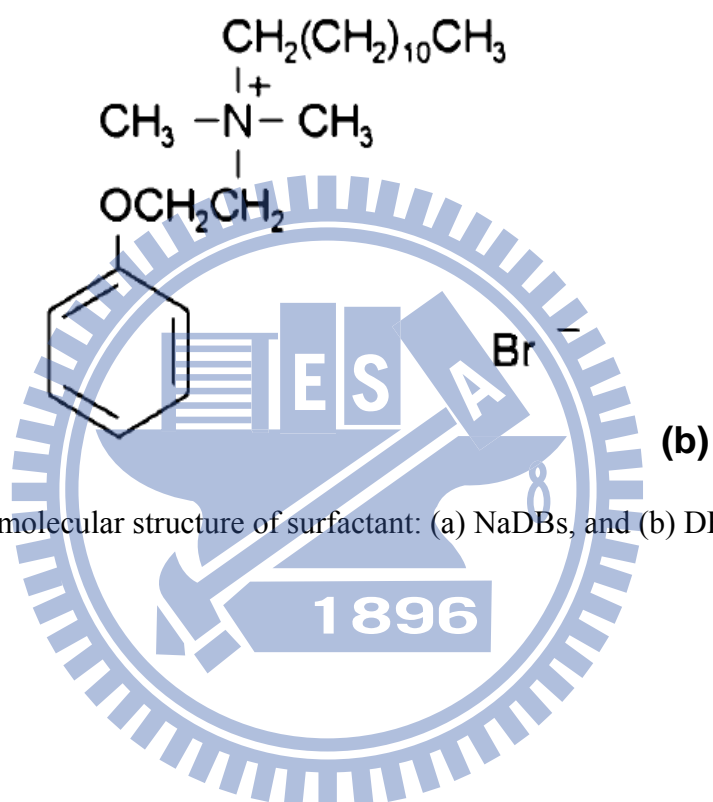
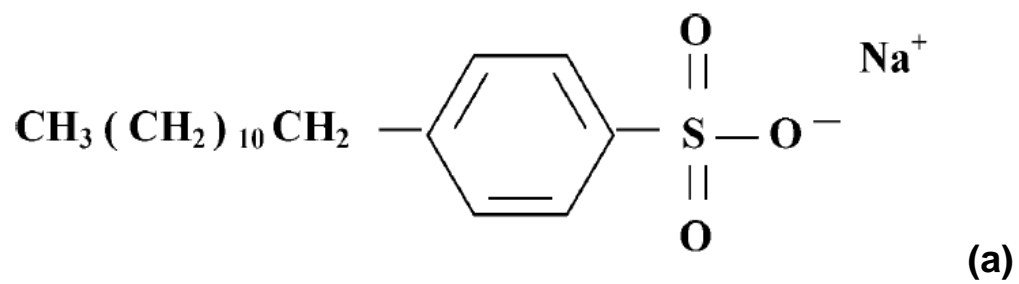


Figure 3.2 The molecular structure of surfactant: (a) NaDBs, and (b) DB.

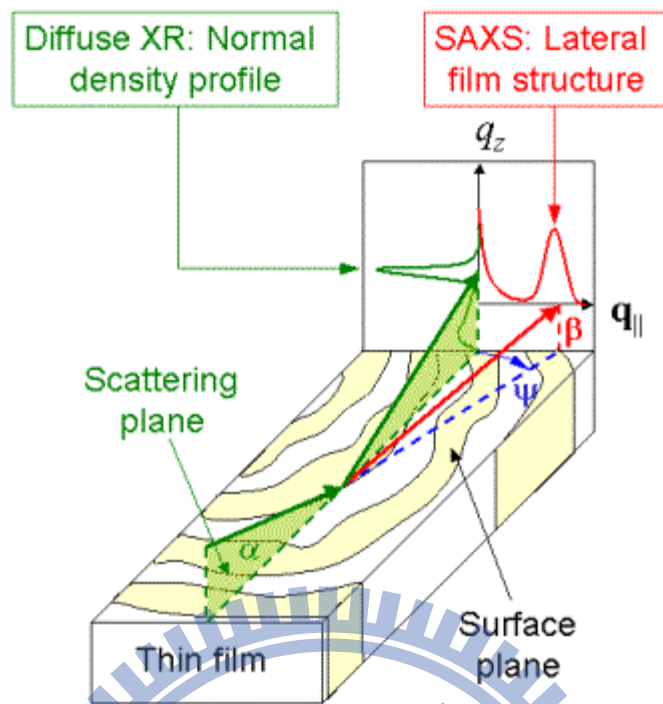


Figure 3.3 Typical geometry of GISAXS measurement.

# Chapter 4

## Effect of Curing on the Porogen Size in the Low- $k$ MSQ/SBS Hybrid Films

In this chapter, the interaction between porogen and low- $k$  matrix during curing and their impact on the porogen size of low- $k$ /porogen hybrid films will be discussed. A commercial, spin-on organosilicate, MSQ was selected as the matrix and a high-temperature porogen such as SBS, was employed as the sacrificial component. The effects of curing rate (slow: 2 °C/min vs. rapid: 200 °C/min) and cure temperature on the porogen size in the hybrid low- $k$  films cured up to 200 °C were studied by *in-situ* GISAXS, viscosity measurement, and FT-IR analysis. The impact of the MSQ structure during thermal cure process on the porogen aggregation behavior and its correlation with porogen size will be described and elucidated.

### 4.1 *In-situ* porogen size test

The porogen size of the hybrid low- $k$  films before burning out were first characterized by *in-situ* GISAXS. Figures 4.1(a) and (b) show the 2D GISAXS scattering patterns of the hybrid low- $k$  films for various curing temperatures (50-210°C) at two different curing rates. In Figure 4.1(a), the scattering patterns of the hybrid low- $k$



film cured at slow curing rate showed significant transition between 90 and 170°C. In contrast, the scattering patterns of low- $k$  films cured at a rapid curing rate exhibited little variation as illustrated in Figure 4.1(b). These scattering patterns indicate that the SBS porogens showed much diffusion and aggregation activities within MSQ matrix when the hybrid film was cured at a slow curing rate. In contrast, the diffusion and aggregation of SBS within MSQ matrix is very limited when the hybrid low- $k$  film was cured at a rapid rate.

From GISAXS scattering patterns, the porogen sizes in the MSQ/SBS films cured under different rates at temperatures between 50 and 210°C can be further determined. In this paper, a particulate system was used to analyze the scattering data by treating the pores in the matrix the same as the particles in the hybrid film. When the particle concentration is low, the scattering of the pores in the matrix does not mutually interact. Accordingly, the scattering intensity of individual particle,  $I(q)$ , could be defined by Equation (4.1),

$$I(q) = n_p (\rho_p - \rho_m)^2 V_p^2 P(q) S(q) \quad (4.1)$$

where the wavevector  $q = 4\pi\lambda^{-1}\sin\theta$  is defined by the wavelength  $\lambda$  and the scattering angle  $2\theta$  of X-rays;  $n_p$  is the number density of particles;  $\rho_p$  and  $\rho_m$  are the scattering density of the particle and the matrix;  $V_p$  denotes the volume of particle;  $P(q)$  is a form factor, and  $S(q)$  is a structure factor. The structure factor  $S(q)$  is close to 1 in a

low-concentration system and thus can be ignored. Therefore, the scattering profile of  $I(q)$  is only related to the form factor  $P(q)$  of the particles. As a result,  $I(q)$  can be furthered to the Guinier's expression [123,124,125], involving radius of gyration  $R_g$  as described by Equation (4.2).

$$I(q) = n_p (\rho_p - \rho_m)^2 V_p^2 \exp\left(\frac{-q^2 R_g^2}{3}\right) \quad (4.2)$$

In this case, a linear relationship exists between  $\ln(I)$  and  $q^2$ , with a slope of  $(-R_g^2/3)$ . Figures 3(a) and 3(b) show  $\ln(I)$  plot against  $q^2$  in the 2D GISAXS scattering patterns of the hybrid low- $k$  films cured at various temperatures under slow curing and rapid curing conditions, respectively. The slope, i.e.  $R_g$  size, showed that the porogen  $R_g$  size increased non-linearly with the curing temperature between 50 and 210°C in the slowly cured system as shown in Figure 4.2(a), but varied little with temperature between 50 and 210°C in the rapidly cured system as shown in Figure 4.2(b). Since the shape of SBS porogen in the hybrid film is close to sphere as confirmed by scanning electron microscope, the pore size,  $d$  could be deduced from  $d = 2(5/3)^{1/2} R_g$  [126,127]. In addition, the porogen size distribution is estimated from the change of the slopes in the low- $q$  region; for instance, monodispersity corresponds to a single slope. As a result, the calculated porogen size and distribution of the hybrid low- $k$  films as a function of curing temperatures under the slow curing and rapid curing conditions are shown in Figure 4. Upon slow curing to 210°C as shown in Figure 4.3(a), the porogen

size/distribution increased from  $12.7 \pm 2.3$  nm to  $32.8 \pm 5.4$  nm. Moreover, the increase rate of pore size became noticeable at  $T > 110^\circ\text{C}$ , and more significant between  $130^\circ\text{C}$  and  $170^\circ\text{C}$  (from  $17.5 \pm 2.9$  nm to  $31.2 \pm 4.9$  nm), but little variation between  $170^\circ\text{C}$  and  $210^\circ\text{C}$  (from  $31.2 \pm 4.9$  nm to  $32.8 \pm 5.4$  nm). In contrast, the porogen size/distribution remained about  $12 \pm 2$  nm with a narrow size distribution upon rapid curing up to  $210^\circ\text{C}$  as shown in Figure 4.3(b).

## 4.2 *In-situ* viscosity test

Subsequently, the interaction between SBS porogen and MSQ matrix was examined by an *in-situ* viscosity measurement from room temperature to  $200^\circ\text{C}$  (1) at a slow curing rate ( $2^\circ\text{C}/\text{min}$ ), and (2) at a rapid curing rate, *i.e.* isothermally at  $200^\circ\text{C}$  as shown in Figures 4.4(a) and (b), respectively. For the slowly cured system shown in Figure 4.4 (a), the viscosity increased linearly up to about 3800 s or  $100^\circ\text{C}$  when it reached the first plateau. In this period, the viscosity was strongly influenced by the solvent, *i.e.* THF whose boiling point is  $66^\circ\text{C}$ . At this time, the molecular chains of MSQ and porogen hardly diffused and aggregated because the hybrid films behaved like a solid as the solvent, THF was slowly evaporated, leading to film shrinkage and increase of viscosity [128].

Beyond  $100^\circ\text{C}$ , the viscosity initially remained around 210,000-230,000 poise in

the plateau, then dropped drastically to 130,000 poise above 160°C until to 170°C, subsequently increased again up to ~ 250,000 poise at 200°C. In the plateau stage (100 to 160°C), the glass transition temperature ( $T_g$ ) of the hybrid film played an important role on the viscosity. For the low- $k$  matrix MSQ, it has a  $T_g$  around 88-111°C depending on the ratio of hydroxyl and methoxy groups within the precursor [129]. In contrast, the porogen, SBS has a  $T_g$  around 98-105°C depending on the weight percentage of polystyrene and polybutadiene [130]. Based on differential scanning calorimetry (DSC) measurement, the  $T_g$ 's of SBS and MSQ in this study were 90 and 100°C, respectively. As the temperature exceeded 100°C, *i.e.*  $T_g$  of MSQ, the molecular chains of MSQ matrix became relaxed or “rubber-like”, which further enhanced the mobility of the SBS particles, resulting in slight reduction of viscosity to ~210,000 poise. It is believed that SBS particles aggregated readily as facilitated by the rubber-like MSQ matrix at  $T \geq T_g$ .

As the temperature was increased to about 160°C, drastic drop of viscosity in the MSQ/SBS hybrid film was presumably caused by the plasticization of H<sub>2</sub>O released at the onset of significant MSQ cross-linking reaction, which will be further elucidated by FT-IR analysis in the following section. After 170°C, the viscosity resumed its increasing trend up to 200°C as H<sub>2</sub>O was evaporated rapidly while the crosslinking of low- $k$  MSQ matrix continued. As a result, significant aggregation of SBS porogen occurred during 160-170°C stage due to its high mobility in a much reduced viscosity

condition. This explained the rapid increase of porogen size and distribution at temperature between 150 and 170°C, then the porogen size leveled off due to limited mobility of SBS porogen as the viscosity increased beyond 170°C. On the other hand, Figure 4.4(b) shows the *in-situ* viscosity of the hybrid film cured rapidly at 200°C. In this system, the viscosity rapidly reached a plateau of ~250,000 poise at 400 s. This suggested that low-*k* MSQ matrix became very dense and rigid in a short period, inducing enormous viscosity in the film and preventing any aggregation of porogen. Thus, the size of porogen was confined to ~12 nm with tight distribution immediately upon fast cure.

### 4.3 Structure variation and porogen aggregation

It becomes clear that the structure state of low-*k* MSQ matrix at  $T \geq T_g$  during the cure step plays a critical role on the viscosity of the hybrid film and porogen size. As a result, FT-IR was employed to examine the structure state of MSQ matrix in the MSQ/porogen hybrid films as a function of cure temperature. Figure 4.5(a) shows FT-IR spectra of the hybrid films cured up to various temperatures such as 25, 100, 150 and 200°C. Two peaks at 1130 and 1030  $\text{cm}^{-1}$  were attributed to Si–O stretching in the cage and network structures, respectively. In addition, all infrared spectra were normalized to the intensity of cage Si–O stretching at 1130  $\text{cm}^{-1}$  and the ratio of specific

absorption band to the cage Si–O absorption band was defined by its peak intensity to that of cage Si–O band in this study for simplicity. The absorption intensity at  $1030\text{ cm}^{-1}$  associated with the stretching of network Si–O changed slightly between 25 and  $100^\circ\text{C}$  based on the band broadening even though peak height remained the same, but its intensity increased significantly when curing temperature was raised above  $100^\circ\text{C}$ . To carefully examine the change rate of structural transformation from cage Si–O to network Si–O structure, the ratio of network/cage structure in the MSQ/SBS hybrid films is shown in Figure 4.5(b) for slow cure profile from 30 to  $200^\circ\text{C}$  at an interval of  $10^\circ\text{C}$ . The ratio increased gradually from 0.932 to 0.938 when cure temperature was raised from 30 to  $100^\circ\text{C}$ . Afterwards, the ratio rose up from 0.938 at  $100^\circ\text{C}$  to 0.952 at  $160^\circ\text{C}$ , due to the condensation of silanol (Si–OH) groups in MSQ precursor [131]. Yet, at T between 160 and  $170^\circ\text{C}$ , there was a faster increase in the ratio of network/cage structure (from 0.952 to 0.962) as evidenced by the change of slope shown in Figure 4.5(b). This indicated that MSQ underwent extensive structural transformation from cage Si–O to network Si–O structure through the cleaving of Si–O–Si group in the cage structure and condensation reaction, *i.e.* crosslinking with a byproduct of  $\text{H}_2\text{O}$ . For a short duration, the released  $\text{H}_2\text{O}$  can serve as a plasticizer in the MSQ/SBS hybrid film, reducing its viscosity between 160 and  $170^\circ\text{C}$  as shown in Figure 4.4(a). From 170 to  $200^\circ\text{C}$ , the ratio of network/cage structure increased at a slightly lower rate from  $\sim 0.96$

up to 0.98 as the transformation to rigid, 3D network structure continued. Continued crosslinking of MSQ matrix in conjunction with fast evaporation of H<sub>2</sub>O accounted for the increasing viscosity above 170°C in Figure 4.4(a).

Summarizing the results of *in-situ* viscosity measurement, structural variation of MSQ matrix by FT-IR analysis, and porogen size by GISAXS as a function of temperature in Figure 4.6, the effect of the MSQ structure during thermal cure process on the porogen aggregation behavior and its correlation with porogen size can be described and elucidated below.

For the as-spun MSQ/SBS hybrid films in this paper, the SBS porogen (5 wt%) could be considered as nano-particles in the MSQ matrix, whose structure could change from precursor at room temperature to lightly crosslinked or even highly crosslinked structure depending on cure temperature and cure rate. In turn, the structure of MSQ matrix during thermal cure process affected the porogen aggregation behavior and the porogen size in the MSQ/SBS hybrid films. According to the *in-situ* viscosity measurement, porogen size measurement by GISAXS, and FT-IR analysis summarized in Figure 4.6, the interaction between SBS porogen particles and the MSQ matrix for the slow cure profile could be divided into four stages; namely (1) below 100°C, (2) 100 to 160°C, (3) 160 to 170°C, and (4) above 170°C up to 200°C. This highlights three critical temperatures: (1) glass transition temperature,  $T_g$  (~100°C), (2) onset

temperature of network Si–O transformation (160°C), and (3) immobilization temperature (170°C), which controlled the microstructure of MSQ matrix and, in turn, the porogen segregation and porogen size during the thermal cure process.

For temperature below 100°C in the slow cure system, SBS porogen particles hardly diffused and aggregated within MSQ matrix because the hybrid films behaved as a solid when THF solvent was slowly evaporated, leading to film shrinkage and increase of viscosity. Little variation of SBS porogen size (~12-13 nm) was found in this stage.

In the 2<sup>nd</sup> stage (100°C to 160°C), MSQ matrix exhibited a low-degree of crosslinking via the condensation of Si–OH groups as evidenced by the ratio of network/cage structure shown in Figure 4.6, even though MSQ crosslinking started at room temperature [132]. At  $T > T_g$  of MSQ matrix, SBS possessed high mobility in the MSQ matrix, whose molecule chains fully relaxed, reducing the viscosity of the hybrid film as illustrated by Figure 7. Therefore, the behavior of SBS particle could be described by the kinetic molecular theory of Brownian motion based on Einstein-Stokes Equation (4.3) [133,134].

$$D = \frac{k_B T}{6\pi\eta r} \quad (4.3)$$

where the  $k_B$  is Boltzmann constant;  $T$  is the absolute temperature;  $\eta$  is the viscosity of system;  $r$  is the particle radius. At this stage, the SBS particle aggregation depended on its diffusivity, which increased with (1) increasing temperature due to higher collision



frequency and (2) reduced viscosity,  $\eta$ , which is a measure of the steric barrier for SBS particle to move within MSQ matrix. Thus, the relaxation of SBS and MSQ molecular chains at  $T > T_g$  led to reduced viscosity and higher diffusivity of SBS particles. Such high diffusivity enhanced SBS collision and led to the aggregation of SBS porogen from 13 nm to 22 nm.

At  $T > 160^\circ\text{C}$ , the cross-linking of MSQ precursor continued. But, we observed noticeable transformation of MSQ matrix from loose, cage Si–O structure to dense, network Si–O structure which served as a 3D steric barrier to the migration of SBS particles within the MSQ matrix. One expected the viscosity of the hybrid films to increase from 170 to  $200^\circ\text{C}$  as a higher degree of crosslinking took place and more network Si–O structure was formed. Instead, the viscosity dropped drastically to 130,000 poise in the 3<sup>rd</sup> stage (160 to  $170^\circ\text{C}$ ). It is believed that when extensive transformation of cage to network Si–O occurred at  $T > 160^\circ\text{C}$ , large amount of  $\text{H}_2\text{O}$  byproduct could serve as a plasticizer in the MSQ/SBS hybrid film and result in significant reduction of viscosity. Furthermore, this enhanced aggregation of SBS porogens resulting in a faster change of porogen size from 22 to 31 nm between 150 and  $170^\circ\text{C}$ .

In the final stage (170 to  $200^\circ\text{C}$ ), most  $\text{H}_2\text{O}$  is believed to be dried up prior to  $170^\circ\text{C}$ . In addition, the cross-linking of MSQ matrix with a 3D and highly crosslinked

Si-O network structure at  $T > 170^{\circ}\text{C}$  made the MSQ/SBS hybrid like a solid with very high viscosity,  $\sim 250,000$  poise. Thus, SBS porogen were trapped or “frozen” within the highly crosslinked MSQ matrix, leading to approximately constant porogen size ( $\sim 31\text{-}32$  nm) beyond  $T > 170^{\circ}\text{C}$ . This also accounted for the small porogen size and tight distribution ( $12 \pm 2$  nm) in the MSQ/porogen hybrid films cured rapidly at  $200^{\circ}\text{C}/\text{min}$ .

#### 4.4 Mechanical strength

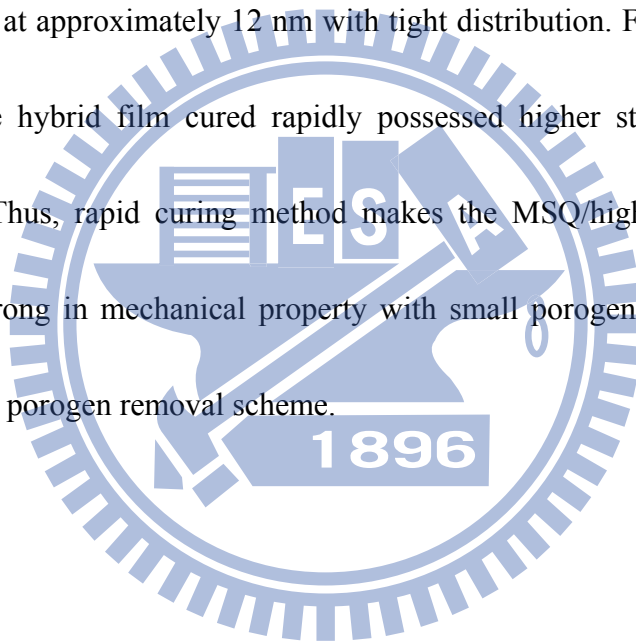
The elastic moduli of the hybrid films cured under slow and fast profiles measured by nano-indentation method were 4.9 and 5.6 GPa, respectively. For the same degree of MSQ crosslinking, their difference in the modulus was caused by the different porogen sizes. Based on *in-situ* GISAXS measurement for the hybrid film cured in the slow curing step, the porogen aggregated and formed an interconnected mass in the matrix with size up to 33 nm, reducing the mechanical strength of the hybrid film. In contrast, the hybrid film cured rapidly possessed higher strength due to a smaller porogen size ( $\sim 12$  nm) trapped within a highly crosslinked MSQ matrix. Thus, rapid curing method makes the MSQ/high-temperature porogen hybrid films strong in mechanical property with small porogen size and practical for the post-integration porogen removal scheme. In addition, rapid curing method has been widely adapted in the industry to shorten the

processing time and reduce cost. The low- $k$  films are typically prepared using a soft-bake on the hot-plate to removal the solvent, then cured or hard-baked at higher temperature in the furnace to burn out the porogen. Based on the results of this paper, we recommend that the soft-bake temperature is kept below the glass transition temperature of the porogen when rapid curing method is used. On the other hand, the hard-bake temperature should be kept at least higher than the immobilization temperature of low- $k$  matrix, which is  $> 170^{\circ}\text{C}$  for MSQ matrix in this paper.

## 4.5 Summary

The effect of the MSQ structures under different thermal cure profiles (slow:  $2^{\circ}\text{C}/\text{min}$  vs. rapid:  $200^{\circ}\text{C}/\text{min}$ ) on the porogen aggregation behavior and its size in the hybrid MSQ/SBS films cured up to  $200^{\circ}\text{C}$  were investigated by *in-situ* GISAXS, viscosity measurement, and FT-IR analysis. For slow curing, significant porogen diffusion and aggregation occurred between  $100$  to  $200^{\circ}\text{C}$ , at which the porogen size increased from  $12$  to  $34$  nm. The aggregation of SBS in the hybrid MSQ/SBS films were greatly influenced by the structural state of MSQ matrix at three controlling temperatures; namely (1) glass transition temperature,  $T_g$  ( $100^{\circ}\text{C}$ ), (2) onset temperature ( $160^{\circ}\text{C}$ ) for transforming cage to network structure, and (3) immobilization temperature ( $170^{\circ}\text{C}$ ). Porogen size started growing as SBS porogen aggregated at  $T > T_g$  of MSQ,

then increased at a higher rate at  $T > 160^{\circ}\text{C}$  as viscosity drastically dropped down to  $\sim 130,000$  poise due to the plasticization of vast amount of  $\text{H}_2\text{O}$  released by the condensation reaction of MSQ involving the transformation of cage to network structure, and finally remained about constant at  $\sim 32$  nm after  $170^{\circ}\text{C}$ , at which MSQ matrix was highly cross-linked to immobilize SBS particles. In contrast, upon rapid curing, the SBS porogen was trapped within a rapidly formed, well-crosslinked MSQ matrix, leaving its size unchanged at approximately 12 nm with tight distribution. Furthermore, the elastic modulus of the hybrid film cured rapidly possessed higher strength due to smaller porogen size. Thus, rapid curing method makes the MSQ/high-temperature porogen hybrid films strong in mechanical property with small porogen size and practical for post-integration porogen removal scheme.



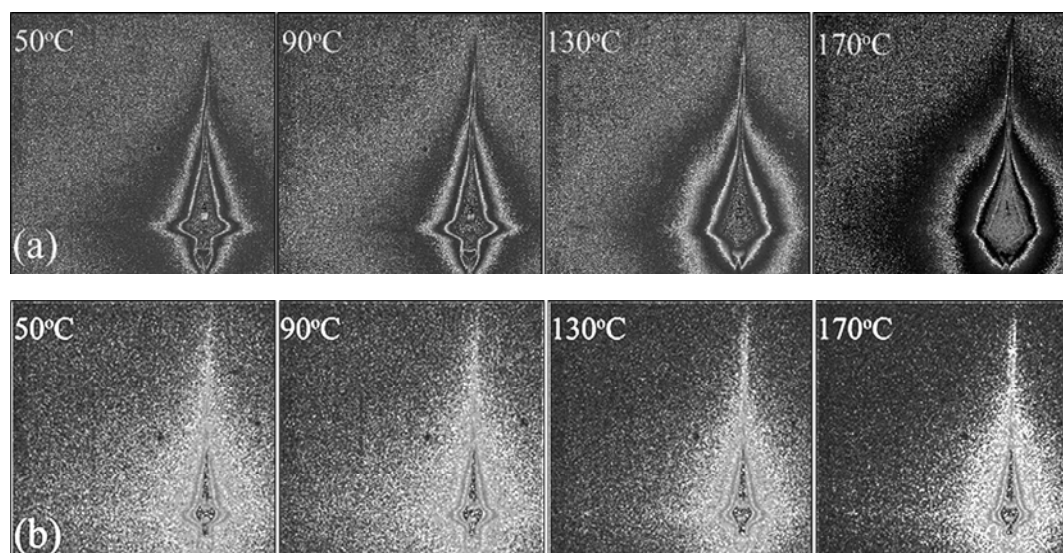
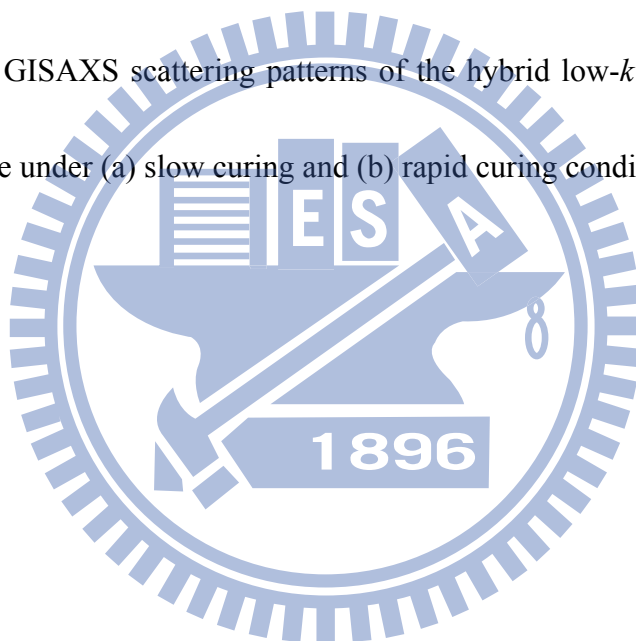


Figure 4.1 2-D GISAXS scattering patterns of the hybrid low- $k$  films as a function of cure temperature under (a) slow curing and (b) rapid curing condition.



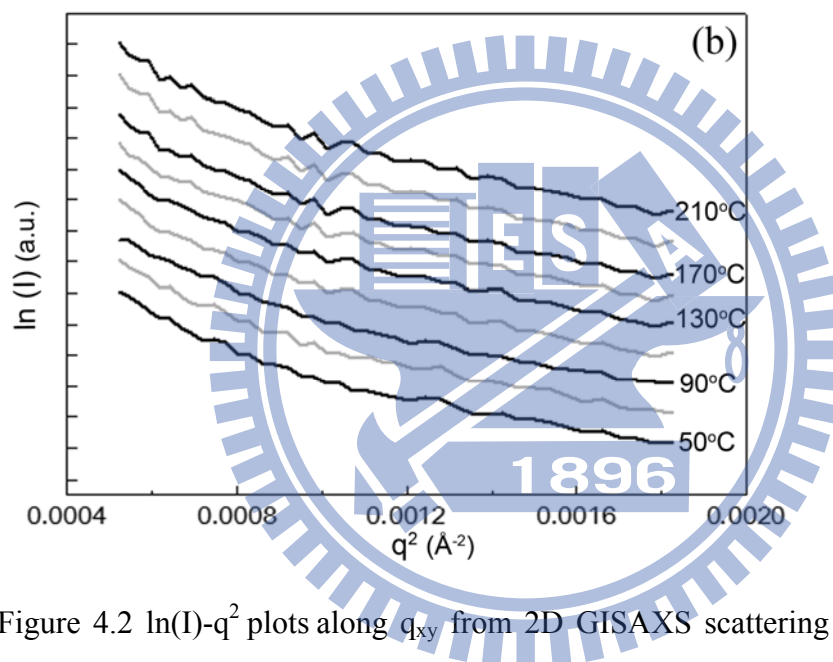
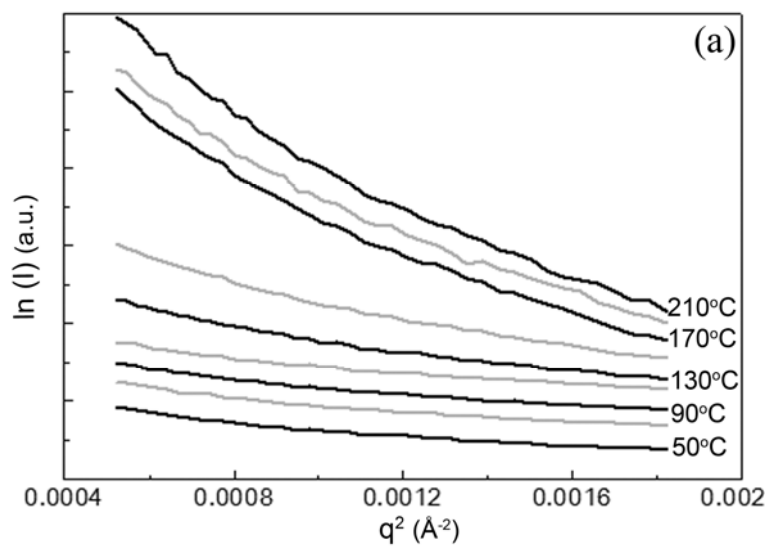


Figure 4.2  $\ln(I)$ - $q^2$  plots along  $q_{xy}$  from 2D GISAXS scattering patterns of the hybrid low- $k$  films cured at various temperatures under (a) slow and (b) rapid curing conditions.

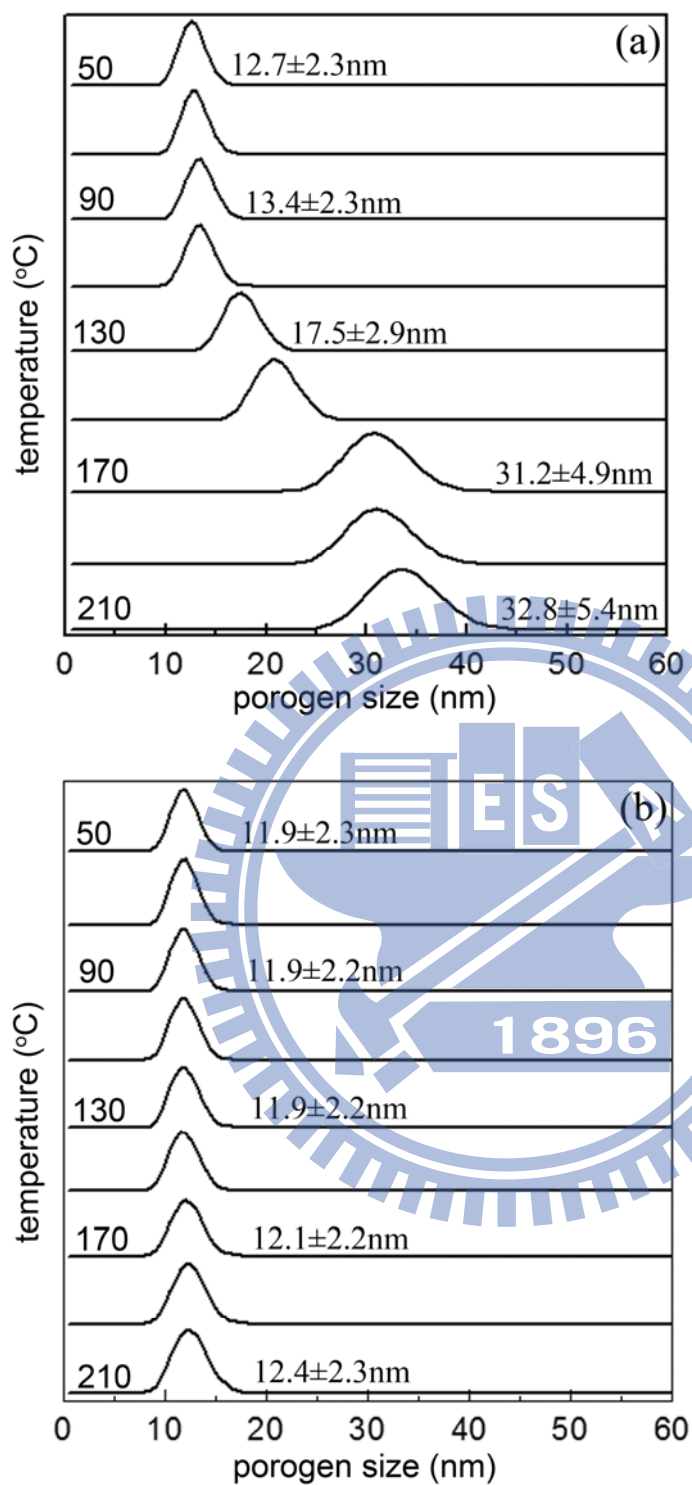


Figure 4.3 Porogen sizes in the hybrid low- $k$  films as a function of cure temperature under (a) slow and (b) rapid curing conditions.

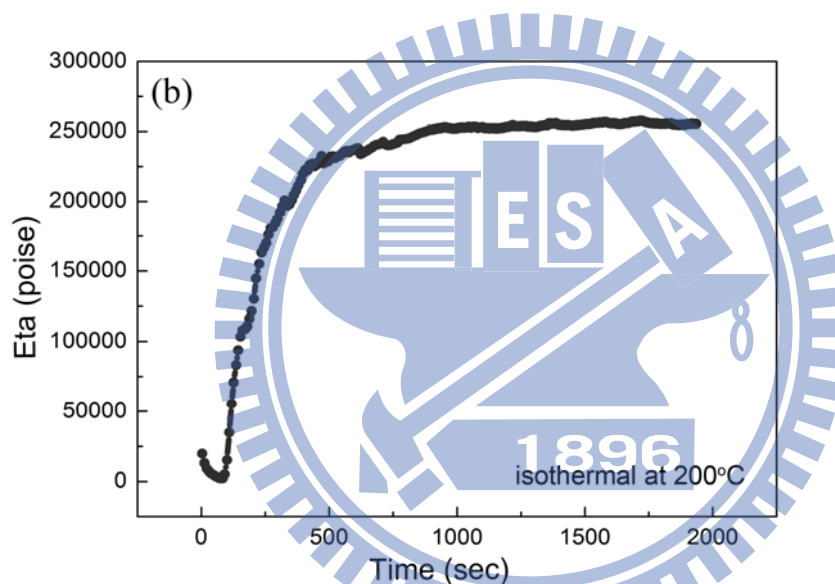
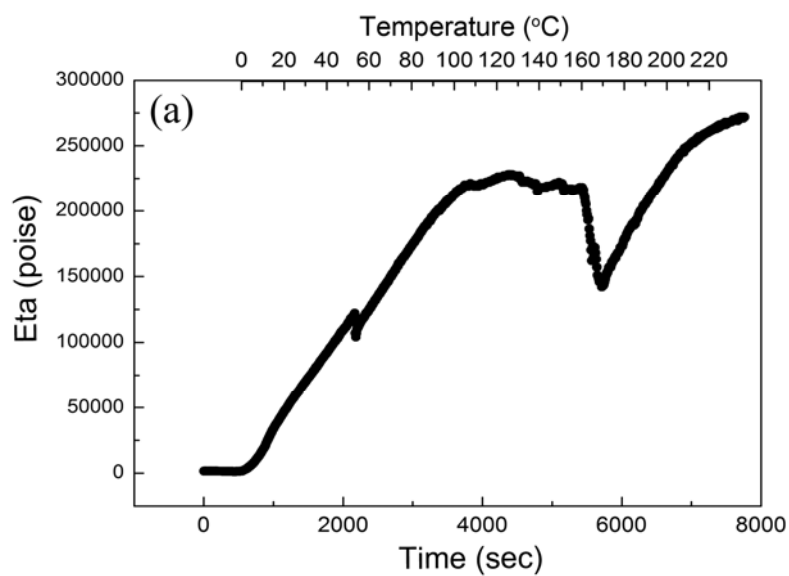


Figure 4.4 Viscosity of the hybrid low- $k$  films as a function of cure temperature under (a) slow curing profile at  $2^{\circ}\text{C}/\text{min}$  to  $250^{\circ}\text{C}$  (b) isothermal at  $200^{\circ}\text{C}$ .



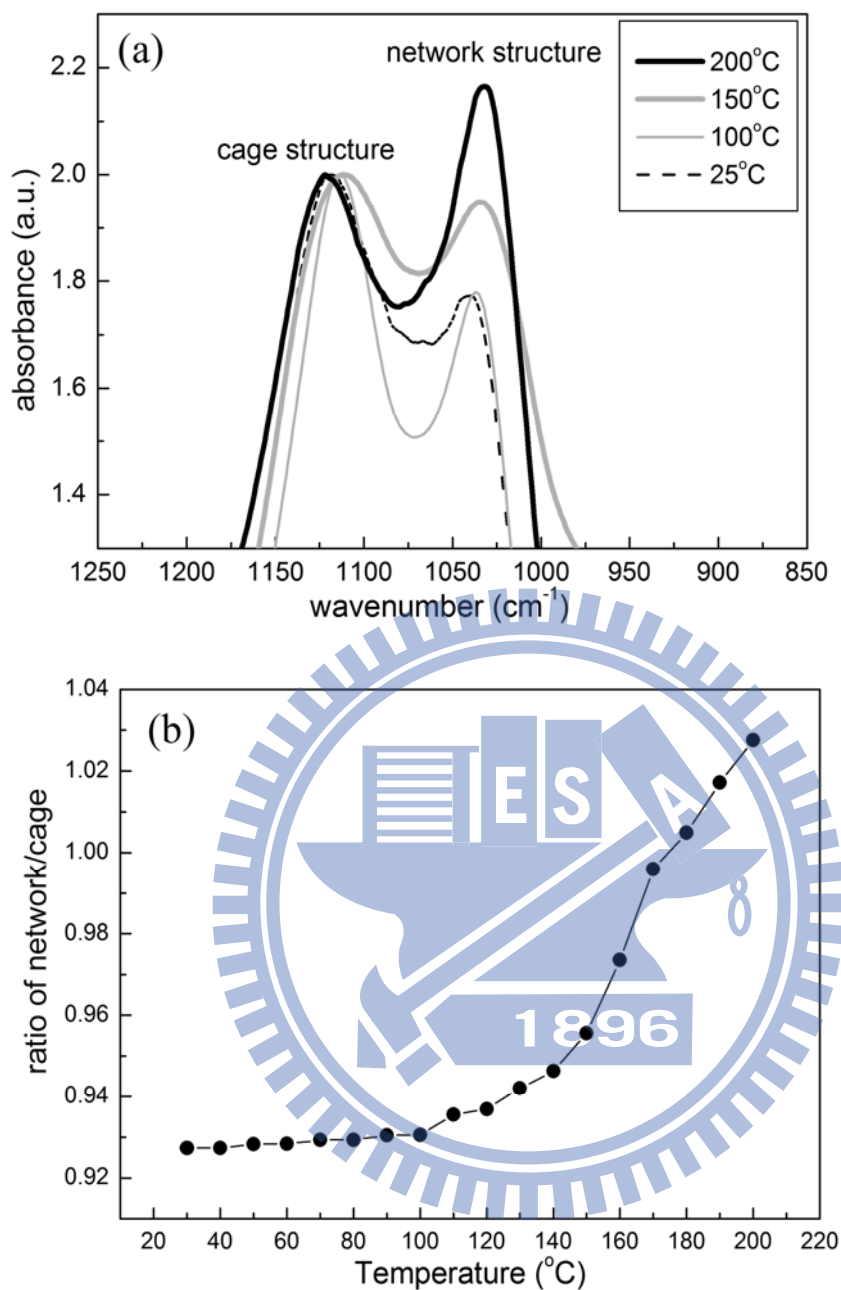


Figure 4.5 (a) Infrared spectra of MSQ/SBS hybrid films cured up to various temperatures: 25, 100, 150 and 200°C. (b) The ratio of network/cage structure in the MSQ/SBS hybrid films as a function of cure temperature between 30 and 200°C at an interval of 10°C.

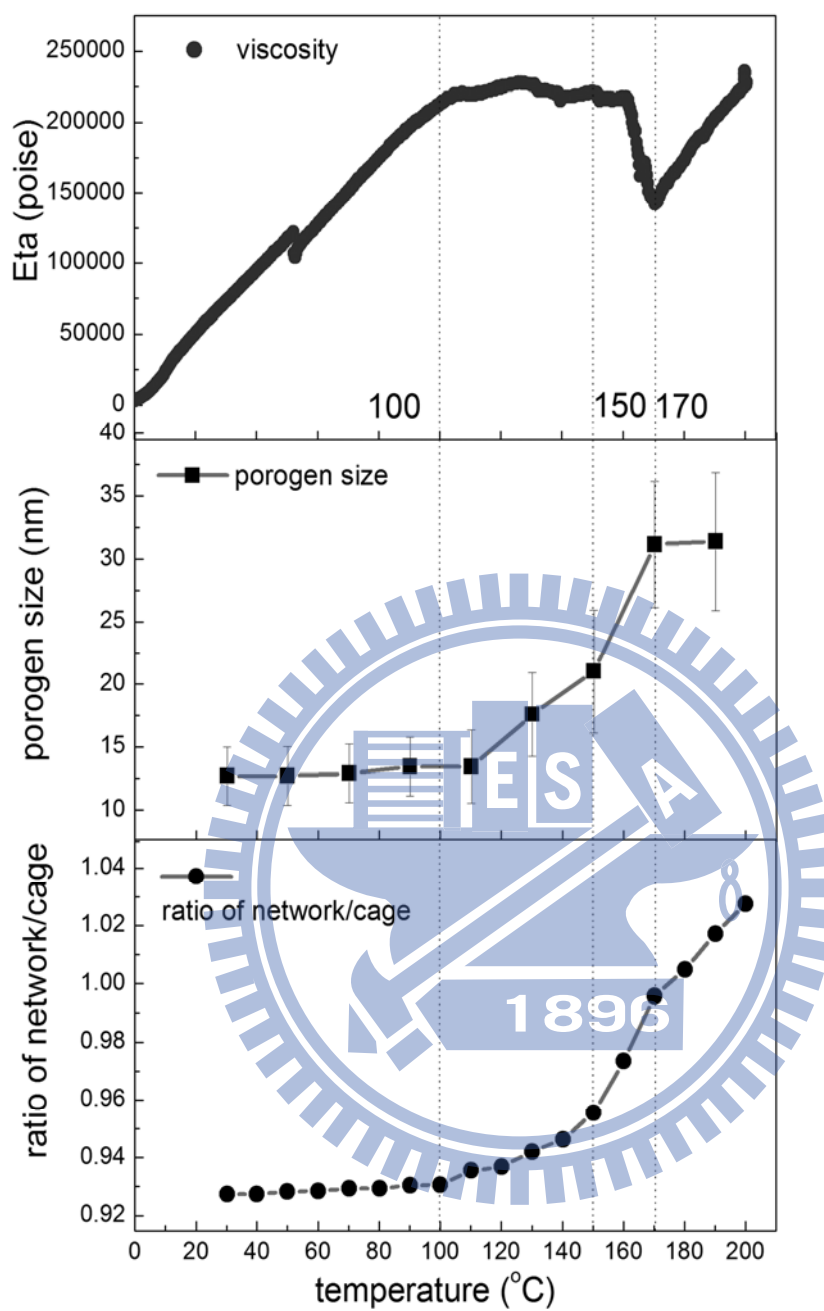


Figure 4.6 The viscosity, porogen size, and network/cage structure ratio of the MSQ/SBS hybrid films as a function of temperature during slow curing.

## Chapter 5

# Effect of Surfactants on the Porogen Size in the Low- $k$ Methylsilsesquioxane/Polystyrene Hybrid Films

This chapter explores the electrostatic and steric dispersion of polymer porogens within a low- $k$  matrix to control the porogen size in low- $k$  hybrid films at a slow cure rate. This study uses a commercial, spin-on organosilicate, MSQ, as the matrix and PS as a porogen in a novel post-integration porogen removal method for preparing porous low- $k$  MSQ film. An anionic surfactant (NaDBS) and a cationic surfactant (DB) were used to modify the PS surface in the solution and the MSQ/PS hybrid films. The effect of surfactant modification on the porogen and pore size in the low- $k$  methylsilsesquioxane (MSQ)/PS hybrid films at 10wt% PS loading, under a slow curing rate, was studied by *in-situ* GISAXS, viscosity measurement, and FT-IR analysis. The mechanism for determining the PS porogen aggregation with and without surfactant modification, as well as the porogen size and pore size, within a successively crosslinked MSQ matrix will be described and elucidated.

## 5.1 Porogen size in the precursor

Zeta potential has been recognized as a measure of the magnitude of the repulsion or attraction between particles in colloids [135]. Such measurement provides an insight into the dispersion of PS porogens in THF solvent. This helps us to understand how the porogen size in the solution is affected by the electrostatic dispersion due to surface modification of the PS. Table 5.1 summarizes the zeta potential and the corresponding particle size of PS porogen in the THF solution as a function of surface modification. The particle sizes of the PS in the solution were measured to be  $12.3 \pm 2.5$ ,  $49.3 \pm 4.1$  and  $11.2 \pm 2.4$  nm for PS/THF solutions at a pH value of 3, 7 (as-prepared without modification), and 11, respectively. And the corresponding zeta potentials of the PS/THF solution were 28, -18, and -40 mV. This indicates that a higher absolute surface potential led to a smaller PS particle size. The relationship between zeta potential and PS particle size can be described by Equation (5.1) [136].

$$\zeta = \frac{q}{4\pi\epsilon r} \quad (5.1)$$

where  $\zeta$  is the zeta potential of the particle,  $q$  is the electronic charge,  $\epsilon$  is the dielectric constant of the particle, and  $r$  is the radius of the particle. Our finding on the effect of pH values is consistent with an earlier report that the larger absolute value of potential ( $>25$  mV) results in better colloidal stability and a smaller particle size, due to electrostatic dispersion [135]. In addition, Table 5.1 shows that the particle sizes of PS

in the solution modified by anionic and cationic surfactants, were further reduced to  $9.0 \pm 2.0$  nm and  $8.0 \pm 1.8$  nm because of their relatively higher, absolute surface potential of -58 and +66 mV, respectively.

## 5.2 *In-situ* porogen size test

Based on the particle size data, we will focus on the modification of PS by anionic and cationic surfactant for producing low- $k$  MSQ/PS hybrid film and the corresponding porous low- $k$  film in this study. More specifically, MSQ matrix precursor was added to PS/THF solutions with and without surfactant modification. Subsequently, the solutions were spin-coated onto silicon wafer to fabricate the as-prepared low- $k$  hybrid films. The sizes of PS porogens in the hybrid low- $k$  films, cured at a slow rate, i.e.  $2^{\circ}\text{C}/\text{min}$  from 30 to  $200^{\circ}\text{C}$ , was then *in situ* characterized by 2D GISAXS. Fig. 5.1 show the GISAXS patterns of the low- $k$  PS/MSQ hybrid films at representative temperatures from 30 to  $190^{\circ}\text{C}$  ( $40^{\circ}\text{C}$  intervals) for PS porogens without and with NaDBS and DB surfactant modification, respectively. With increasing temperature, scattering patterns illustrated in Figure 5.1(a), were confined in the low- $q$  region, indicating that the PS porogens tended to aggregate and did not disperse well in the low- $k$  PS/MSQ hybrid film. In contrast, the scattering patterns shown in Figure 5.1(b) NaDBS and (c) DB were stronger and more uniform in the high- $q$  region than the corresponding ones without surface modification

(Figure 5.1(a)). The results of these successive scattering patterns indicates that the porogen size in the modified low- $k$  hybrid films was smaller than that of the unmodified films at the same cure temperatures.

In order to compare the effect of surfactant treatment on the porogen size and its evolution during the curing step, the PS porogen size/distribution was quantitatively determined by the same method described in chapter 4. Accordingly, the calculated porogen size and distribution of the hybrid low- $k$  films with and without NaDBS and DB modification, as a function of curing temperatures are shown in Figure 4.2(a), (b) and (c), respectively. For low- $k$  hybrid film without modification shown in Figure 4.2(a), the porogen size/distribution increased noticeably from  $10.0 \pm 2.4$  nm to  $16.5 \pm 5.5$  nm from 30 to 190°C. Moreover, the increased rate of porogen size became noticeable at  $T \geq 110^\circ\text{C}$ , and more significant between 130 and 170°C (from  $11.4 \pm 3.9$  nm to  $15.6 \pm 4.9$  nm), but less between 170 and 190°C (from  $15.6 \pm 4.9$  nm to  $16.5 \pm 5.5$  nm). In the NaDBS modification case (Figure 4.2(b)), the porogen size and distribution increased slightly and linearly from  $9.0 \pm 2.0$  nm at 30°C to  $11.1 \pm 2.4$  nm at 190°C. In contrast, for PS modified by DB (Fig. 2c), the porogen size and distribution changed only slightly from  $7.8 \pm 1.0$  nm at 30°C to  $8.7 \pm 2.0$  nm at 190°C. Overall, modification of PS porogen by cationic surfactant, DB yielded the smallest porogen size and tightest distribution.

### 5.3 Pore size, distribution and porosity

Next, we examine the pore size in the porous low- $k$  MSQ films after removing the PS porogens in the above-mentioned 3 different MSQ/PS hybrid films at 400°C. Figure 5.3(a)-(c) show the GISAXS patterns of the porous low- $k$  MSQ films prepared from the unmodified PS, NaDBS-modified PS, and DB-modified PS system, respectively. The stronger scattering intensities in Figure 5.3(b) and (c) indicate smaller and uniform pores in the porous films prepared from surfactant-modified PS porogens. Specifically, the pore sizes were calculated to be 16.8, 11.5, and 8.8 nm for these 3 different systems. In addition, the porosity of the porous low- $k$  film at 10wt% PS loading was found to be 15.6% by using the XRR technique. Compared to the porogen size in the hybrid films cured at 190°C, there was little aggregation of PS porogens once MSQ was fully cross-linked at 200°C.

### 5.4 Structure variation vs. porogen behavior

Based on particle analysis of the PS/THF solution and *in situ* GISAXS analysis of the low- $k$  MSQ/PS hybrid films, the PS size in the solution and the hybrid film, then the pore size after burn-out, can be summarized below. The PS particles in the THF solvent without modification could diffuse and aggregate readily into large particles with a size

of 49.3 nm. When MSQ precursor was added to the solution to form a low- $k$  hybrid film, the PS porogen size was found to be 10.0 nm at 30°C. These results indicate that PS particles without surfactant treatment were shrunk by the presence of MSQ matrix precursor in the hybrid film due to the steric effect [137,138]. In contrast, the PS with NaDBS and DB modification in the solution showed a much smaller particle size of 9.0 and 8.0 nm, respectively. The difference can be attributed to the electrostatic dispersion due to their higher absolute zeta potentials as described in the previous section. When MSQ precursor was added to the PS/THF solution with NaDBS and DB modification, then spin-coated to form a low- $k$  hybrid film, the PS porogen size remained at 9.0 and 7.8 nm at 30°C, respectively. This indicates that the electrostatic dispersion effect by surfactant was dominant over the steric effect by MSQ matrix.

When the low- $k$  hybrid films were further cured to 190°C, the porogen size was increased by 23.3% from 9.0 to 11.1 nm for the NaDBS-modified PS system; and increased by 11.5% from 7.8 to 8.7 nm for the DB-modified PS system, but increased significantly, by 65.0% from 10.0 to 16.5 nm for the system without modification. After the removal of PS porogens at 400°C, the pore sizes were about the same as those at cured at 200°C, showing that there was little aggregation of PS porogens once MSQ was fully cross-linked at 200°C. Thus, surfactant modification of PS, especially by DB, can achieve and maintain a small pore size with tight distribution, even at a slow cure rate,



i.e. 2°C/min. Thus, the porogen aggregation behavior within the cross-linkable MSQ matrix as a function of cure temperature up to 200°C is critical for controlling the porogen and pore size after burn-out. This will be addressed in the following sections.

*In situ* viscosity measurement was carried out from room temperature to 200°C to examine any aggregation of porogens and the interaction between porogens and progressively cross-linked MSQ. In addition, the cross-linking behavior of MSQ in the low-*k* MSQ/PS hybrid films was investigated by FTIR analysis. The viscosity, porogen size, and network/cage structure ratio of the MSQ/PS hybrid films with and without modification, as a function of temperature at a heating rate of 2°C/min from 30 to 200°C, are shown in Figure 5.4(a), (b), and (c), respectively. In the unmodified case, porogen size did not change much at  $T < 100^{\circ}\text{C}$ . Then, the viscosity reached a plateau and remained at  $\sim 2.3 \times 10^5$  poises between 105°C and 160°C (Figure 5.4(a)). The porogen size noticeably increased by 15% (relative to the size at 30°C) at 130°C and 33% at 150°C (Fig. 4b). As the cure temperature was further increased, the viscosity would drop at the on-set temperature of about 160°C and reached its lowest value,  $\sim 1.8 \times 10^5$  poises at 175°C (Figure 5.4(a)), while the porogen size was enlarged by 50% to 170°C (Figure 5.4(b)). In the last stage up to 190°C, the porogen size increased by 65%. But, the rate of size change was reduced because MSQ was almost entirely cross-linked as illustrated by the network/cage ratio.

The results indicate that the PS porogen without treatment can diffuse and aggregate readily in the relaxed MSQ structure at  $T_g \leq T \leq 160^\circ\text{C}$ . The aggregation was enhanced at  $T > 160^\circ\text{C}$  due to viscosity reduction by  $\text{H}_2\text{O}$  released from the on-set of condensation, i.e. cross-linking of the MSQ matrix, resulting in an increase in porogen size at a faster rate. At  $T > 175^\circ\text{C}$ , viscosity increased again as the cross-linking of the MSQ matrix was near completion, leading to a continued increase in porogen size to 16.5 nm at  $200^\circ\text{C}$ , but a lower rate.

In the NaDBS-modified PS case, Figure 5.4(b) shows that the PS porogen size increases very little from 9.0 nm at  $30^\circ\text{C}$  to  $\sim 10$  nm at  $150^\circ\text{C}$ , then to 11.0 nm at  $T > 170^\circ\text{C}$ . Interestingly, it exhibits higher viscosity ( $\sim 2.3 \times 10^5$  poises) than the hybrid film without modification ( $\sim 2.2 \times 10^5$  poises) in the  $105^\circ\text{C}$  to  $160^\circ\text{C}$  range as shown in Fig. 4a. While the on-set temperatures for the viscosity drop ( $160^\circ\text{C}$ ) and viscosity pickup ( $175^\circ\text{C}$ ) for both systems are the same, the viscosity of the NaDBS-modified hybrid film remained higher,  $\sim 2.3 \times 10^5$  poises at  $160^\circ\text{C}$  and  $\sim 2.0 \times 10^5$  poises (vs.  $\sim 1.8 \times 10^5$  poises for the unmodified system) at  $175^\circ\text{C}$ . The degree of cross-linking of the MSQ matrix in the NaDBS-modified MSQ/PS hybrid system (Figure 5.4(c)) was slightly lower than the unmodified system, presumably due to its higher viscosity. Nevertheless, this indicates that the addition of anionic surfactant does not noticeably affect the cross-linking behavior of MSQ. This is confirmed by the same on-set temperatures of

viscosity drop at 160°C and the rapid rise in viscosity at ~175°C as shown in Figure 5.4(a).

In the cationic DB-modified PS system, Fig. 4b shows that the PS porogen size increases very little from 7.8 nm at 30°C to ~8.7 nm at  $T > 170^\circ\text{C}$ . This system exhibited higher viscosity (max.  $\sim 2.4 \times 10^5$  poises) than the hybrid film without modification (max.  $\sim 2.2 \times 10^5$  poises) and even the NaDBS-modified hybrid film (max.  $\sim 2.3 \times 10^5$  poises) throughout the whole temperature range. Moreover, its viscosity did not show an obvious plateau prior to the on-set condensation temperature, i.e. at  $T_g \leq T \leq 160^\circ\text{C}$ . However, the viscosity curve shows that the on-set temperature of viscosity drop in the DB-modified PS system was delayed by about 5°C, compared to the other two conditions. Also, the degree of cross-linking of the MSQ matrix in the DB-modified PS system (Figure 5.4(c)) was the lowest. This shows that the addition of cationic surfactant does noticeably affect the cross-linking behavior of MSQ in the hybrid film during the curing step.

The interaction between MSQ and surfactant-modified PS was then further investigated by monitoring changes in the of Si–OH infrared absorption band in the 905-930  $\text{cm}^{-1}$  region of the MSQ/PS hybrid films at room temperature by FTIR spectroscopy. Figure 5.5 show a cage Si–O structure at  $\sim 1130 \text{ cm}^{-1}$  and a network Si–O structure at  $\sim 1030 \text{ cm}^{-1}$  [139], and a Si–OH stretching band in the 905-930  $\text{cm}^{-1}$  region

[140,141]. In particular, the peak positions of Si-OH of MSQ for the unmodified, NaDBS-, and DB-modified PS systems were 922, 924, and 908  $\text{cm}^{-1}$ , respectively. Compared to the unmodified and anionic surfactant-modified PS systems with a negative surface potential, the strong red shift, 14  $\text{cm}^{-1}$  in the Si-OH band for the cationic DB-modified PS system can be attributed to columbic attraction [142] between the electron lone pair of oxygen atoms of the Si-OH group and the positively charged PS particles (with a surface potential of +66 mV).

## 5.5 Matrix structure variation with charged porogen

The next task is to clarify whether the attractive force between the Si-OH and DB-modified PS porogen affects the MSQ matrix cross-linking and porogen aggregation during the curing step. Therefore, the peak positions and peak intensities of the Si-OH absorption band of MSQ with and without modification, as a function of cure temperature are further examined and illustrated in Figs. 6a and 6b, respectively. Figure 5.6(a) shows that the peak positions of Si-OH in the negatively charged PS system remained at  $\sim 922 \text{ cm}^{-1}$  without any obvious change at  $T \leq 140^\circ\text{C}$ . This implies that the electrostatic force between charged PS and MSQ is not affected by cure temperature below  $140^\circ\text{C}$ . The peak position then shifted noticeably to  $908 \text{ cm}^{-1}$  at temperatures between  $140^\circ\text{C}$  and  $160^\circ\text{C}$ . This can be attributed to the hydrogen bonding

interaction [143] as Si–OH groups come in a closer range due to a drop of viscosity, and start a condensation reaction at this stage. Similarly, the peak position of the positively charged, DB-modified PS system remained at  $905\text{ cm}^{-1}$  until  $150^{\circ}\text{C}$ , then shifted gradually to  $898\text{ cm}^{-1}$  due to the cross-linking of MSQ. The Si–OH band was still present at  $170^{\circ}\text{C}$ , which is about  $10^{\circ}\text{C}$  offset compared to the negatively charged and unmodified PS systems.

Fig. 6b shows that the intensity of the Si–OH peak decreases with increasing cure temperatures of  $> 100^{\circ}\text{C}$ , except that the rate of change is much slower for the DB-modified PS system. The decrease in the Si–OH band intensity was due to the condensation of Si–OH groups in the MSQ precursor, leading to a cross-linked, cage to network Si–O structure [128]. Thus, the cross-linking rate in the positively charged, DB-modified system was slower than those in the negatively charged PS systems (without modification or NaDBS-modified) presumably due to the columbic attractive force between Si–OH and positively charged PS porogens, as evidenced by the red-shift in the Si–OH band (Figure 5.5).

Based on the FTIR results, the interaction mechanism between the MSQ matrix and surfactant-modified PS porogen, especially the positively charged, DB-modified PS can be elucidated. Its correlation with the degree of cross-linking, the viscosity, and the porogen size in the hybrid films prepared at a slow cure rate, using GISAXS, FTIR and

viscosity measurements, is also clarified. The aggregation of the PS porogen in the low- $k$  hybrid PS/MSQ films is greatly influenced by electrostatic stabilization [144], steric stabilization of cross-linkable MSQ matrix, and interaction between the MSQ matrix and surface-modified PS, depending on the zeta potential and charge state of surfactants.

## 5.6 Dispersion mechanism

As with our previous work on MSQ/polystyrene-*b*-polybutadiene-*b*-polystyrene (SBS) porogen, the steric barrier effect on the PS porogens is affected by the microstructure of the cross-linkable MSQ matrix at three significant temperatures in the cure step; namely, (1) the glass transition temperature,  $T_g$  ( $\sim 100^\circ\text{C}$ ), (2) the onset temperature,  $160^\circ\text{C}$  for transformation from cage to network structure, and (3) the immobilization temperature,  $175^\circ\text{C}$ , which have been described in Figure 5.4(a)-(c). Noticeable porogen aggregation occurred at  $T > T_g$ , but the aggregation occurred at a different rate during these 3 stages, depending on the diffusivity of PS particles, which is a function of viscosity and temperature as described by the Einstein-Stokes equation (Equation 5.2):

$$D = \frac{k_B T}{6\pi\eta r} \quad (5.2)$$

where  $k_B$  is the Boltzmann constant,  $T$  is the absolute temperature,  $\eta$  is the viscosity of

the system and  $r$  is the particle radius. In this study,  $\eta$ , is a measure of the steric and electrostatic barrier to movement of the PS particles within the cross-linkable MSQ matrix. Thus, at  $T > T_g$ , the relaxation of the PS and MSQ molecular chains leads to reduced viscosity and higher diffusivity of the PS particles. Such high diffusivity increases PS collisions and leads to the aggregation of PS porogens from 10.0 to 13.4 nm. At  $T > 160^\circ\text{C}$ , the viscosity drops drastically to  $\sim 1.8 \times 10^5$  poises, because of the plasticization by the large amount of  $\text{H}_2\text{O}$  by-products when extensive transformation of cage to network Si–O occurs in the MSQ. This results in greater aggregation of the PS porogens, resulting in a faster change in the porogen size, from 13.4 to 15.6 nm, between 150 and  $175^\circ\text{C}$ . In the final stage,  $\sim 175$  to  $200^\circ\text{C}$ , most  $\text{H}_2\text{O}$  is believed to have dried off at less than  $175^\circ\text{C}$ . In addition, the cross-linking of the MSQ matrix with a 3D and highly cross-linked Si–O network structure at  $T > 175^\circ\text{C}$  makes the MSQ/PS hybrid behave like a solid, with a very high viscosity of  $\sim 2.2 \times 10^5$  poises. As a result, the PS porogens are trapped or “frozen” within the highly cross-linked MSQ matrix, leading to an approximately constant porogen size of 15.6 to 16.5 nm, beyond  $T > 175^\circ\text{C}$ .

When the surfactant, either anionic or cationic, is added to PS in THF solution, negative or positive charges build up on the PS particle surface. As a result, the charged PS porogens repel each other and do not aggregate. This electrostatic repulsion also plays the dominant role in hindering the aggregation of PS porogens in the NaDBS- and

DB-modified PS/MSQ hybrid films during the slow cure process from 30 to 200°C. Since the surfactant is physically adsorbed only on the PS particle surface, the surface charge on the PS particles may change over time and temperature, if the surfactant desorbs from the surface, during the cure process. However, NaDBS and DB have been reported or tested to possess excellent thermal stability up to at least 200°C [145]. Therefore, the surface density of NaDBS- or DB-modified PS particles would not be expected to degrade as the cure temperature rises to 200°C [146,147]. Compared to a weakly electrostatic dispersed PS/MSQ system without modification (zeta potential: -18 mV), the NaDBS-modified PS/MSQ system (zeta potential: -58 mV) and DB-modified PS/MSQ system (zeta potential: +66 mV) exhibits strong electrostatic repulsion, resulting in little or limited aggregation of PS porogens during a slow cure process, which produces a small porogen size with a tight distribution.

The charge on the particles has an effect on the increased viscosity, depending on the surface charge density, because the electrical double layer around each particle is distorted under shearing, *i.e.* the electroviscous effect [148,149]. This increased viscosity can be quantified and taken into account by introducing a correction factor, *i.e.* the primary electroviscous coefficient,  $p$ , to the modified Einstein-Stokes equation [150] (Equation 5.3):

$$\eta_r = 1 + k(1 + p)\phi \quad (5.3)$$



where  $\eta_r$  is the relative viscosity,  $\phi$  is the volume fraction of the solid and  $k=2.5$  for spherical and rigid particles. The “p” coefficient [145] can be represented by Equation

(5.4)

$$p = \frac{(2\varepsilon_0\varepsilon_r\zeta)^2}{\lambda_0\eta_0a^2} \quad (5.4)$$

where  $\varepsilon_0$  is the permittivity of free space,  $\varepsilon_r$  is the relative permittivity,  $\zeta$  is the zeta potential,  $\lambda_0$  is the specific conductivity of the continuous phase,  $\eta_0$  is its viscosity and  $a$  is the diameter.

A higher zeta potential leads to a higher viscosity, which accounts for the difference in viscosity among the three different MSQ/PS hybrid films as illustrated in Figure 5.4(a) at  $T > T_g$ . As a result, the diffusivity of the highly-charged PS porogens is hindered by the increased viscosity. Therefore, the high zeta potential of charged PS porogens further impedes the segregation and aggregation of PS within a successively cross-linked MSQ matrix through electrostatic repulsive forces and the electroviscous effect. In addition, the columbic attraction between the electron lone pair of the oxygen atoms of the Si–OH group and the positively charged PS particles, restrains the PS porogen and its mobility during the cure step, resulting in a further reduction in porogen aggregation. Overall, the NaDBS modified-PS/MSQ hybrid film yielded a small porogen size and tight distribution ( $8.7 \pm 2$  nm) when cured at a slow rate up to 200°C with MSQ fully cross-linked, and a similarly small pore size (8.8 nm) after burning out

of porogen at 400°C. In comparison, our previous work on low-*k* MSQ/SBS hybrid film used a rapid curing method to trap the porogen within a rapidly formed, well-cross-linked MSQ matrix, leaving its size unchanged (from as-prepared, 25°C) with tight distribution. Thus, surface modification of PS porogens by cationic surfactant offers an alternative and simple method to control the porogen and pore size and distribution even at a slow cure rate (2°C/min), which offers great process latitude. This simple method based on polystyrene porogen with surface potential modification, can be further improved by reducing the pore size and extended to other relevant materials as the porogen. In principle, the porogen particle size in the solvent can be reduced by using a porogen of a lower molecular weight [151] and with treatment leading to a higher surface potential [152,153]. As a result, a smaller pore size can be expected after the removal of porogen from the corresponding low-*k*/porogen hybrid film. In addition to polystyrene, the porogen materials can be selected from linear polymers such as polyethylene, polypropylene, poly(methyl methacrylate) [154], poly(alkylene ether)s (e.g., poly(ethylene oxide) (PEO) and poly(propylene oxide) (PPO)) [155] of lower molecular weight and good miscibility with low-*k* matrix precursors, such as MSQ.

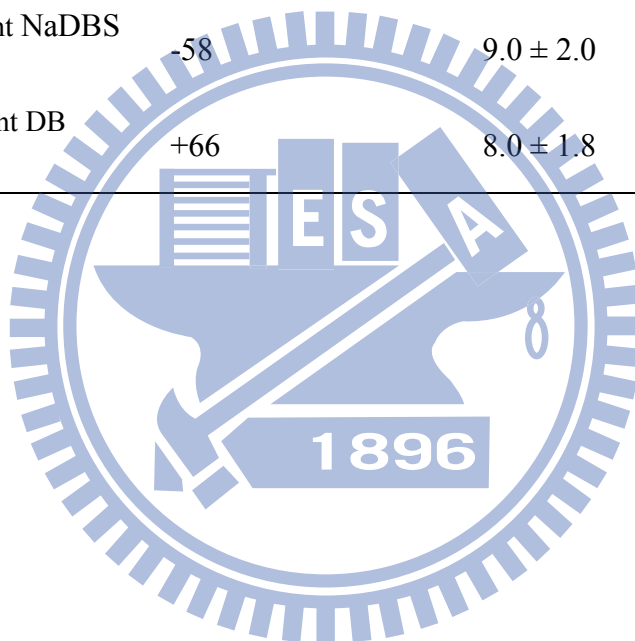
## 5.7 Summary

An anionic surfactant, NaDBS, and a cationic surfactant, DB, were used to modify

the surface potential of PS porogen in THF solution from an initial value of -18 mV (unmodified) to -58mV and +66mV, respectively. Upon curing at a slow rate (2°C/min), the porogen without modification aggregates and its size increases from 10.0 to 16.5 nm. In contrast, for the NaDBS-modified and DB-modified PS systems, the high zeta potential of charged PS porogens impede the aggregation of PS within a successively cross-linked MSQ matrix through electrostatic repulsion forces and the electroviscous effect. This results in little or limited PS porogen aggregation and yields a small porogen size with tight distribution,  $11.1 \pm 2.4$  and  $8.7 \pm 2.0$  nm, respectively. More importantly, the columbic attraction between the Si-OH groups of MSQ matrix and the DB-modified, positively charged PS particles, restrains the PS porogen and its mobility during the cure step, resulting in a further reduction in porogen aggregation. Overall, the NaDBS modified-PS/MSQ hybrid film yields a small porogen size and tight distribution ( $8.7 \pm 2$  nm) when cured at a slow rate up to 200°C with MSQ fully cross-linked, and a similarly small pore size (8.8 nm) after burning out of porogen at 400°C.

Table 5.1 The zeta potential and the corresponding particle size of PS porogen in the solution as a function of surface modification.

Treatment on PS	Zeta potential (mV)	PS particle size (nm)
No modification	-18	$49.3 \pm 4.1$
pH = 3	+28	$12.3 \pm 2.5$
pH = 11	-40	$11.2 \pm 2.4$
Anionic surfactant NaDBS	-58	$9.0 \pm 2.0$
Cationic surfactant DB	+66	$8.0 \pm 1.8$



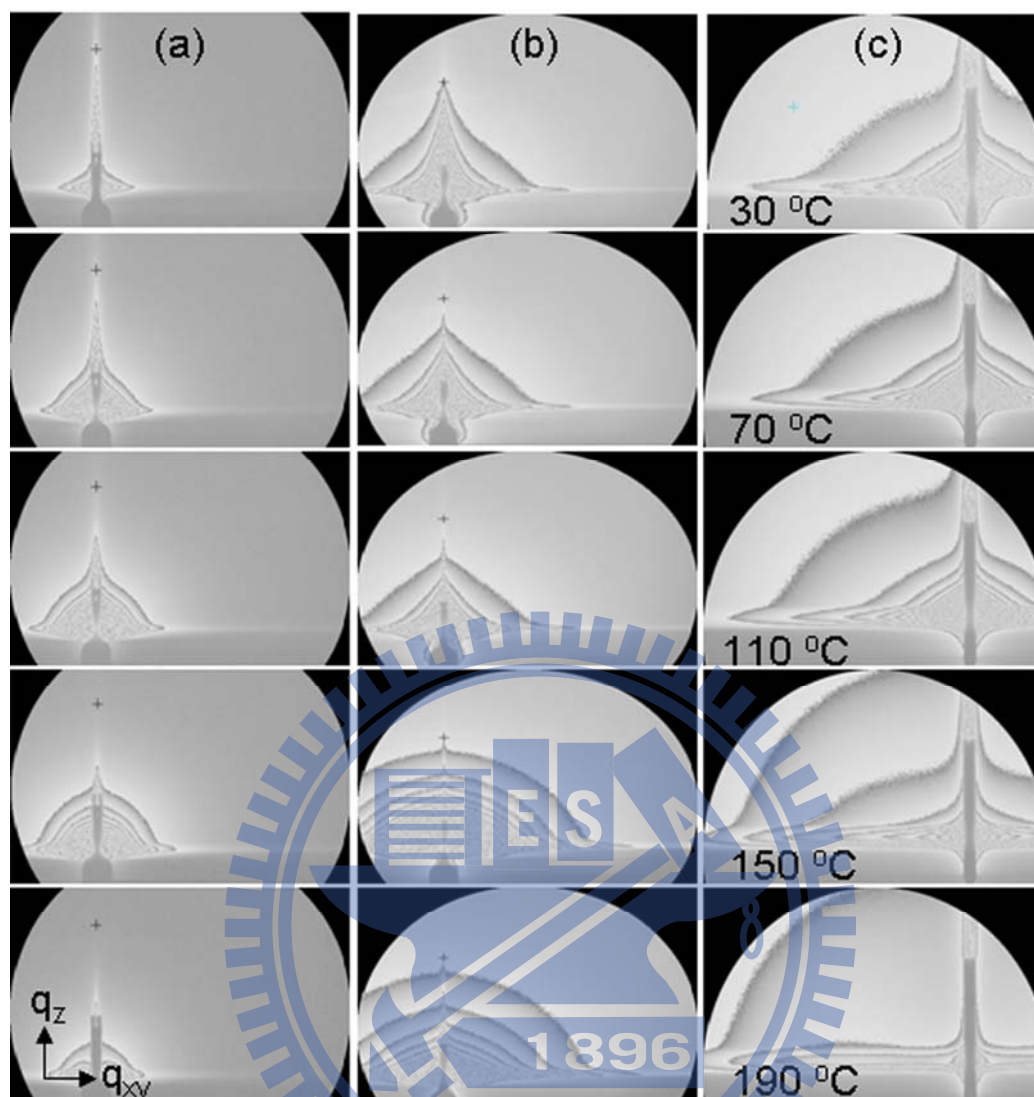
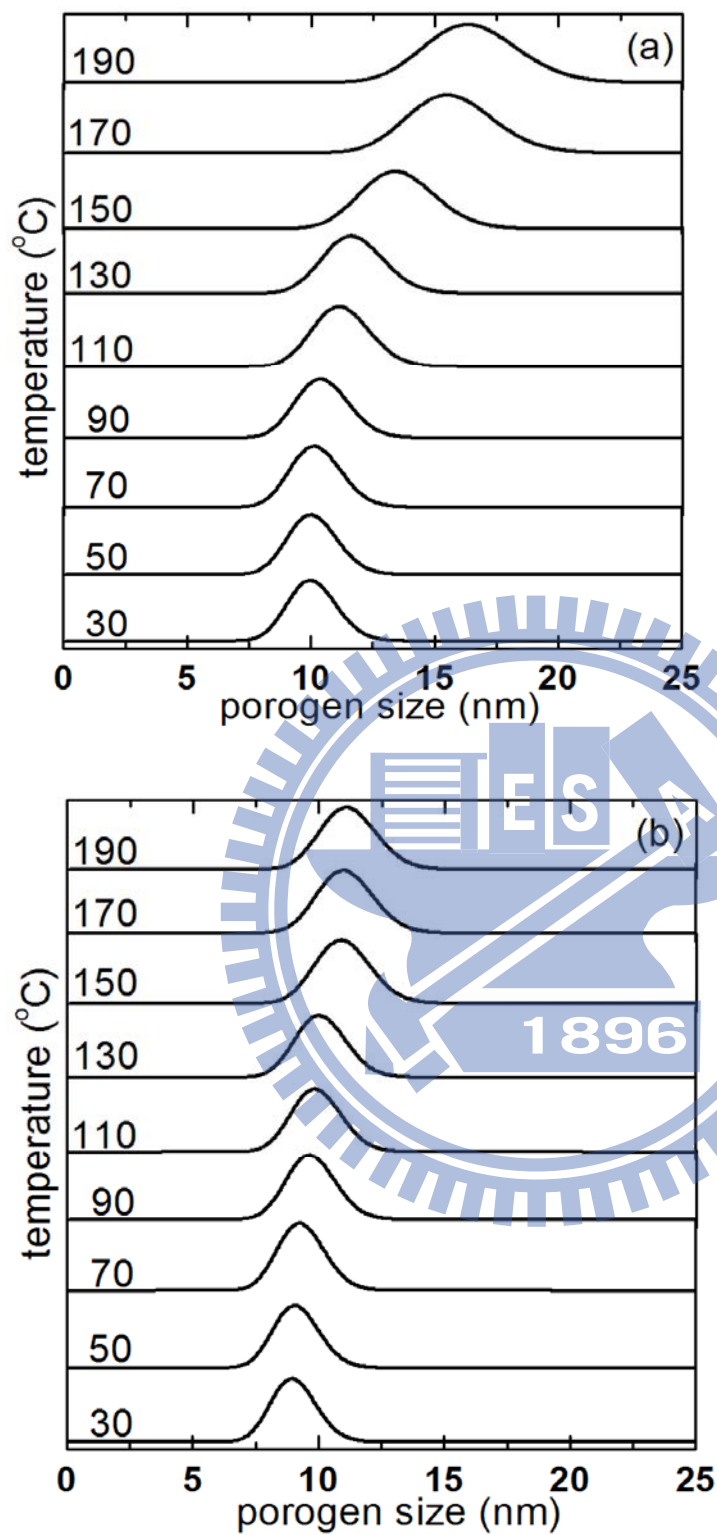


Figure 5.1 2-D GISAXS scattering patterns of the low- $k$  MSQ/PS hybrid films as a function of cure temperature: (a) PS without modification, (b) NaDBS-modified PS, and (c) DB-modified PS.



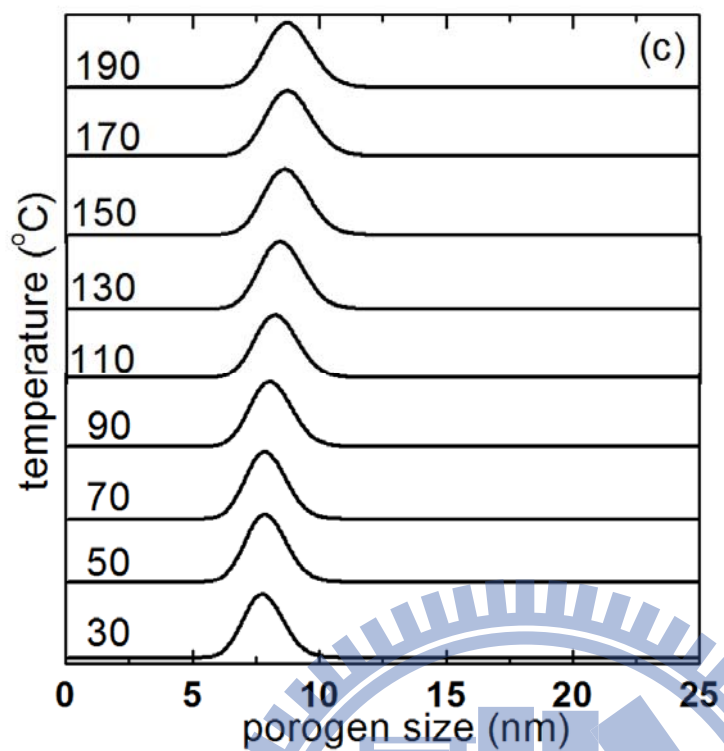


Figure 5.2 Porogen sizes and distribution in the low- $k$  MSQ/PS hybrid films as a function of cure temperature: (a) PS without modification, (b) NaDBS-modified PS, and (c) DB-modified PS.

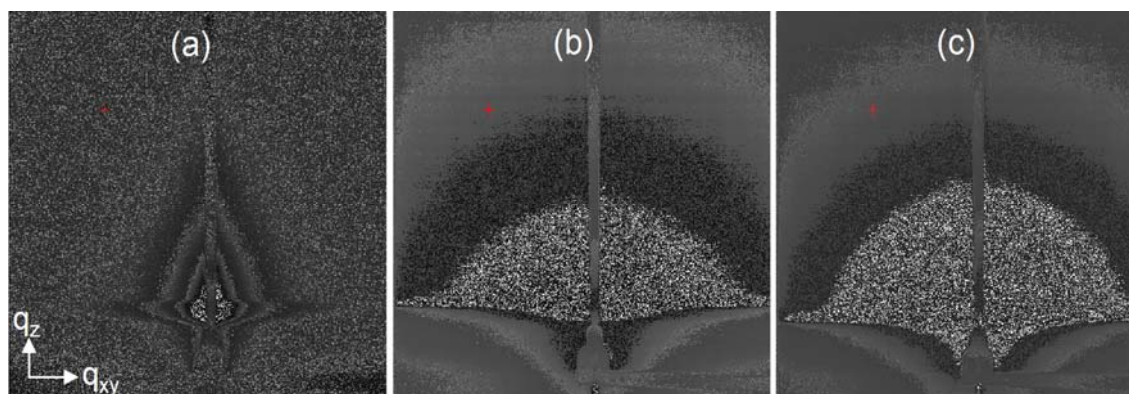


Figure 5.3 2-D GISAXS scattering patterns of the low- $k$  porous MSQ films after removal of PS porogens at 400°C: (a) PS without modification, (b) NaDBS-modified PS, and (c) DB-modified PS.





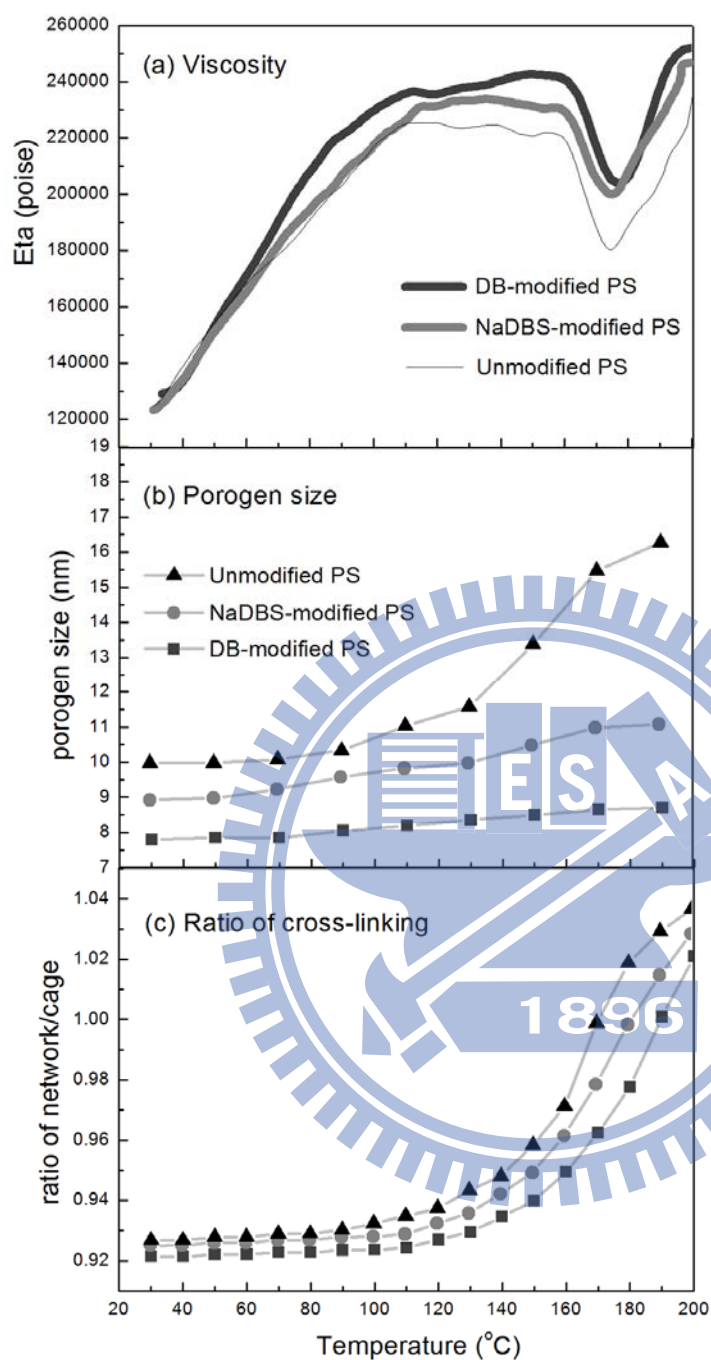


Figure 5.4 (a) The viscosity, (b) porogen size, and (c) the ratio of network-/cage- Si-O in the low- $k$  MSQ/PS hybrid films as a function of cure temperature for NaDBS-modified PS (●), DB-modified PS (■), and PS without modification (▲).

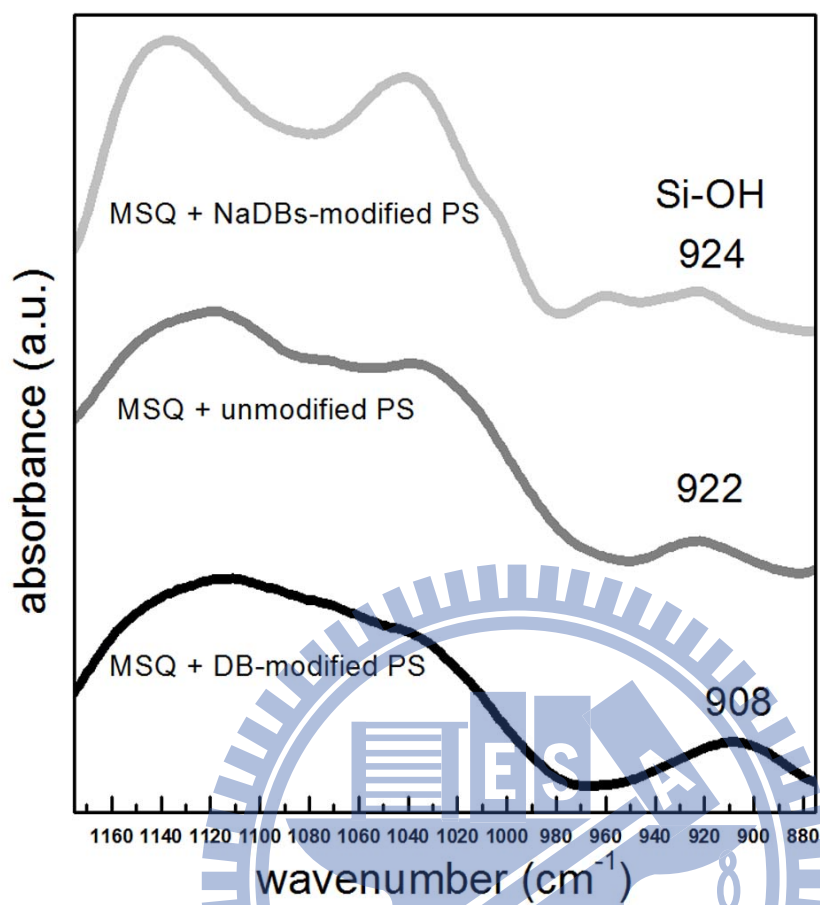


Figure 5.5 FTIR spectra (880 to 1170 cm<sup>-1</sup>) of low-*k* MSQ/PS hybrid films at 25°C for PS without modification, NaDBS-modified, and DB-modified PS.

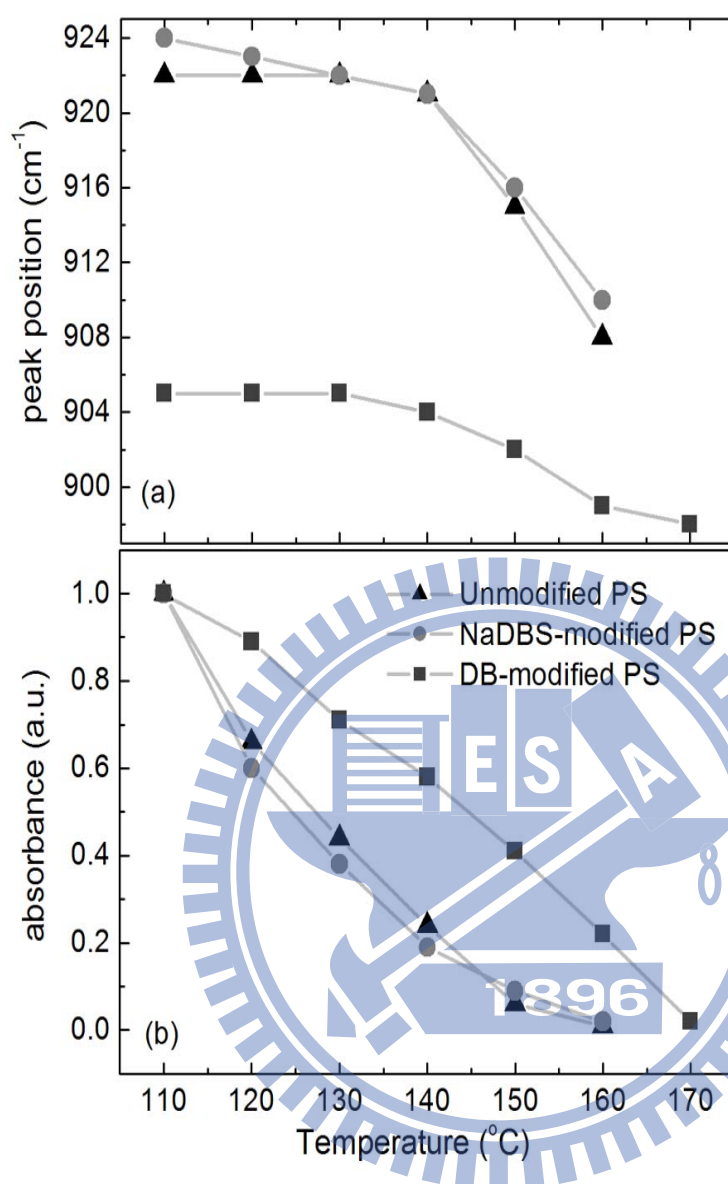


Figure 5.6 (a) Peak position and (b) peak intensity of Si-OH infrared absorption band as a function of cure temperature for NaDBS-modified PS (●), DB-modified PS (■), and PS without modification (▲).

# **Chapter 6**

## **Well-dispersed Ultra-Low- $k$ Porous Methylsilsesquioxane using a Cationic Surfactant-modified Polystyrene Porogen**

Chapter 5 indicates the surface modification method to modify and disperse the porogen in the solution and the hybrid low- $k$  film. The electrostatic dispersion controls of porogen at 10wt% in the solvent and in the hybrid film were investigated. The modified porogen can limit the size in the precursor and hybrid film. And the size did not change in the thermal removal process. This chapter focuses on increasing porogen loading (or porosity) in the low- $k$  matrix under modification of the porogen. In addition, the critical porosity with small pores and tight distribution is discussed. The cationic surfactant Domiphen bromide (DB), was used to modify the PS surface in the MSQ/PS hybrid film. And we adjust the different the porogen loading to increase the the porosity. The porosity of porous low- $k$  film will be described and elucidated by X-ray reflectivity (XRR). The pore size of the porous low- $k$  film under different porosity were characterized by 2D GISAXS and focused ion beam scanning electron microscopy (FIB-SEM). And, the dielectric constant of porous film will be described and elucidated. The mechanical strength was measured using a nanoindenter.

## 6.1 Porogen size in the precursor

Zeta potential has been recognized as a measure of the magnitude of the repulsion or attraction between PS particles in colloids. Figure 6.1 showed the initial PS is the 49.3 nm in the THF solution at pH value equal 7, and that appear the negatively surface charge -18 mV. When pH value is reduced from 7 to 5 and 3, the surface potential increased from -18 to -5.7 and +28 mV. The porogen size showed 12.3 nm at pH value of 3 and that smaller than in the pH= 7. On the other hand, the pH value from 7 to 9 and 11, the surface potential decreased from -18 to -36 and -66 mV. The porogen size at pH= 11 is also smaller than initial PS at pH= 7. Our finding on the effect of the larger absolute value of potential ( $>25$  mV) results in better colloidal stability and a smaller particle size, due to electrostatic dispersion [135]. In addition, the initial PS (pH= 7) modified by the cationic surfactant DB shows the size of 8.0 nm at surface potential +66 mV. Based on the particle size data, we will focus on the modification of PS by cationic surfactant for producing the low- $k$  MSQ/PS hybrid film and the corresponding porous low- $k$  film in this study. In order to define the property of high porosity porous low- $k$  film and further reduce the dielectric constant, the porogen loading were increased at 10, 20, 30, 40 and 50 wt%. And two kinds of porogen including unmodified and modified PS were used and discussed.

## 6.2 Porosity and pore size, shape

All hybrid low- $k$  films form the porous films after thermal process to remove porogen at 400°C. The porosity of porous film was calculated by comparing the density of porous film with a dense MSQ film (1.96 g/cm<sup>3</sup>) [156,157] by using Equation (6.1).

$$\rho = \rho_o(1 - p) \quad (6.1)$$

where  $\rho$  was experimental value of film density (g/cm<sup>3</sup>),  $\rho_o$  was silica density (1.96 g/cm<sup>3</sup>), and  $p$  referred to porosity. All of the densities were obtained from XRR experiments. Generally if the density of porous films decreased, the porosity increased. Table 6.1 summarizes the correlation between the porogen loading and porosity of the unmodified and modified condition. As the results, the porosity of porous film under the unmodified PS condition show the vol.% from 16.4, 25.6, 37.5, 46.9 to 55.8% by increasing the porogen loading (10 to 50 wt%). On the other hand, the porosity under the unmodified PS condition show the vol.% from 15.6, 27.8, 33.4, 45.3 to 53.8% by loading raised.

The next task is to clarify the pore variation under all conditions. The pore morphology and pore size of porous low- $k$  film under the different porosity without and with modification were investigated by SEM as shown in Figure 6.2(a) show the cross-section of porous film from unmodified PS at 16.4, 25.6, 37.5, 46.9 and 55.8 vol.% porosity. The results show that the pore shape was spherical at 16.4 and 25.6

vol.%, and the pore size was about 15 to 16 nm. When the porosity increased to 37.5 vol.%, the pore shape changed from sphere to worm-like (interconnected pores) and size (or length) of about 20 nm. At porosity 46.9 vol.%, the pore from the larger interconnect pore in this term obviously. Finally, a lot of worm pore appeared in the porous film and the length was  $> 20$  nm at 55.8 vol.%. Figure 6.2(b) shows the pore morphology variation for the modified PS case. The pictures show that the pore shape was spherical at 15.6, 27.8, 33.4 and 45.3 vol.% porosity. When the porosity was increased, the pore size did not grow and remained at 9-10 nm. At 56.9 vol.% porosity, the pore aggregate and pore size was about 15 nm. In particular, the picture shows that the pore size increased, but worm-like pores appeared at 56.9 vol.% porosity.

Furthermore, the pore size of the porous film with different porosity was characterized by 2D GISAXS. From GISAXS scattering patterns, the pore sizes in the porous MSQ films cured under different porosity with and without surface modification can be further determined. Figure 6.3 shows the GISAXS patterns of the different porosity low- $k$  porous films for PS porogens without and with DB surfactant modification, respectively. Figure 6.3(a) shows a weaker scattering pattern than the other one. This indicates that the pores did not disperse well in the porous low- $k$  film under the unmodified PS condition. With increasing porosity, scattering patterns illustrated in Figure 6.3(a), were confined in the low- $q$  region, indicating that the pores

tended to aggregate and start at porosity  $\geq 37.5$  vol.%. In contrast, the scattering patterns shown in Figure 6.3(b) are stronger and more uniform in the high- $q$  region than the corresponding ones (without modification) in Figure 6.3(a) until porosity was 56.9 vol.%. The results of these successive scattering patterns indicate that the pore sizes in the modified low- $k$  porous films were smaller than those in the unmodified film at specific porosity  $\leq 45.3$  vol.%. Accordingly, the scattering intensity of individual particles,  $I(q)$ , can be defined by Equation (6.2).

$$I(q) = n_p (\rho_p - \rho_m)^2 V_p^2 P(q) S(q) \quad (6.2)$$

where the wavevector  $q = 4\pi\lambda^{-1}\sin\theta$  is defined by the wavelength  $\lambda$  and the scattering angle  $2\theta$  of X-rays;  $n_p$  is the number density of particles;  $\rho_p$  and  $\rho_m$  are the scattering density of the particle and the matrix;  $V_p$  denotes the volume of particles;  $P(q)$  is a form factor, and  $S(q)$  is a structure factor. The structure factor  $S(q)$  is close to 1 in a disordered system and thus can be ignored. Therefore, the scattering profile of  $I(q)$  is only related to the form factor  $P(q)$  of the particles. As a result,  $I(q)$  can be furthered to the Guinier's expression, involving radius of gyration  $R_g$  for spherical pore as described by Eq. 2, and radius of cylinder for rod-like (worm-like) shape pore could be approximated by using Kratky-Porod approximation as by Equation (6.3) (6.4) [158].

$$I(q) \propto P(q) \propto \exp\left(\frac{-q^2 R_g^2}{3}\right) \quad (6.3)$$



$$I(q) \propto P(q) \propto \frac{1}{q} \exp\left(\frac{-q^2 R_c^2}{2}\right) \quad (6.4)$$

In the spherical case, a linear relationship exists between  $\ln(I)$  and  $q^2$ , with a slope of  $(-R_g^2/3)$ . In addition, a linear relationship exists between  $\ln(I)$  and  $q^2$ , with a slope of  $(-R_c^2/2)$  for the rod-like (worm-like) case. In order to develop more profound structural information from the scattering patterns, initial approximation was defined by using the Guinier plot ( $\ln(I)$  versus  $q_{xy}^2$ ) for spherical pores and the Kratky-Porod plot ( $\ln(I).Q$  versus  $q_{xy}^2$ ) for cylindrical pores shape. Figure 6.3 also illustrates the  $\ln(I).Q$  versus  $q_{xy}^2$  of porous low- $k$  film for both the in plane and out of plane direction. In-plane direction refers to x-y plane direction (parallel to the substrate) and out-of-plane refers to the z-direction (perpendicular to the substrate). Thus, based on Equation (6.3), the slope was directly related to the radius( $R$ ) of the pores in either the in-plane or out-of-plane direction for rod-like pores. The porous low- $k$  film from unmodified PS would be discussed for the rod-like pores shape at porosity  $\geq 37.5$  vol.%.

The pore sizes/distributions were quantitatively determined by the same method described in detail in our previous study. Accordingly, the calculated pore size and distribution of the porous low- $k$  films without and with modification, as a function of porosity are shown in Figure 6.4. For low- $k$  porous film with porogen surface modification, the average pore size/distribution increased noticeably from 9.51, 9.56, 9.75 to 10.23 nm by increasing the porosity from 15.6, 27.8, 33.4 and 45.3 vol.%. In

specific, the pore size increased slightly to 15.72 nm for a porosity of 56.9 wt%. In contrast, for the unmodified condition, the pore size was 15.8 and 16.23 nm at porosity of 16.4 and 25.6 vol.%. Because of the pore shape of 37.5, 46.9 and 55.8 vol.% porous films as shown in the SEM picture, the length of the worm-like pores will be discussed and compared to the other spherical pore condition. The pore length was 20.81 23.38 and 25.39 nm in the porosity of 37.5, 46.9 and 55.8 vol.%. Based on pore analysis of low-*k* MSQ porous films, the different PS conditions under the different loadings can be summarized as below. The unmodified PS step, when porogen loading was from 10 to 20 wt%, the pore size did not aggregate obviously. When the porogen loading was 30 wt%, the pores would change in size and shape as length of worm-like pores was about 20.81 nm. That indicates that porogen underwent a lot of aggregation during the porogen loading 20 to 30 wt%. In the literature suggests that 25 wt% loading is an ideal value of porogen addition in the hybrid low-*k* film. Above 25 wt% loading, the porogen might cause much aggregation due to the position of porogen being close to each other and forming larger mass. At 40 and 50 wt% porogen loading, the pore size (length) increased to 23.38 and 25.39 nm. In contrast, the porous film formed by modified PS, the pore size remained constant under porogen loading from 10 to 40 wt%. This indicates that the pore size did not grow obviously even when the porosity was 45.3 vol.%. The results show that the modified PS would disperse well in the hybrid low-*k*

film. When the temperature was increased, the porogen size and the later pore size and shape was also controlled even at a high porogen loading (> 25 wt %). Yet, the pore size still slightly increased at 50 wt% porogen loading. In particular, the pore size under high porosity (56.9 vol.%) was smaller than the for other condition.

### 6.3 Dielectric constant and mechanical properties

Next, the effect of porous low- $k$  film on dielectric constant and mechanical strength of porous film were showed in the Figure 6.5. The dielectric constant of the pure MSQ film was 2.78, and the  $k$  values of porous MSQ films decreased by increasing the porosity. A positive deviation of the dielectric constant by C–V measurement from the estimated value of the ideal mixing rule [ $k_{\text{porous}} = k_{\text{MSQ}} \times (1 - \text{porosity}) + k_{\text{air}} \times \text{porosity}$ ] aggravated with increasing porosity in the two kinds of porous films (without and with surface modification) as shown by Figure 6.5(a). The porous films from the modified PS showed the curve close to the ideal mixing rule, and the  $k$  value were 2.57, 2.36, 2.25, 2.12 and 1.93 by increasing the porosity from 15.6, 27.8, 33.4, 45.3 to 56.9 vol.%, respectively. Therefore, the porous films from the unmodified PS showed the  $k$  value were 2.58, 2.44, 2.18, 2.07 and 2.01 for the porosity at 16.4, 25.6, 37.5, 46.9 and 55.8 vol.%, respectively. Base on the pore size, morphology and porosity data, the  $k$  value dressers effectly by increasing porosity and  $k$  value is only related by porosity.

Figure 6.5(b) showed that the ratio of network/cage different porosity porous film with and without modification. When the porogen was adding in the hybrid film, the porogen would form a steric barrier to limit the cross-linking of matrix. In addition, the positively charge porogen attack the  $\text{OH}^-$  group would decrease the ratio of network/cage obviously. The ratio of network/cage would reduce with increasing porosity in all condition. And results indicate the ratio of network/cage in the modified case is lower than the other one. It is well knows that degree of porosity, concentration of methyl group and ratio of cross-linking impact the mechanical properties of organosilicate glasses [159,160]. Furthermore, the mechanical strength, a critical property in backend processing steps [161], of the porous low- $k$  films is discussed by nanoindenter. The incorporation of porosity into dense low- $k$  materials lowered its density, which reduced not only dielectric constant, but also mechanical properties such as elastic modulus. Figure 6.5(c) showed the moduli of the porous low- $k$  film with different loading and surface property. In this study, the MSQ without adding porogen showed the modulus on 7.8 GPa after curing at 400°C. It assumes that mechanical property of the porous film is decreased with increasing the porosity. In specific, the mechanical property of porous film is also depending on the pore size, shape, and arrangement [162,163]. In the unmodified condition, the moduli were 4.9, 3.4, 1.5, and 0.7 GPa for porosity from 16.4, 25.6, 37.5, and 46.9 vol.%, respectively. In specific, the

modulus at 55.8 vol.% of max porosity can not be measured. It expects that the lot of worm-like pore lead to the film collapse under the test. On the other hand, the moduli in the modified condition showed 5.2, 3.7, 3.0, 2.2 and 1.1 GPa for porosity at 15.6, 27.8, 33.4, 45.3 and 56.9, respectively. Figure 6.5(b) indicates that porous film with DB-modified PS showed a little lower ratio of network/cage. Yet, the mechanical strength would be effected by the pore size and shape. Thus, the worm or interconnect pore existed in the high porosity low- $k$  film during unmodified PS lead to the moduli rigid decreased. Figure 6.5(c) indicates the ideal moduli for spherical pores and discoid pores case in the different porosity [162,163,164]. The ideal E moduli and pore fraction can be defined by Equation (6.5).

$$E=E_0(1-p)^n \quad (6.5)$$

where  $E_0$  is modulus without pore,  $p$  is porosity,  $n=2$  for spherical pores,  $2<n<4$  for discoid pores. The moduli in the modified case showed a trend similar to the spherical pores. On the other hand, the unmodified case, the modulus drop at 37.5 vol.% of porosity due to the worm-like pore generate.

Finally, the maximum porogen loading was investigated in this paper. The modified porogen such as 42, 44, 46, 48, 50 wt% were prepared to form the porous low- $k$  film. Figure 6.6 shows that the GISAXS pattern varies by increasing the PS porogen loading. The result indicates that the pattern of 40 wt% PS was stronger and

more uniform in the high- $q$  region than the others. Above the 40 wt%, the scattering pattern started to approach the low- $q$  region. By increasing the porogen loading, the aggregation of porogen was slightly increased and formed the larger pores. Next, the pore size was defined by Equation (6.3) and the Gaussian distribution. The pore sizes were 11.42, 11.79, 12.03, and 13.46 nm at 42, 44, 46, and 48wt%, respectively. According to the pattern and pore size data, the maximum of porogen loading was about 48 wt%. Compared to the un-modified case, with porogen loading above 20 wt%, the pore size aggregated and the shape changed. Thus, the modification method is suitable in the high porosity porous low- $k$  film.

## 6.4 Summary

Acationic surfactant, domiphen bromide (DB), was used to modify the PS surface and effectively disperse the PS in the MSQ/PS hybrid film. Porosity of the porous film is increased by adjusting the porogen loading from 10, 20, 30, 40 to 50 wt%. For the unmodified condition, the pore size were spherical and about 16 nm in the low porosity ( $\sim 26$  vol%). When the porosity was above 37.5 vol%, the pores changed from sphere to worm-like or interconnected pore and the pore length was 21.2 to 26.3 nm. In contract, with porous films prepared from modified PS, the pore size remained at 9~10 nm even when the porosity increased from 15.6 to 46 vol%. All dielectric constant would was

from 2.6 to 1.9 by increasing the porosity of the porous films with and without surface modification. Because of the  $k$  value is only related by porosity. The DB-modified PS slightly reduces the degree of cross-linking of MSQ due to the charged PS surface effect the condensation of Si-OH. In summary, the surface modification method could disperse the porogen in the hybrid system due to the electrostatic force and the electroviscous effect with the matrix. In particular, the surface modification could be employed effectively at high porosity above 26 wt% of porogen loading. Porous film with small pore and tight distribution from maximum porogen loading at 46 wt% is suggested.

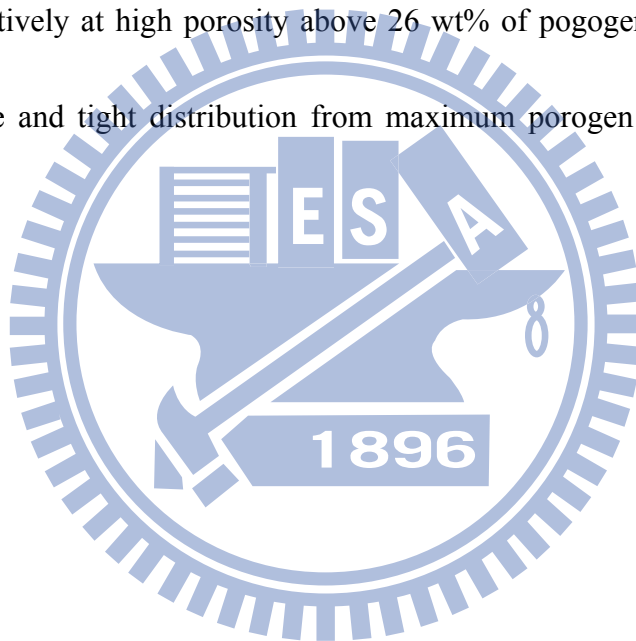


Table 6.1 Density and porosity of low-*k* films by using XRR

loading (wt%)	Unmodified condition		Modified condition	
	Density (g/cm <sup>3</sup> )	Porosity (%)	Density (g/cm <sup>3</sup> )	Porosity (%)
10	1.63	16.4	1.65	15.6
20	1.46	25.6	1.42	27.8
30	1.23	37.5	1.30	33.4
40	1.04	46.9	1.07	45.3
50	0.84	55.8	0.91	56.9





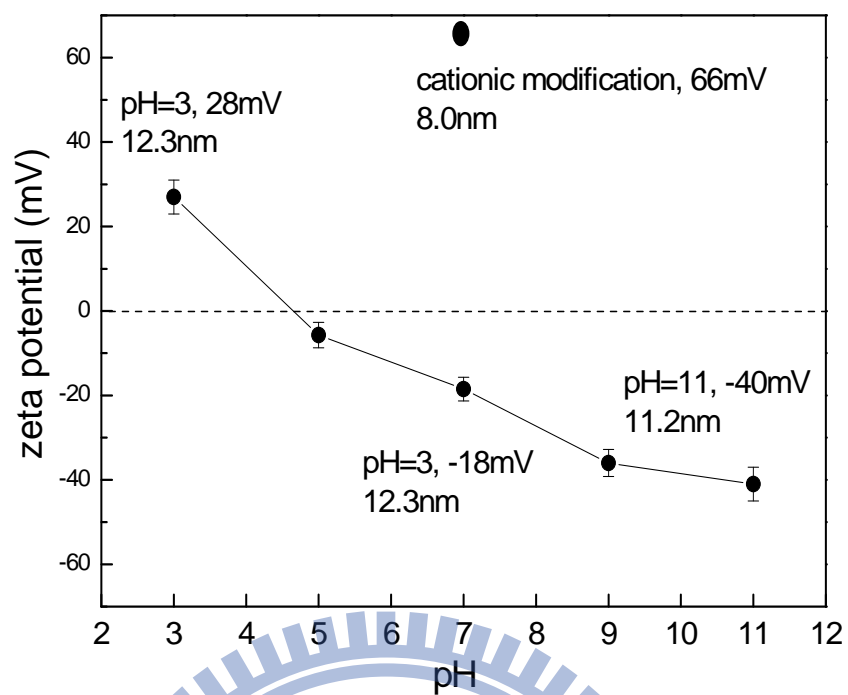


Figure 6.1 The size and surface potential of PS porogen under different pH value and surface modification by DB.

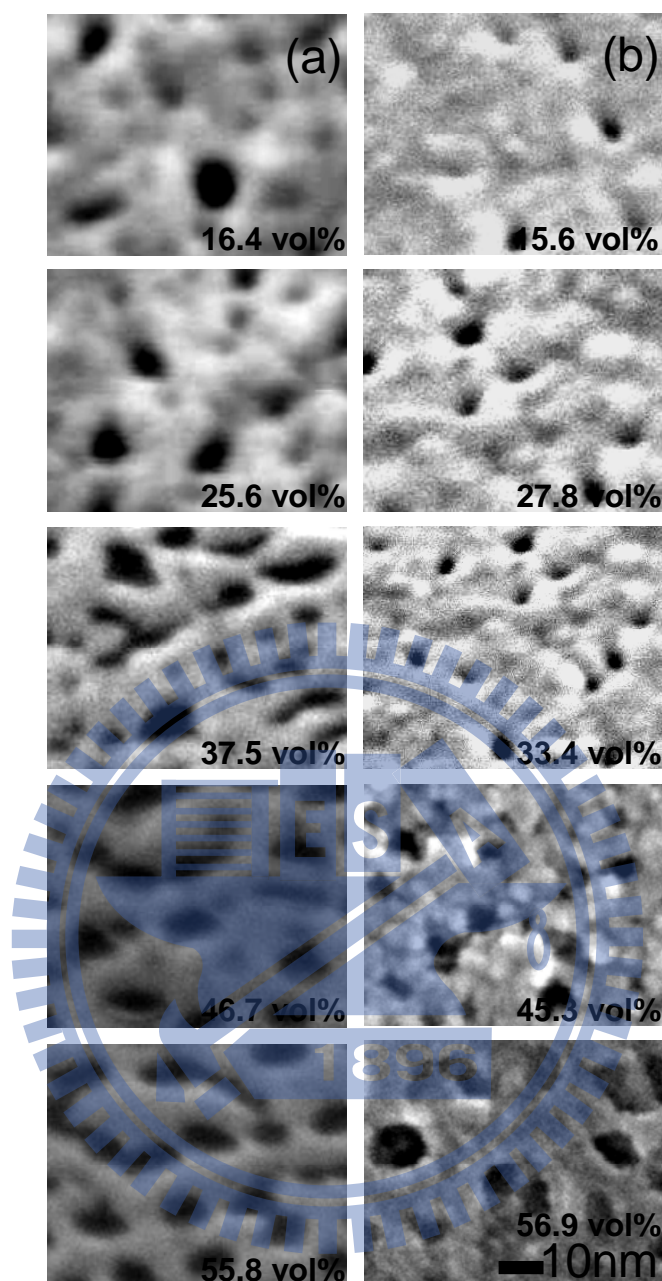


Figure 6.2 Morphology of the low- $k$  porous films with different porosity as a function of: (a) no modification, (b) modification by DB.

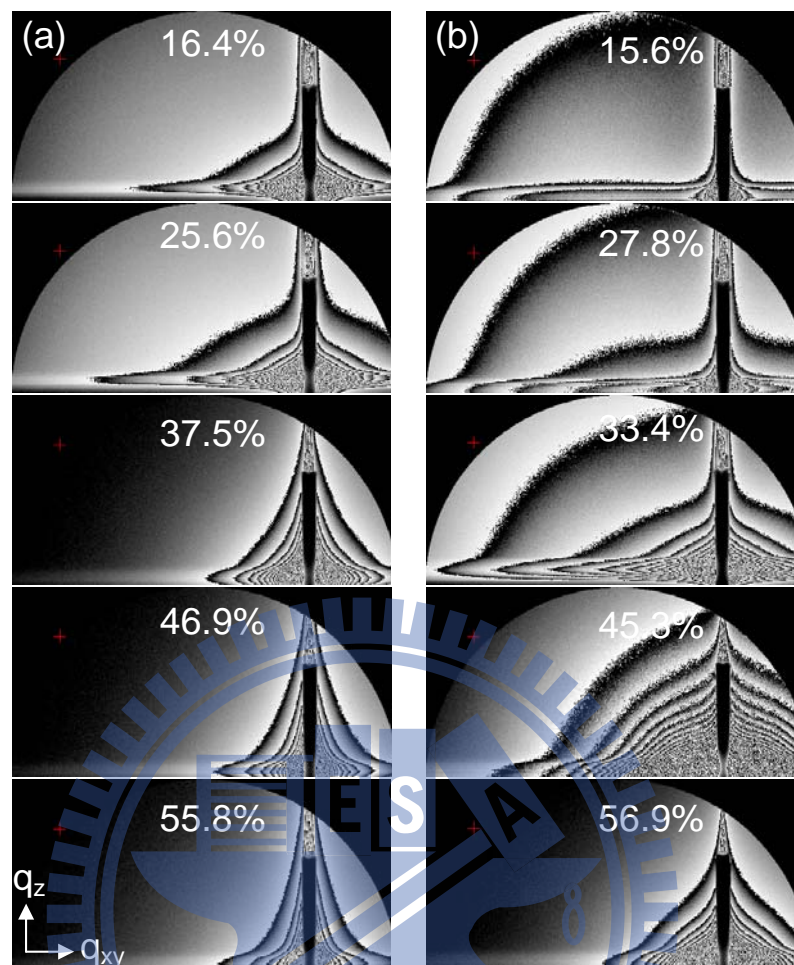


Figure 6.3 2-D GISAXS scattering patterns of the low- $k$  porous films with the different porosity under porogen as a function of : (a) no modification, (b) modification by DB.

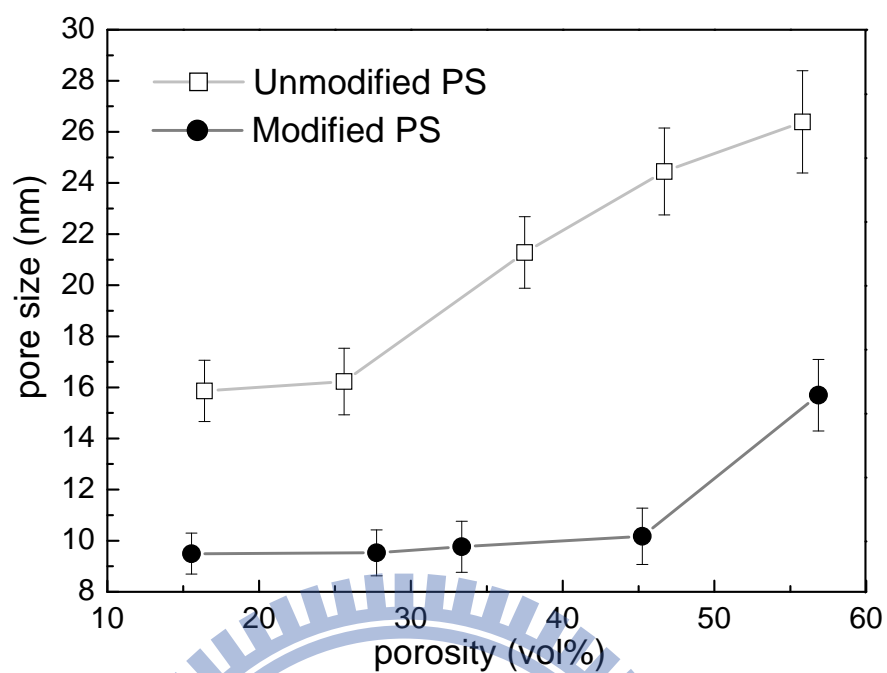


Figure 6.4 Pore size and distribution in the low- $k$  porous films with different porosity as a function of: (a) no modification, (b) modification by DB.

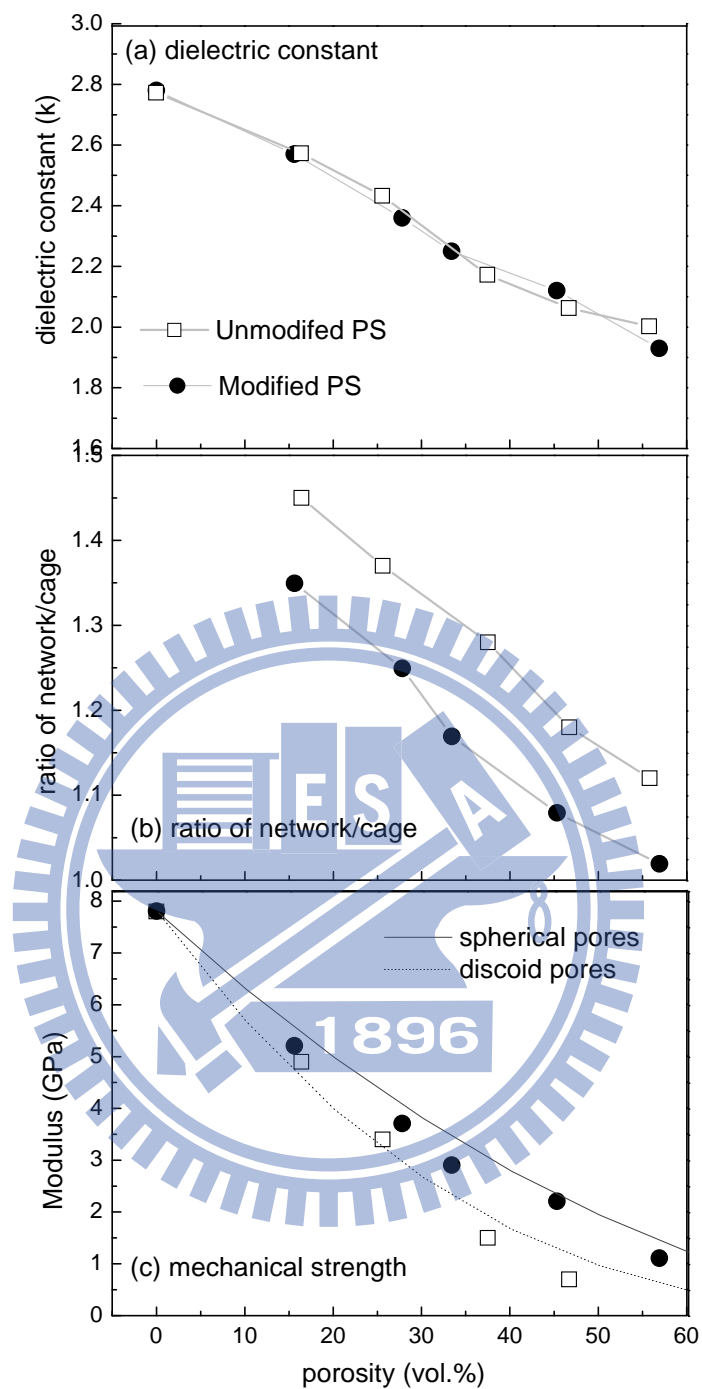


Figure 6.5 The (a) dielectric constant, (b) ratio of network/cage and (c) mechanical strength of porous low- $k$  film with and without modification under different porosity.



Figure 6.6 2-D GISAXS scattering patterns of the low- $k$  porous films under modification with the different porogen loading.

# Chapter 7

## Conclusions

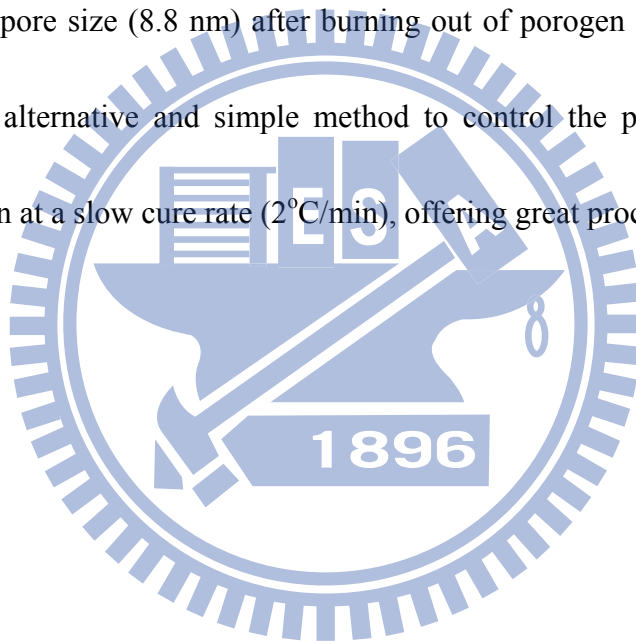
A commercial, spin-on organosilicate, *i.e.* methylsilsesquioxane (MSQ) was selected as the low- $k$  matrix and a high-temperature porogen such as SBS, was employed as the sacrificial component in this paper. The effect of the MSQ structures under different thermal cure profiles (slow: 2°C/min *vs.* rapid: 200°C/min) on the porogen aggregation behavior and its size in the hybrid MSQ/SBS films cured up to 200°C were investigated by *in-situ* GISAXS, viscosity measurement, and FT-IR analysis. For slow curing, significant porogen diffusion and aggregation occurred between 100 to 200°C, at which the porogen size increased from 12 nm to 34 nm. The aggregation of SBS in the hybrid MSQ/SBS films were greatly influenced by the structural state of MSQ matrix at three controlling temperatures; namely (1) glass transition temperature,  $T_g$  (100°C), (2) onset temperature (160°C) for transforming Si-O cage Si-O to network Si-O structure, and (3) immobilization temperature (170°C). Porogen size started growing as SBS porogen aggregated at  $T > T_g$  of MSQ, then increased at a higher rate at  $T > 160^\circ\text{C}$  as viscosity drastically dropped down to ~130,000 poise due to the plasticization of vast amount of H<sub>2</sub>O released by the condensation reaction involving the transformation of cage Si-O to network Si-O structure, and finally remained about constant at ~32 nm after 170°C, at which MSQ matrix was highly cross-linked to

immobilize SBS particles. In contrast, upon rapid curing, the SBS porogen was trapped within a rapidly formed, well-crosslinked MSQ matrix, leaving its size unchanged at approximately 12 nm with tight distribution.

Next, we replace a lower Mw polymer PS as high temoerature. The effect of surfactant modification of PS on the porogen size in low- $k$  MSQ/PS hybrid films at 10wt% PS loading under a slow curing profile was studied by GISAXS, viscosity measurement, and Fourier transform infrared analysis. Specifically, an anionic surfactant, NaDBS, and a cationic surfactant, DB, were used to modify the surface potential of PS porogen in THF solution from an initial value of -18 mV (unmodified) to -58mV and +66mV, respectively. Upon curing at a slow rate (2°C/min), the porogen without modification aggregates and its size increases from 10.0 to 16.5 nm at different rates due to the steric hindrance of the structural state of the MSQ matrix at three particular temperatures. The porogen size starts to increase as PS porogen aggregates, at  $T > T_g$  of MSQ, then increases at a higher rate, at  $T$  between 150 and 175°C, where the viscosity drops drastically at  $T > 160^\circ\text{C}$ , and finally increases to 16.5 nm after 190°C. In contrast, for the NaDBS-modified and DB-modified PS systems, the high zeta potential of charged PS porogens impede the aggregation of PS within a successively cross-linked MSQ matrix through electrostatic repulsion forces and the electroviscous effect. This results in little or limited PS porogen aggregation and yields a small



porogen size with tight distribution,  $11.1 \pm 2.4$  and  $8.7 \pm 2.0$  nm, respectively. More importantly, the columbic attraction between the Si-OH groups of MSQ matrix and the DB-modified, positively charged PS particles, restrains the PS porogen and its mobility during the cure step, resulting in a further reduction in porogen aggregation. Overall, the NaDBS modified-PS/MSQ hybrid film yields a small porogen size and tight distribution ( $8.7 \pm 2$  nm) when cured at a slow rate up to 200°C with MSQ fully cross-linked, and a similarly small pore size (8.8 nm) after burning out of porogen at 400°C. In summary, we provide an alternative and simple method to control the porogen, pore size and distribution even at a slow cure rate (2°C/min), offering great process latitude.



## References

---

- 1 M. T. Bohr, *Solid State Technol.*, **9**, 105 (1996).
- 2 P. S. Ho, J. Leu, and W. W. Lee, *Low Dielectric Constant Materials for IC Applications*, Springer, New York (2002).
- 3 D. Edelstein, J. Heidenreich, R. Goldblatt, W. Cote, C. Uzoh, N. Lustig, P. Roper, T. McDevitt, W. Motsiff, A. Simon, J. Dukovic, R. Wachnik, H. Rathore, R. Schulz, L. Su, S. Luce, J. Slattery, *Proc. Int. 1998 Electron Devices Meeting, Technical Digest*, IEEE Press, 773 (1997).
- 4 P. W. Lee, S. Mizuno, A. Verma, H. Tran, and B. Nguyen, *J. Electrochem. Soc.*, **143**, 2015 (1996).
- 5 S. J. Martin, J. P. Godschalx, M. E. Mills, E. O. Shaffer II, and P. H. Townsend, *Adv. Mater.*, **12**, 1769 (2000).
- 6 J. L. Hedrick, R. D. Miller, C. J. Hawker, K. R. Carter, W. Volksen, D. Y. Yoon, and M. Trollsas, *Adv. Mater.*, **10**, 1049 (1998).
- 7 T. J. Shin, and M. Ree, *Macromol. Chem. Phys.*, **203**, 791 (2002).
- 8 M. Fayolle, G. Passemard, O. Louveau, F. Fusalba, and J. Cluzel, *Microelectron. Eng.*, **70**, 255 (2003).
- 9 *International Technology Roadmap for Semiconductor*, Overview, 2010 Update, Semiconductor International Association (2010).
- 10 M. Ree, J. Yoon, and K. Heo, *J. Mater. Chem.*, **16**, 685 (2005).

- 
- 11 J. N. Sun, Y. Hu, W. E. Frieze, W. Chen, and D. W. Gidley, *J. Electrochem. Soc.*, **150**, F97 (2003).
- 12 T. Frot, W. Volksen, T. Magbitang, D. Miller, S. Purushothaman, M. Lofaro, R. Bruce, and G. Dubois, *Interconnect Technology Conference and 2011 Materials for Advanced Metallization (IITC/MAM), IEEE International*, p.1 (2011).
- 13 H. Shi, H. Huang, J. Bao, J. Im, P. S. Ho, Y. Zhou, J. T. Pender, M. Armacost, and D. Kyser, *Conference Proceedings of the IEEE International Interconnect Technology (IITC)*, p.78 (2009).
- 14 J. Calvert and M. Gallagher, *Semicond. Int.*, **26**, 56 (2003).
- 15 S. Malhouitre, C. Jehoul, J.V. Aelst, H. Struyf, S. Brongersma, L. Carbonell, I. Vos, G. Beyer, M.V. Hove, D. Gronbeck, M. Gallagher, J. Calvert, and K. Maex, *Microelectron. Eng.*, **70**, 302 (2003).
- 16 M.-L. Che, C.-Y. Huang, S. Choang, Y.-H. Chen, and J. Leu, *J. Mater. Res.*, **25**, 1049 (2010).
- 17 G. E. Moore, *Electronics*, **38**, 8 (1965).
- 18 J. Singh, *Semiconductor Devices: Basic Principles*, Chapter 10, John Wiley & Sons, New York (2001).
- 19 *International Technology Roadmap for Semiconductor*, Executive Summary, 2009 Edition, Semiconductor International Association (2009).
- 20 P. T. Liu, T. C. Chang, Y. L. Yang, Y. F. Cheng and S. M. Sze, *IEEE Trans. On Electronic Devices*, **47**, 1733 (2000).
- 21 *National Technology Roadmap for Semiconductors*, 1997 Edition, Semiconductor

- 
- Industry Association (1997).
- 22 R. D. Goldblatt, *Proc. of Int'l Interconnect Technology Conference*, **263**, 261 (2000).
- 23 C. Case, *Interconnect Working Group*, ITRS 2010 summer conference, 14th July, San Francisco (2010).
- 24 N. Nakamura, N. Matsunaga, T. Kaminatsui, K. Watanabe, and H. Shibata, *Proc. Int. 2008 Interconnect Technology Conf.*, IEEE Press, 193 (2008).
- 25 N. Patil, D. Jie, S. Mitra, and H. S. P. Wong, *Nanotechnology*, **8**, 37 (2009).
- 26 A. Naeemi, and J. D. Meindl, *Electron Device Letters*, IEEE press, **29**, 497 (2008).
- 27 V. L. Shannon, M. Z. Karim, *Thin Solid Films*, **270**, 498 (1995).
- 28 M. J. Shapiro, S. V. Nguyen, T. Matsuda, D. Dobuzinsky, *Thin Solid Films*, **270**, 503 (1995).
- 29 C. C. Chang, S. K. J. Jian, and J. S. Chen, *J. Electrochem. Soc.*, **153**, G901 (2006).
- 30 M. J. Loboda, *Microelectron. Eng.*, **50**, 15 (2000).
- 31 H. G. P. Lewis, D. J. Edell, and K. Gleason, *Chem. Mater.*, **12**, 3488 (2000).
- 32 Q. Wu and K. Gleason, *J. Vac. Sci. Technol. A*, **21**, 388 (2003).
- 33 A. Grill, *Thin Solid Films*, **398-399**, 527 (2001).
- 34 A. Grill and V. Patel, *Appl. Phys. Lett.*, **79**, 803 (2001).
- 35 C. C. Chiang, M. C. Chen, L. J. Li, Z. C. Wu, S. M. Jang, and M. S. Liang, *J. Electrochem. Soc.*, **151**, G612 (2004).
- 36 M. L. O'Neill, R. N. Vrtis, J. L. Vincent, A. S. Lukas, E. J. Karawacki, B. K.

- 
- Peterson, and M. D. Bitner, *Mater. Res. Soc. Symp. Proc.*, **766**, E8.17.1 (2003).
- 37 S. J. Martin, J. P. Godschalx, M. E. Mills, E. O. Shaffer II, and P. H. Townsend, *Adv. Mater.*, **12**, 1769 (2000).
- 38 M. Fayolle, G. Passemard, M. Assous, D. Louis, A. Beverina, Y. Gobil, J. Cluzel and L. Arnaud, *Microelectron. Eng.*, **60**, 119 (2002).
- 39 R. H. Baney, M. Itoh, A. Sakakibara, and T. Suzukit, *Chem. Rev.*, **95**, 1409 (1995).
- 40 P. T. Liu, T. C. Chang, Y. S. Mor, and S. M. Sze, *Jpn. J. Appl. Phys.*, **38**, 3482 (1999).
- 41 H. C. Liou, and J. Pretzer, *Thin Solid Films*, **335**, 186 (1998).
- 42 H. C. Liou, and J. Pretzer, *Mater. Res. Soc. Symp. Proc.*, **565**, 239 (1999).
- 43 J. Bremmer, Y. Liu, K. Gruszynski, and F. Dall, *Mater. Res. Soc. Symp. Proc.*, **37**, 476 (1997).
- 44 Y. Liu, J. Bremmer, K. Gruszynski, and F. Dall, *VLSI Multilevel Interconnection Conf.*, 655, Santa Clara, CA, (1997).
- 45 L. W. Hrubesh, L. E. Keene, and V. R. Latorre, *J. Mater. Res.*, **8**, 1736 (1993).
- 46 D. H. Evertt, *Pure Appl. Chem.*, **31**, 579 (1972).
- 47 T. Ramos, S. Wallace, and D. M. Smith, *Mat. Res. Soc. Symp. Proc.*, **495**, 279 (1998).
- 48 C. M. Flannery, C. Murray, I. Streiter and S. E. Schulz, *Thin Solid Films*, **388**, 1 (2001).

- 
- 49 A. Jain, S. Rogojevic, S. V. Nitta, V. Pisupatti, W. N. Gill, P. C. Wayner, J. L. Jr., T. E. F. M. Plawsky, G. S. Standaert, *Mat. Res. Soc. Symp. Proc.*, **565**, 29 (1999)
- 50 T. Ramos, K. Roderick, A. Mascara, and D. M. Smith, “Processings of Advanced Metallization Conferences (AMC), Advanced Metallization and Interconnect Systems for ULSI Applications, 445 (1996).
- 51 C. Jin, J. D. Luttmer, D. M. Smith, and T. A. Ramos, *MRS Bull.* **22**, 39 (1997).
- 52 K. Chung, E. S. Moyer, and M. Spaulding, U.S. Patent No. 6,231,989 (2001).
- 53 E. S. Moyer, K. Chung, M. Spaulding, T. Deis, R. Boisvert, C. Saha, and J. Bremmer, *Proceedings of IITC*, 1999.
- 54 Z. Li, M. C. Johnson, M. Sun, E. T. Ryan, D. J. Earl, W. Maichen, J. I. Martin, S. Li, C. M. Lew, J. Wang, M. W. Deem, M. E. Davis, and Y. Yan, *Angew. Chem.-Int. Edit.*, **118**, 6477 (2006).
- 55 Z. Li, S. Li, H. Luo, and Y. Yan, *Adv. Funct. Mater.*, **14**, 1019 (2004).
- 56 S. Eslava, C. E. A. Kirschhock, S. Aldea, M. R. Baklanov, F. Iacopi, K. Maex, and J. A. Martens, *Microporous Mesoporous Mat.*, **118**, 458 (2009).
- 57 S. Eslava, F. Iacopi, M. R. Baklanov, C. E. A. Kirschhock, K. Maex, and J. A. Martens, *J. Am. Chem. Soc.*, **129**, 9288 (2007).
- 58 S. Eslava, S. Delahaye, M. R. Baklanov, F. Iacopi, C. E. A. Kirschhock, K. Maex, and J. A. Martens, *Langmuir*, **24**, 4894 (2008).

- 
- 59 C. M. Lew, Z. Li, S. Li, S. Hwang, Y. Liu, D. I. Medina, M. Sun, J. Wang, M. E. Davis, and Y. Yan, *Adv. Funct. Mater.*, **18**, 3454 (2008).
- 60 C. M. Lew, Y. Liu, B. Day, G. M. Kloster, H. Tiznado, M. Sun, F. Zaera, J. Wang, and Y. Yan, *Langmuir*, **25**, 5039 (2009).
- 61 S. Li, Z. Li, D. Medina, C. Lew, and Y. Yan, *Chem. Mater.*, **17**, 1851 (2005).
- 62 S. Eslava, J. Urrutia, A. N. Busawon, M. R. Baklanov, F. Iacopi, S. Aldea, K. Maex, J. A. Martens, and C. E. A. Kirschhock, *J. Am. Chem. Soc.*, **130**, 17528 (2008).
- 63 Z. Li, M. C. Johnson, M. Sun, E. T. Ryan, D. J. Earl, W. Maichen, J. I. Martin, S. Li, C. M. Lew, J. Wang, M. W. Deem, M. E. Davis and Y. Yan, *Angew. Chem.*, **118**, 6477 (2006).
- 64 J. L. Hendrick, R. D. Miller, C. J. Hawker, K. R. Carter, W. Volksen, D. Y. Yoon, and M. Trollsas, *Adv. Mater.*, **10**, 1049 (1998).
- 65 M. Gallagher, N. Pugliano, J. Calvert, Y. You, R. Gore, N. Annan, M. Talley, S. Ibbitson, and A. Lamola, Presented at the MRS Spring Meeting, 2001.
- 66 M. L. Che, J. Leu, Y. H. Chen, C. Y. Huang, and S. Choang, *ECS Trans.*, **6**, 591 (2007).
- 67 Y. F. Lu, G. Z. Cao, R. P. Kale, S. Prabakar, G. P. Lopez, and C. J. Brinker, *Chem. Mater.*, **11**, 1223 (1999).
- 68 M. R. Baklanov *et al.*, *Proceedings of the Advanced Metallization Conference* Materials Research Society, Pittsburgh, PA, (2002).

- 
- 69 M. Petkov, M. H. Weber, K. G. Lynn, and K. P. Rodbell, *Appl. Phys. Lett.*, **79**, 3884 (2001).
- 70 F. Iacopi, C. Zistlc, C. Jehould, Zs. Tokeia, Q.T. Le, A. Das, C. Sullivand, G. Prokopowicz , D. Gronbeck, M. Gallagher, J. Calvert, and K. Maex, *Microelectron. Eng.*, **64**, 351 (2002).
- 71 S. Yang, P. A. Mirau, C. S. Pai, O. Nalamasu, E. Reichmanis, E. K. Lin, H. J. Lee, D. W. Gidley, and J. Sun, *Chem. Mater.*, **13**, 2762 (2001).
- 72 E. M. Freer, L. E. Krupp, W. D. Hisberg, P. M. Rice, J. L. Hendrik, J. N. Cha, R D. Miller, and H. C. Kim, *Nano Lett.*, **5**, 2014 (2005).
- 73 C. C. Yang, P. T. Wu, W. C. Chen, and H. L. Chen, *Polymer*, **45**, 5691 (2004)
- 74 E. Huang, M. F. Toney, W. Volksen, D. Mecerreyes, P. Brock, H.-C. Kim, C. J. Hawker, J. L. Hedrick, V. Y. Lee, T. Magbitang, R. D. Miller and L. B. Lurio, *Appl. Phys. Lett.*, **81**, 2232 (2002).
- 75 H.-C. Kim, W. Volksen, R. D. Miller, E. Huang, G. Yang, R. M. Briber, K. Shin and S. K. Satija, *Chem. Mater.*, **15**, 609 (2003).
- 76 S. C. Zimmerman, M. S. Wendland, N. A. Rakow, I. Zharov and K. S. Suslick, *Nature*, **418**, 399 (2002).
- 77 M. Jikei and M.-A. Kakimoto, *J. Polym. Sci., Part A: Polym. Chem.*, **42**, 1293 (2004).
- 78 B. Lee, Y.-H. Park, Y.-T. Hwang, W. Oh, J. Yoon and M. Ree, *Nat. Mater.*, **4**, 147 (2005).
- 79 C. V. Nguyen, K. R. Carter, C. J. Hawker, J. L. Hedrick, R. L. Jaffe, R. D. Miller, J.



- 
- F. Remenar, H. W. Rhee, P. M. Rice, M. F. Toney, M. Trollsas, and D. Y. Yoon, *Chem. Mater.*, **11**, 3080 (1999).
- 80 Y. Toivola, S. Kim, R. F. Cook, K. Char, J. K. Lee, D. Y. Yoon, H. W. Rhee, S. Y. Kim, and M. Y. Jin, *J. Electrochem. So.*, **151**, F45 (2004).
- 81 B. Lee, Y. H. Park, Y. T. Hwang, W. Oh, J. Yoon, and M. Ree, *Nature Materials*, **4**, 147 (2005).
- 82 A. Heise, C. V. Nguyen, R. Malek, J. L. Hedrick, C. W. Frank and R. D. Miller, *Macromolecules*, **33**, 2346 (2000).
- 83 J. H. Yim, M. R. Baklanov, D. W. Gidley, H. G. Peng, H. D. Jeong, and L. S. Pu, *J. Phys. Chem. B*, **108**, 8953 (2004).
- 84 J. H. Yim, J. B. Seon, T. D. Jeong, L. Y. S. Pu, M. R. Baklanov, and D. W. Gidley, *Adv. Funct. Mater.*, **14**, 277 (2004).
- 85 A. Zenasni, F. Ciaramella, V. Jousseume, C. L. Cornec, and G. Passemard, *J. Electrochem. Soc.*, **154**, G6 (2007).
- 86 W. Oh, T. J. Shin, M. Ree, M.Y. Jin, and K. Char, *Mol. Cryst. And Liq. Cryst.*, **371**, 397 (2001).
- 87 J. Hang, L. Shi, X. Feng, and L. Xiao, *Powder Technol.*, **192**, 166 (2009).
- 88 B.V Derjaguin, S.S Dukhin, and A.E Yaroshchuk, *J. Colloid Interface Sci.*, **115**, 234 (1987).
- 89 F. Zhang, L. Cao, and W. Yang, *Macromol. Chem. Phys.*, **211**, 744 (2010).
- 90 D. Heath and T. F. Tadros, *Faraday Discuss. Chem. Soc.*, **76**, 203 (1983).
- 91 A. B. Jódar-Reyes, J. L. Vinuesa, and A. Martín-Rodríguez, *J. Colloid Interface Sci.*,

- 
- 297**, 170 (2006).
- 92 C. Nguyen, C. J. Hawker, R. D. Miller, E. Huang, and J. L. Hedrick, *Macromolecules*, **33**, 4281 (2000).
- 93 H. W. Ro, K. J. Kim, P. Theato, D. W. Gidley, and D. Y. Yoon, *Macromolecules*, **38**, 1031 (2005).
- 94 A. Heise, C. Nguyen, R. Malek, J. L. Hedrick, C. W. Frank, and R. D. Miller, *Macromolecules*, **33**, 2346 (2000).
- 95 W. Oh, Y. Hwang, Y. H. Park, M. Ree, S.-H. Chu, K. Char, J.K. Lee, and S.Y. Kim, *Polymer*, **44**, 2519 (2003).
- 96 K. Mosig, T. Jacobs, K. Brennan, M. Rasco, J. Wolfe, and R. Augur, *Microelectron. Eng.*, **64**, 11 (2002).
- 97 E. T. Ryan, J. Martin, K. Junker, J. Wetzel, J. W. Sun, and D. W. Gidley, *J. Mat. Res.*, **16**, 3335 (2001).
- 98 G. Ouyang, G Yang, C. Sun, and W. Zhu, *Small*, **4**, 1359 (2008).
- 99 P. A. Hartley and G. D. Prafitt, American Institute of Chemical Engineers Symposium Series, 69, 433 (1983).
- 100 P. A. Hartley and G. D. Prafitt, *Langmuir*, **1**, 651 (1985).
- 101 G. D. Prafitt, *J. Br. Ceram. Soc.*, **13**, 13 (1969).
- 102 K. Mosig, T. Jacobs, K. Brennan, M. Rasco, J. Wolf, and R. Augur, *Microelectron. Eng.*, **64**, 11 (2002).
- 103 M. P. Petkov, M. H. Weber, K. G. Lynn, and K. P. Rodbell, *Appl. Phys. Lett.*, **79**, 3884 (2001).
- 104 S. Chikaki, K. Kinoshita, K. Kohmura, H. Tanaka, E. Soda, T. Suzuki, Y. Seino, N. Hata, S. Satio, and T. Kikkawa, *J. Electrochem. Soc.*, **157**, H519 (2010).

- 
- 105 S. Yang, P. A. Mirau, C.-S. Pai, O. Nalamasu, E. Reichmanis, J. C. Pai, Y. S. Obeng, J. Seputro, E. K. Lin, H.-J. Lee, J. Sun, and D. W. Gidley, *Chem. Mater.*, **14**, 369 (2002).
- 106 J. Hyeon-Lee, Y. Y. Lyu, M. S. Lee, J.-H. Hahn, J. H. Rhee, S. K. Mah, J.-H. Yim, and S. Y. Kim, *Macromol. Mater. Eng.*, **289**, 164 (2004).
- 107 K. H. Lee, J.-H. Yim, and M. R. Baklanov, *Microporous Mesoporous Mat.*, **94**, 113 (2006).
- 108 H.C. Kim, J. B. Wilds, C. R. Kreller, W. Volksen. P. J. Brock, V. Y. Lee, T. Magbitang, J. L. Hedrick, C. J. Hawker, and R. D. Miller, *Adv. Mater.*, **14**, 1637 (2002).
- 109 A. M. Padovani, L. Rhodes, S. A. B. Allen, and P. A. Kohl, *J. Electrochem. Soc.*, **149**, F161 (2002).
- 110 Y. Chang, C.-Y. Chen, and W.-C. Chen, *J. Polym. Sci., Part B: Polym. Phys.*, **42**, 4466 (2004).
- 111 H.-J. Lee, C. L. Soles, B. D. Vogt, D.-W. Liu, W.-I. Wu, E. K. Lin, H.-. Kim, V. Y. Lee, W. Volksen, and R. D. Miller, *Chem. Mater.*, **20**, 7390 (2008).
- 112 S. Malhouitre, C. Jehoul, J. V. Aelst, H. Struyf, S. Brongersma, L. Carbonell, I. Vos, G. Beyer, M. V. Hove, D. Gronbeck, M. Gallagher, J. Calvert, and K. Maex, *Microelectron. Eng.*, **70**, 302 (2003).
- 113 M. Fayolle, V. Jousseume, M. Assous, E. Tabouret, C. le Cornec, P. H. Haumesser, P. Leduc, H. Feldis, O. Louveau, G. Passemar, and F. Fusalba, *Proc. Int. 2004 Interconnect Technology Conf.*, IEEE Press, 208 (2004).

- 
- 114 S. P. Murarka, M. Eizenberg, and A. K. Sinha, *Interlayer Dielectrics for Semiconductor Technologies*, Elsevier/Academic Press, San Diego, CA (2003).
- 115 R. J. O. M. Hoofman, V. H. Nguyen, V. Arnal, M. Broekaart, L. G. Gosset, W. F. A. Besling, M. Fayolle, F. Lacopi, In: M. Baklanov, M. Green, and K. Maex (Eds.), *Dielectric Films for Advanced Microelectronics*, p.214, John Wiley & Sons, New York (2007).
- 116 A. Gawase, S. Chikaki, N. Nakamura, E. Soda, N. Oda, and S. Saito, *Jpn. J. Appl. Phys.*, **49**, 05FD02 (2010).
- 117 M. Koderu, T. Takahashi, and G. Mimamihaba, *Jpn. J. Appl. Phys.*, **49**, 04DB07 (2010).
- 118 H. Lai, Y. S. Sun, U. Jeng, J. M. Lin, T. L. Lin, H. S. Sheu, W. T. Chuang, Y.S. Huang, C. H. Hsu, M. T. Lee, H. Y. Lee, K. S. Liang, A. Gabriel, and M. H. J. Koch, *J. Appl. Crystallogr.*, **39**, 871 (2006).
- 119 R. J. Roe, *Methods of X-Ray and Neutron Scattering in Polymer Science*, Chapter 5, Oxford University Press, New York (2000).
- 120 J.-F. Lee, M.-H. Hsu, H.-P. Chao, H.-C. Huang, and S.-P. Wang, *J. Hazard. Mater.*, **114**, 123 (2004).
- 121 A. van der Lee, F. Salah, and B. Harzallah, *J. Appl. Cryst.*, **40**, 820 (2007).
- 122 J. R. Levine, J. B. Cohen, Y. W. Chung and P. Georgopoulos, *J. Appl. Cryst.*, **22**, 528 (1989).
- 123 A. Guinier, *Ann. Phys.*, **12**, 161 (1939).

- 
- 124 D. J. Kinning and E. L. Thomas, *Macromolecules*, **17**, 1712 (1984).
- 125 J. S. Pedersen, *J. Appl. Crystallogr.*, **27**, 595 (1994).
- 126 L. A. Feigin and D. I. Svergun, *Structure Analysis by Small Angle X-ray and Neutron Scattering*, Plenum, New York (1987).
- 127 A. Guinier and G. Fournet, *Small-Angle Scattering of X-rays*, John Wiley, New York (1955).
- 128 J. Fuwukawa, *Polym. Bull.*, **10**, 336 (1983).
- 129 Q. R. Huang, H.-C. Kim, E. Huang, D. Mecerreyes, J. L. Hedrick, W. Volksen, C. W. Frank, and R. D. Miller, *Macromolecules*, **36**, 7661 (2003).
- 130 R. J. Young and P. A. Lovell, *Introduction to Polymers*, Chapman & Hall, London (1991).
- 131 H. W. Ro, E. S. Park, C. L. Soles, and D. Y. Yoon, *Chem. Mater.*, **22**, 1330 (2010).
- 132 C. Y. Wang, Z. X. Shen, and J. Z. Zheng, *Appl. Spectrosc.*, **54**, 209 (2000).
- 133 N. Wiener, *J. Math. Phys.*, **2**, 131 (1923).
- 134 H. T. Healy and Y. C. Zhang, *Phys. Rep.*, **254**, 215 (1995).
- 135 T. Cosgrove, *Colloid Science: Principles, Methods and Applications*, John Wiley & Sons, New York, 2010.
- 136 A. Drechsler and K. Grundke, *Colloids and Surfaces. A*, **264**, 157 (2005).
- 137 P. F. Luckham, *Adv. Colloid Interface Sci.*, **111**, 29 (2004).
- 138 W. Li, P. Chen, M. Gu, and Y. Jin, *J. Eur. Ceram. Soc.*, **24**, 3679 (2004).
- 139 W. C. Liu, C. C. Yang, W. C. Chen, B. T. Dai, and M. S. Tsai, *J. Non-Cryst. Solids.*, **311**, 233 (2002).
- 140 B. Xie and A. J. Muscat, *Microelectron. Eng.*, **76**, 52 (2004).
- 141 C. D. Volpe, S. Dirè, and E. Pagani, *J. Non-cryst. Solids.*, **209**, 51 (1997).
- 142 M. A. M. Khraisheh, M. A. Al-Ghouti, S. J. Allen, and M. N. Ahmad, *Water Res.*,

- 
- 39**, 922 (2005).
- 143 P. F. Mcmillan and R. L. Remmele Jr., *Am. Mineral.*, **71**, 772 (1986).
- 144 S. S. Dukhin, A. E. Yaroshchuk, and B. V. Deryagin, *Colloid J. USSR*, **46**, 191 (1984).
- 145 A. Uygun, O. Turkoglu, S. Sen, E. Ersoy, A. G. Yavuz, and G. G. Batir, *Current Applied Physics*, **9**, 866 (2009).
- 146 D. Duracher, F. Sauzedde, A. Elaissari, C. Pichot, and L. Nabzar, *Colloid Polym. Sci.*, **276**, 920 (1998).
- 147 R. Pelton, D. Zhang, K. L. Thompson, and S. P. Armes, *Langmuir*, **27**, 2118 (2011).
- 148 M. J. Garcia-Salinas and F. J. de las Nieves, *Colloid Surf. A: Phys. Eng.*, **222**, 65 (2003).
- 149 G. Navaneetham and J. D. Posner, *J. Fluid Mech.*, **619**, 331 (2009).
- 150 P. C. Hiemenz, R. Rajagopalan, Principles of Colloid and Surface Chemistry, Marcel Dekker, New York, 1997, pp.145.
- 151 Y. Liu, S. Bo, Y. Zhu, and W. Zhang, *Polymer*, **44**, 7209 (2003).
- 152 K. Kandori, H. Ishiguro, K. Kon-no, and A. Kitahara, *Langmuir*, **5**, 1258 (1989).
- 153 H. Kishimoto, M. Watanabe, T. Iyoda, K. Nagai, and M. Nakagawa, *Chem. Lett.*, **35**, 598 (2006).
- 154 T.R. Aslamazova and K. Tauer, *Colloid Surf. A-Physicochem. Eng. Asp.*, **300**, 260 (2007).
- 155 M. P. Ryder, K. F. Schilke, J. A. Auxier, J. McGuire, and J. A. Neff, *J. Colloid Interface Sci.*, **350**, 194 (2010).
- 156 J. J. Si, H. Ono, K. Uchida, S. Nozaki, H. Morisaki, and N. Itoh, *Appl. Phys. Lett.*,

- 
- 79**, 3140 (2001).
- 157 W. L. Wu, W. E. Wallace, E. K. Lin, G. W. Lynn, C. J. Glinka, E. T. Ryan, and H. M. Ho, *J. Appl. Phys.*, **87**, 1193 (2000).
- 158 G. Porod, Small Angle X-ray Scattering, Academic Press INC., Eds: O.Glatte and O. Kratky, London, New York , (1980).
- 159 M. L. O'Neill, M. K. Haas, B. K. Peterson, R. N. Vrtis, S. J. Weigel, D. Wu, M. D. Bitner, and E. J. Karwacki, *Mater. Res. Soc. Symp. Proc.*, **914**, 0914-F01-02 (2006) .
- 160 A. Grill, D. A. and Neumayer, *J. Appl. Phys.*, **94**, 6697 (2003).
- 161 J. Tan, Z.W. Zhong, and H.M. Ho, *Micro. Eng.*, **81**, 75 (2005)..
- 162 A. P. Roberts, and E. J. Garboczi, *J. Am. Ceram. Soc.*, **83**, 3041 (2000).
- 163 H. Miyoshi, N. Hata, and T. Kikkawa, *Jpn. J. Appl. Phys.*, **44**, 1166 (2005).
- 164 F. Aldinger, V. A. Weberru, Advanced Ceramics and Future Materials, Chapter 3, WILEY-VCH GmbH & Co. KGaA, Weinheim (2010).

---

## Vita

### 【Personal information】

- Name: 譚昱涵 / Yu-Han Chen
- Gender: Male
- Date of birth: 1981/04/22
- Nationality: Taiwan (R.O.C)
- Email: [osiris0422@yahoo.com.tw](mailto:osiris0422@yahoo.com.tw)

### 【Education】

Degree	Name of School / Major	From	To	Research Advisor
Ph.D	National Chiao Tung University Materials Science and Engineering	Sep. 2005	Jun. 2012	Jihperng Leu
MS	National Taipei University of Technology Materials and Mineral Resources Engineering	Sep. 2003	Jun. 2005	Sea-Fue Wang
BS	Feng Chia University Materials Science and Engineering	Sep. 1999	Jun. 2003	

### 【Expertise】

- Low- $k$  and Porous Dielectric Materials.
- Nano Particle and Dispersion Technology.



---

✚ Thin Film Properties and Characterization.

✚ Surface/Physical/Electrical Analyses.

## 【Experience】

✚ Instrumental assistant:

- Particle size measurement in MSE dept. of NCTU (2008-2009).
- FIB/SEM dual guns system in Nano Facility Center of NCTU (2007-2008).
- FT-IR in MSE dept. of NCTU (2007-2008).
- BET in MSE dept. of NCTU (2006-2007).

## 【Publications List】

✚ Thesis of Master degree

奈米  $\alpha$ -Al<sub>2</sub>O<sub>3</sub> / Ni 核殼結構複合粉體之製備

Synthesis of Nano-Sized  $\alpha$ -Al<sub>2</sub>O<sub>3</sub>/Ni Core-Shell Composite Powders

✚ Dissertation of Ph.D. degree

超低介電孔洞材料 MSQ 薄膜中起孔劑聚集行為及孔洞形貌控制之研究

The porogen aggregation behavior, pore size, and size control of ultra-low-*k* porous organosilicate films based on MSQ/porogen hybrid system.

✚ International journal papers

- **Yu-Han Chen**, Hung-En Tu, and Jihperng Leu, “Effect of Surfactants on the Porogen Size in the Low-*k*

---

Methylsilsesquioxane/Polystyrene Hybrid Films”, Microporous and Mesoporous Materials, 162, 181-188 (2012).

- **Yu-Han Chen**, U-Ser Jeng, and Jihperng Leu, “Effect of Curing on the Porogen Size in the Low-*k* MSQ/SBS Hybrid Films”, *Journal of The Electrochemical Society*, **158** (3), G52 (2011).
- Hung-En Tu, **Yu-Han Chen**, and Jihperng Leu, “Low-*k* SiC<sub>x</sub>N<sub>y</sub> Films Prepared by Plasma-enhanced Chemical Vapor Deposition using 1,3,5-trimethyl-1,3,5-trivinylcyclotrisilazane Precursor”, *Journal of The Electrochemical Society*, **159** (5), G56 (2012).
- Mu-Lung Che, Cheng-Ying Huang, Shindy Chuang, **Yu-Hen Chen**, and Jihperng Leu, “Thermal and Mechanical Properties of Hybrid Methylsilsesquioxane/poly(styrene-*b*-4-vinylpyridine) Low-*k* Dielectrics Using a Late Porogen Removal Scheme,” *Journal of Materials Research*, **25**(6), 1049 (2010).

#### Conference papers

- **Yu-Han Chen** and Jihperng Leu, "The Effect of Heating Rate on the Porogen Behavior and Pore Sizes in the Methylsilsesquioxane/Porogen hybrid Low-*k* Films," Proceedings of Materials Research Society Symposium, Vol. 1147, OO04-08, 2009.
- **Yu-Han Chen** and Jihperng Len, “Electrostatic dispersion on polystyrene sizes in solution and pore sizes in the porous low-*k* MSQ thin films,” 2008 International Electron Devices and Materials Symposia: oral section AO-424, 28-29 November, 2008, Taichung, Taiwan.
- Mu-Lung Che, Jihperng Leu, **Yu-Hen Chen**, Cheng-Ying Huang, and Shindy Choang, “Effects of High-Temperature Porogens on Materials Properties of Novel 2-Phase Low-*k* Dielectrics,” 211th

---

Meeting of the Electrochemical Society, Trans., 6(3), 591, May 6-10, 2007, Chicago, Illinois, USA.

- Mu-Lung Che, Cheng-Ying Huang, Shindy Chuang, **Yu-Hen Chen**, Ying-Lang Wang, and Jihperng Leu, “A Study of High-temperature Porogens in the Formation of Novel Low-*k* Materials and Its Impact on Mechanical properties,” 2006 Materials Research Society Taiwan, P03-128, November 24-25, 2006, Tainan, Taiwan.

